Multiple Scattering Approach for Excitations
in Complex Systems

Dissertation

zur Erlangung des Doktorgrades der Naturwissenschaften
(Dr. rer. nat.)

der

Naturwissenschaftlichen Fakultät II
Chemie, Physik und Mathematik

der Martin-Luther-Universität
Halle-Wittenberg

vorgelegt von

Herrn Stefan Thomas
geb. am 12.02.1988 in Merseburg

Gutachter:

1. PD Dr. Arthur Ernst (Max-Planck-Institut für Mikrostrukturphysik)
2. Prof. Dr. Wolfgang Paul (Martin-Luther-Universität Halle-Wittenberg)
3. Prof. Dr. Hisazumi Akai (University of Tokyo)

Tag der öffentlichen Verteidigung: 21. April 2017

This is LuaTeX, Version 0.95.0 (TeX Live 2016/Arch Linux)

Abstract

This thesis deals with the application of the multiple scattering theory to describe physical properties of complex systems. In particular, it is concerned with the calculation of magnons and plasmons. The magnetic properties of disordered systems are treated in terms of the classical Heisenberg Hamiltonian allowing the calculation of their magnetic susceptibility. To get an understanding of the magnetic behavior of disordered systems, diluted magnets in form of a model system and the alloy $Fe_{1-x}Al_x$ are investigated. The calculations of the plasmonic properties of metallic nanostructures are performed with the Generalized Multiparticle Mie method, which is a multiple scattering extension to the classical Mie theory. The method is used to design a plasmonic filter.

Diese Dissertation beschäftigt sich mit der Anwendung der Vielfachstreutheorie zur Beschreibung physikalischer Eigenschaften komplexer Systeme. Im Speziellen handelt sie von der Berechnung von Magnonen und Plasmonen. Die magnetischen Eigenschaften ungeordneter Systeme werden im Rahmen des klassischen Heisenberg-Hamiltonians behandelt, was die Berechnung der magnetischen Suszeptibilität erlaubt. Um ein Verständnis für den Magnetismus in ungeordneten System zu entwickeln, werden verdünnte Magnete am Beispiel eines Modellsystems und der Legierung $Fe_{1-x}Al_x$ untersucht. Die Berechnung der plasmonischen Eigenschaften metallischer Nanostrukturen wird mit der verallgemeinerten Vielteilchen-Mie-Methode, die eine Vielfachstreuerweiterung der klassischen Mie-Theorie darstellt, durchgeführt. Diese Methode wird hier verwendet um einen plasmonischen Filter zu entwickeln.

Contents

Contents

1 Introduction

Many processes in physics can be explained with the concept of quasiparticles. This concept helps to describe the interactions between the elementary particles and certain physical phenomena, because these phenomena behave in a particle-like manner. The quasiparticles of interest here are the collective excitations, which describe the excitation state of a whole system in a particle picture. Typical examples for these collective excitations are vibrations of the lattice, propagating disturbances in the magnetic order or oscillations in the charges of a solid, which are represented as phonons, magnons and plasmons, respectively. The other kind of quasiparticles are particles in a narrower sense: for example, missing electrons or bound states of two particles, i.e., electron holes or excitons, respectively. In the framework of this thesis, two collective excitations were of particular interest: magnons and plasmons.

Magnons are propagating disturbances in the magnetic order of a magnetic system. They play an important role, e.g., in understanding the electron-electron interaction in superconductors or newly found phenomena like current-induced magnetization switching and domain wall motion.[1] A very strong interest can also be found in magnonics. This is among other things important for better storage devices,[2,3] and spintronic applications, which are aimed at improving or replacing conventional semiconductor technology.[4] Experimental measurements of magnons can be performed by spin-polarized electron energy loss spectroscopy,[1,5] inelastic neutron scattering,[6–9] Brillouin scattering,[10] ferromagnetic scattering[11,12] and spin-polarized scanning tunneling microscopy.[13]

Plasmons, on the other hand, are oscillations of free charges in a system. They play an important role in the design of plasmonic nanoantennas[14–17] and surface-enhanced Raman spectroscopy (SERS). A new field of research is spinplasmonics, which is a combination of spintronics and plasmonics, aimed at the design of magnetism-controlled plasmonic devices.[18–20] Typical experimental techniques to measure surface plasmons include the electron energy loss spectroscopy (EELS) in a transmission electron microscope (TEM) and the attenuated total reflection.[21]

A theoretical description of both quasiparticles can be achieved using a multiple scattering approach. This approach is similar for both quasiparticles – as well as for other (quasi-)particles – although the underlying theoretical frameworks

are different. Most of the time, the applicable scheme breaks down into the evaluation of a single-scattering problem, i.e., the scattering at a single scatterer like an atom, and the subsequent self-consistent solution of the scattering between multiple scatterers.

The particular interest of this thesis is the investigation of these quasiparticles in disordered systems – a difficult task within the well-known methods, but interesting for many applications. The magnon dispersion relation of a perfect system can be easily calculated in terms of the torque matrix derived from the Heisenberg Hamiltonian.[22] However, disordered systems require more sophisticated approaches like the coherent potential approximation (CPA) or the application of a Monte Carlo algorithm (MCA) in combination with the calculation of the susceptibility. The investigation of plasmons is focused on the optimization of plasmonic nanostructures with respect to near-field enhancement and filtering of certain wavelengths. While well-known algorithms like the discrete dipole approximation,[23] the generalized multipole technique,[24] the boundary element method[25] or finite element methods like the discontinuous Galerkin time domain method[26,27] are flexible but computationally expensive, the T-matrix method is very efficient but restricted in the systems possible to compute.[28] A method, which is both fast and flexible, is the Generalized Multiparticle Mie method,[29,30] which was implemented and used for optimization of plasmonic nanostructures.

In addition to the study of magnons and plasmons, the multiple scattering approach was also used to investigate electronic and magnetic properties of several other systems: The calculation of the electronic structure with electron multiple scattering theory was used to investigate the electromechanical properties of the semiconductors ZnO and $Pb_xSn_{1-x}Te$. Both systems have a band gap depending on the applied mechanical strain. On the other hand, the magnetic properties of several Heusler alloys were studied. The system $Ca(Co_xRu_{1-x})O_3$ exhibits anti-ferromagnetic interaction between nearest-neighbor Co atoms. The lack of magnetic ordering suggests the existence of a frustrated magnetic lattice in this material. Concluding to this investigation, the "traditional" Heusler alloys Pd_2MnSn, Ni_2MnSn and Cu_2MnAl are examined with respect to a uniform description of their magnetic and thermodynamic properties.

This thesis consists of four parts: At first, the experiments for the investigation of magnons and plasmons are described and subsequently the corresponding theory is explained. Then, a brief overview of some computational details is provided in order to give some insight, how the actual calculations were performed. Finally, the results of the investigations about magnons and plasmons, but also the results from the study of the electromechanical systems and the Heusler alloys, are presented.

2 Review of experimental techniques to investigate magnons and plasmons

In order to provide a proper theoretical description of magnons and plasmons, it is necessary to take a look at the available experiments and the observable physical quantities. Therefore, the following chapter provides a review of the most prominent experimental techniques to detect these two quasiparticles.

In both cases, most experiments rely on the scattering of an incident particle, e.g., electrons, neutrons or photons. This encourages the theoretical description of magnons and plasmons in terms of multiple scattering theory to be as close to the experiment as possible. The measured quantity is usually the energy and the corresponding wave vector of the scattered particle. This allows to determine the dispersion relation – the relation between energy and momentum, or frequency and wave vector – which is accessible from theoretical calculations.

2.1 Magnons at metallic surfaces and thin films

In a perfect ferromagnetic system, the spins of all atoms are parallel to each other. However, due to thermal excitations, these spins can deviate from their equilibrium orientation. Since the ferromagnetic system exhibits an effective magnetic field, the deviated spins start to precess. At this point, the interaction between all neighboring spins induces a change of spin direction for the interacting spins. This propagating spin deviation can be observed as a so called spin-wave or magnon (cf. fig. 2.1.1) characterized by its frequency and wave vector.

Although magnons are a bulk property, the experiments[1,31] motivating the theoretical investigations of this thesis were carried out at the surface of thin films. Also, most of the other available experiments presented in the following are restricted to properties at the surface like the resulting 2-dimensional dispersion relation. The according theoretical description described in section 3.1.4 is not restricted to 2-dimensional systems but describes these as a special case of a 3-dimensional system.
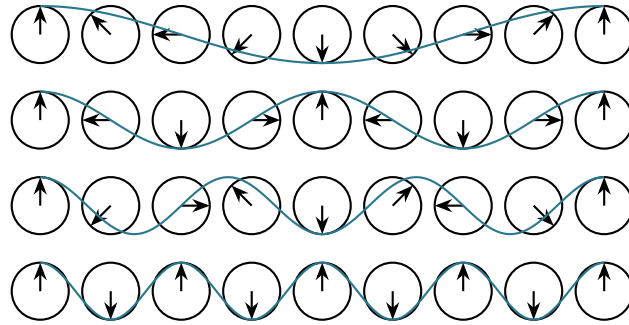
Figure 2.1.1: Schematic representation of magnons with different wavelengths. The arrows depict the deviation of the spins from the out-of-plane, ferromagnetical ordering.
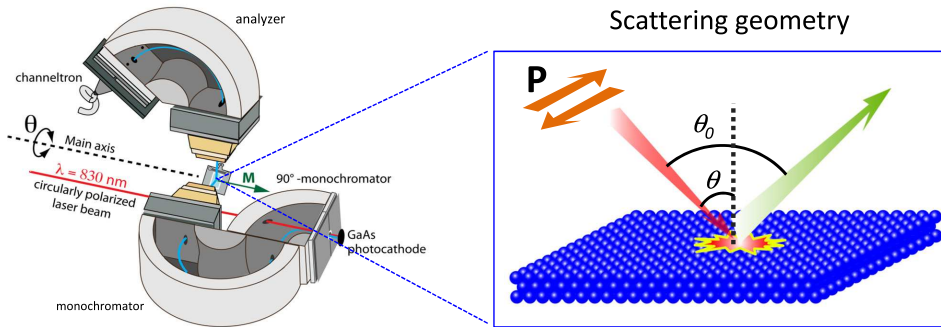
Figure 2.1.2: Experimental setup for SPEELS.[5]

2.1.1 Spin-polarized electron energy loss spectroscopy

A recently developed method is the spin-polarized electron energy loss spectroscopy (SPEELS).[1,5] The experimental setup, shown in fig. 2.1.2, consists of a source of spin-polarized electrons, a monochromator to define the energy of incident electrons, an analyzer to measure the energy loss and a channeltron to detect the scattered electrons.

The spin-polarized electrons, which are directed at the sample, are usually created with an GaAs-cathode irradiated by a beam of circularly polarized light. By application of strain, e.g., by creating the cathode as a semiconducting heterostructure with large lattice strain, the polarization of the emitted electrons can reach up to 90 %. The handedness of the circular polarization of the incident laser beam influences the spin direction of the created electrons, which is either
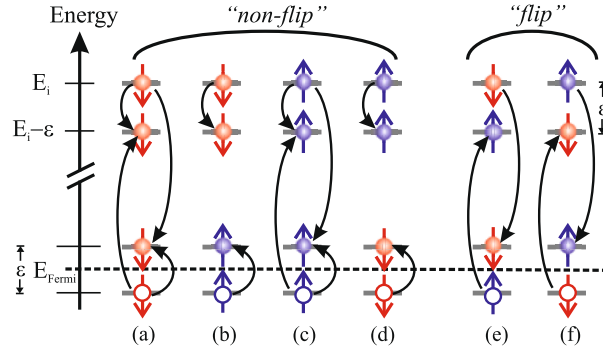
Figure 2.1.3: Possible excitations occurring in a SPEELS experiment. Only the "flip" excitations correspond to scattering at magnons.[1]

parallel or antiparallel to the majority electrons of the sample. However, the final detection of electrons is spin-unresolved.

The scattering process at the sample is influenced by several possible excitations presented in fig. 2.1.3. These excitations can be divided into "non-flip" and "flip" excitations. Only the latter can be magnon excitations, because both the creation and annihilation of magnons require a spin exchange of $1\hbar$. The following paragraph summarizes the six excitations observed for an incident electron with energy E_i.

An incident electron with spin-down polarization can experience an excitation of a spin-down electron below the Fermi energy E_{Fermi}, where either the excited or the incident electron gets scattered, while the other one will occupy a state above the Fermi energy (cf. fig. 2.1.3a). Another possibility is the excitation of a spin-up electron from below the Fermi energy to a state above the Fermi energy, while the incident electron gets scattered (cf. fig. 2.1.3b). Both of these excitations exhibit no spin exchange and are thus not involved with magnon creation or annihilation. However, the third possible excitation, where the incident spin-down electron excites and scatters a spin-up electron, while occupying a state above the Fermi energy, involves a spin flip (cf. fig. 2.1.3e), which is necessary to create a magnon. In the case of an incident spin-up electron, the "non-flip" excitations are similar (cf. fig. 2.1.3c,d), while the "flip" excitation (cf. fig. 2.1.3f) requires an angular momentum of $1\hbar$, i.e., the annihilation of a magnon.[1]

The SPEELS measurements are typically performed by measuring the scattering rate for a given energy loss and a wave vector parallel to the sample surface. The measured detector-dependent scattering rate is proportional to the
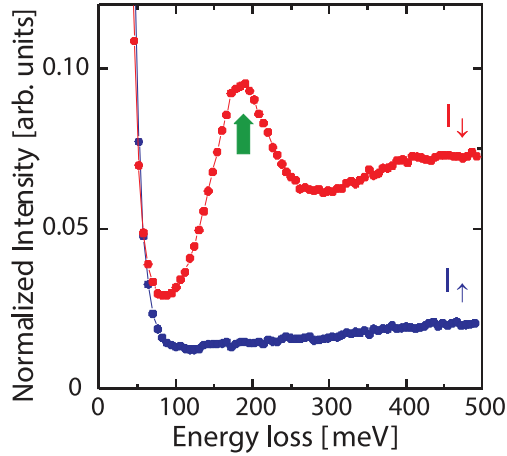
Figure 2.1.4: SPEELS spectrum for 8ML Co(100) on Cu(100).[1]

spin-polarized electron energy loss probability. The resulting spin-resolved spectra show characteristic peaks due to magnon excitations. These contributions are proportional to the imaginary part of the transverse magnetic susceptibility. Figure 2.1.4 shows a SPEELS spectrum of 8 monolayers (ML) of Co(100) on Cu(100). The spin-down channel contains a significant peak around 180 meV, which is the result of magnon creation.

As mentioned before, it is also possible to annihilate thermally excited magnons. Since the annihilation frees the magnon's energy, this process leads to an energy gain, which can be seen as peaks in the negative energy range of the SPEELS spectra (fig. 2.1.5a). Accordingly, it is also expected that a cooled sample does not show magnon annihilation, because no thermally exited magnons should exist (fig. 2.1.5b).

The possibility to measure energy loss and energy gain allows the distinction of magnon and phonon excitations, of which the latter will also appear in the spectra. On the one hand, magnon creation and annihilation require an exchange of angular momentum. Thus, the asymmetry of the intensities $((I_\downarrow - I_\uparrow)/(I_\downarrow + I_\uparrow))$ has positive and negative sign, respectively. Differing from this, the phonon excitations are spin-independent. The sign of the asymmetry is therefore equal for both energy gain and loss. In fig. 2.1.6, these phenomena are prominently visible. The peaks at around ± 19 meV show opposite sign and can thus be attributed to magnon creation and annihilation. The other peaks are caused by phonon excitations, because their intensities' asymmetry shows the same sign for positive and negative energy ranges.

Figure 2.1.5: SPEELS spectra for 2ML Fe(110)/W(110) at (a) 300 K and (b) 10 K. Magnon excitations can be observed at $\pm 45\,\text{meV}$.[1]

Figure 2.1.6: SPEELS spectra for Fe(001)-O(1×1) surface at 300 K. The gray area marks magnon excitations.[1]

2.1.2 Inelastic neutron scattering

A second possible experiment, which can be used to measure magnons, is the inelastic neutron scattering (INS). Due to the advantageous relation of energy and momentum of slow neutrons, this method is well suited for such measurements.

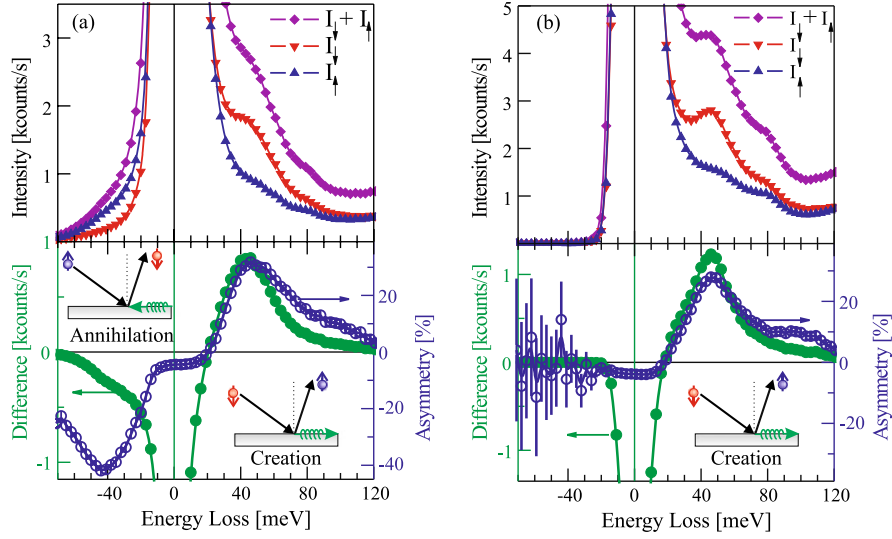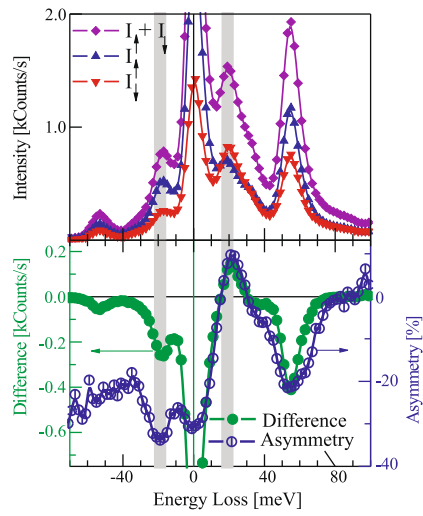In INS experiments, slow neutrons with predetermined energy $E_{inc} \approx 100\,\text{meV}$ and momentum $\boldsymbol{k}_{inc}$ are directed at the sample. In addition to the well-known Bragg peaks, which appear due to elastic scattering, there are additional peaks in their direct vicinity. These are the result of inelastic excitations. The corresponding energy can be determined from the energy E_{sca} and the wave vector $\boldsymbol{k}_{sca}$ of the scattered neutron,[6–8]

$$\boldsymbol{k}_{inc} - \boldsymbol{k}_{sca} = 2\pi\boldsymbol{G} - \boldsymbol{q}, \tag{2.1.1}$$

$$\Delta E = E_{inc} - E_{sca} = \pm\hbar\omega. \tag{2.1.2}$$

The reciprocal lattice vector $\boldsymbol{G}$ corresponds to a Bragg peak, from which the neutron was inelastically scattered. The energy $\pm\hbar\omega$ and the momentum $\boldsymbol{q}$ describe the created/annihilated excitation.

Here, it is again important to distinguish between magnon and phonon excitations. For this reason, the INS experiment can be performed with spin polarized neutrons created by reflection from, e.g., Fe_3O_4 or $Co_{92}Fe_8$. Because neutrons have a magnetic moment of $\frac{1}{2}\hbar$, they are well suited to create or annihilate magnons. The distinction between magnon and phonon excitations can finally be achieved by the modification of the polarisation state of the spin-polarized neutron beam, because the intensity of the peak depends on the polarization state.[9,32]

2.1.3 Brillouin scattering

Similar to inelastic neutron scattering, it is also possible to perform these experiments with photons, i.e., inelastic light scattering.

A typical setup consists of a monochromatic polarized light source, which is directed at the sample and scattered by 180°. The polarization of the incident photons is parallel to the plane of incidence, so called p-polarization, while the scattered photons can have s- and p-polarization, i.e., perpendicular or parallel to the plane of incidence. The energy of the scattered photon can be analyzed with a Fabry-Pérot interferometer.[10]

As already known, a change of polarization is necessary for the photon to interact with the magnon. Therefore, it is possible to distinguish between phonon and magnon excitations by analysis of the backscattered photons.[10] The energy

change of the photon and the difference of incident and scattered wave vectors determine the dispersion relation of the magnons.

2.1.4 Ferromagnetic resonance

A completely different approach is used in ferromagnetic resonance experiments. Here, the sample is put into a high-frequency magnetic field and the energy absorption is measured.

In contrast to the other methods, it is not possible to determine the in-plane dispersion relation $E(k_\parallel)$ of magnetic thin-films, but the discrete out-of-plane ($k_\perp$) magnons, which are caused by the confinement of the upper and lower interfaces/surfaces of the sample:[11]

$$k_\perp = \frac{p\pi}{L}, \qquad\qquad p \text{ is an odd integer.} \qquad (2.1.3)$$

The dispersion of the magnons is interpreted to have a quadratic dispersion relation. It depends on the magnetic exchange constant A and the saturation magnetization M:

$$\omega = \omega_0 + \frac{2A\gamma k_\perp^2}{M}. \qquad (2.1.4)$$

However, this method can still be used, to gain information about "standing" spin-waves, i.e., at the Γ point ($k_\parallel = 0$).[12]

2.1.5 Spin-polarized scanning tunneling microscope

The scanning tunneling microscope (STM) can also be used to create and annihilate magnons in a surface sample. To be able to measure this as inelastic scattering, it is necessary to create a magnetized STM tip to create a spin-polarized tunneling current. For this purpose, a tungsten tip can be coated with iron, resulting in a spin polarization of $60\,\%$ minority electrons. Depending on the magnetization of the sample – parallel or antiparallel to the tip – these electrons will enter the sample as minority or majority electrons.[13]

In the STM experiment, the same restrictions on the spin directions for the creation and annihilation of magnons apply as in the SPEELS experiments, i.e., only the minority electrons can create magnons, while majority electrons can only annihilate magnons. Assuming a cooled sample, where no thermally excited magnons exist, a difference in the intensity of the measured signal can be observed, when switching the magnetization of the sample. This can be used
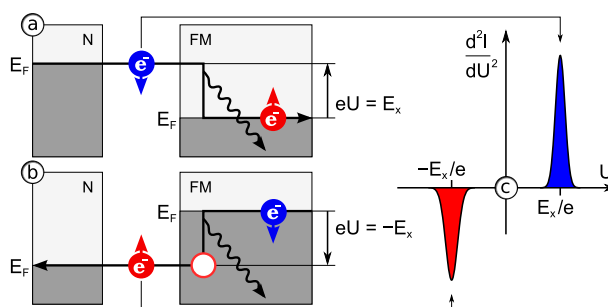
Figure 2.1.7: Magnon creation of two tunneling directions. (a) If the sample bias is positive, minority electrons can scatter into majority states, creating magnons. This yields a peak at $U = E_{\mathrm{x}}/e$. (b) For a negative bias, tunneling majority electrons leave majority holes behind, that can in turn be filled with minority electrons leading again to magnon creation and a resulting peak at $U = -E_{\mathrm{x}}/e$.[13]

to distinguish between magnons and phonons, because phonon excitations are – again – independent of the spin direction of the electrons.

The process of magnon creation is sketched in fig. 2.1.7. For both positive and negative sample bias, the creation of magnons is possible either by scattering minority electrons in majority states, or by tunneling majority electrons, which leave majority holes behind. However, a big caveat of this method is the inaccessibility of $\boldsymbol{q}_{\parallel}$-space information. The electrons are essentially moving out-of-plane and thus only a small part of the space around $\boldsymbol{q}_{\parallel} = 0$ contributes to the measured signal.

2.2 Plasmonic excitations at surfaces and in nanoparticles

The second kind of collective excitations, which are described in this thesis, are plasmons. Plasmons are rapid oscillations of the charge density and are usually observed confined to surfaces or interfaces as surface plasmon polaritons or localized surface plasmons. The former describe the coupling between the charge oscillations in a metal with the electromagnetic field in a dielectric, while the latter describe the confinement of these charge oscillations to nanoparticles in the sub-wavelength domain.[33] However, plasmons can also appear in bulk systems as volume plasmons, which were the subject of previous research.[34,35]

The charge oscillations are the result of the interaction of the electromagnetic field with the free conduction electrons in a metal. This process can be described by a plasma model of a gas of free electrons, which moves against a fixed background of positive ion cores:

$$m\ddot{\boldsymbol{x}} + m\eta\dot{\boldsymbol{x}} = -e\boldsymbol{E}. \tag{2.2.1}$$

This equation of motion describes an electron with the charge $-e$ and the effective mass m, whose motion is damped by collisions occurring at frequency $\eta = 1/\tau$. From this simple model, the most important quantity, the permittivity $\varepsilon(\omega)$, can be derived as:

$$\varepsilon(\omega) = 1 - \frac{\omega_{\mathrm{p}}^2}{\omega^2 + \mathrm{i}\eta\omega}, \tag{2.2.2}$$

with the plasma frequency of the electron gas $\omega_{\mathrm{p}} = \frac{n\,e^2}{\varepsilon_0 m}$ and the electron density n. This model is known as the Drude model of the permittivity.

The real and imaginary parts of the Drude permittivity, $\varepsilon = \varepsilon_1 + \mathrm{i}\varepsilon_2$,

$$\varepsilon_1(\omega) = 1 - \frac{\omega_{\mathrm{p}}^2\tau^2}{1 + \omega^2\tau^2}, \qquad\qquad \varepsilon_2(\omega) = \frac{\omega_{\mathrm{p}}^2\tau^2}{1 + \omega^2\tau^2}, \tag{2.2.3}$$

show immediately the importance of the plasma frequency ω_{p} for the permittivity of a material: If the frequency of the excitation is much larger than the plasma frequency, or if the plasma frequency is very small due to missing free electrons, the imaginary part of the permittivity vanishes and leaves a material behaving like a dielectric – no plasmons can be observed.

Figure 2.2.1 shows this behavior by comparing the permittivities of gold[36] and silicon:[37] In the range of visible light, the imaginary part of the permittivity of silicon vanishes leaving a dielectric material. On the other hand, gold has a significant contribution to the imaginary part of its permittivity resulting in observable plasmon excitations. However, the actual description of the permittivity of gold is more complicated than the Drude model and requires more sophisticated approaches to explain the interaction of the free electrons and the electromagnetic fields (cf. section 5.2.1).

For detection and measuring purposes, the strong coupling between the plasmons and the electromagnetic fields can be exploited by interacting with the latter and interpreting them as the electromagnetic part of a surface plasmon polariton. The interaction, here, is achieved with either charged particles, i.e., usually electrons, or with incident photons. Additionally, it is also possible to image surface plasmons with a number of different microscopy techniques. An overview over available methods is briefly discussed, below.[33]
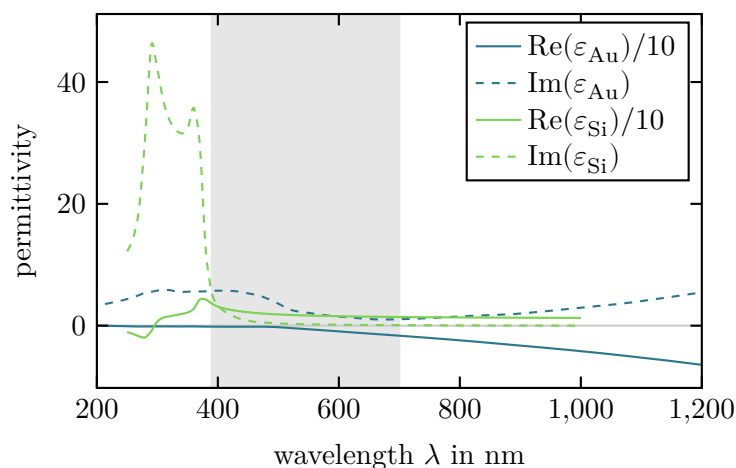
Figure 2.2.1: Permittivity of gold[36] and silicon.[37] The imaginary part of silicon's permittivity almost vanishes in the visible part of the spectrum (marked gray).

2.2.1 Low-energy electron diffraction

A way of excitation and measurement of plasmons is given by the low-energy electron diffraction. In this experiment, the incident electron can experience an energy loss due to plasmon excitations in the bulk and at the surface. While the bulk plasmons are causing an energy loss of $\hbar\omega_{\mathrm{p}}$, the surface plasmon excitation results in a lower-lying peak at $\hbar\omega_{\mathrm{p}}/\sqrt{1+\varepsilon}$, which reduces in the case of air/vacuum to $\hbar\omega_{\mathrm{p}}/\sqrt{2}$.

2.2.2 Transmission electron microscopy

The extension of the low-energy electron diffraction to the transmission of high-energy electrons yields the electron energy loss spectroscopy. This is an experiment, which can be performed with transmission electron microscopes (TEM).

The main principle of this experiment is the measurement of the energy loss, which a passing electron experiences, due to the interaction of the electron and the electromagnetic field of the surface plasmon induced by the electron itself. By adding another source of energy to the system, e.g., a light pump, it would also be possible, to measure an energy gain.[38]

2.2.3 Attenuated total reflection

A different approach is the excitation of surface plasmons by attenuated total reflection. An incoming laser beam is coupled with the help of an optical prism with high refractive index, which is located at the surface.[21] The prism is necessary, because the propagation constant of the surface plasmon β and the in-plane propagation constant of the incident light beam $k_{\parallel} = k_0 \sin\theta$ have to match. The definition of the propagation constant β,

$$\beta = k_0 \sqrt{\frac{\varepsilon_{\mathrm{m}}\varepsilon_{\mathrm{i}}}{\varepsilon_{\mathrm{m}} + \varepsilon_{\mathrm{i}}}}, \tag{2.2.4}$$

for a metal-insulator interface with respective permittivities ε_{m} and ε_{i}, however, prohibits this matching because $\beta > k_0 \geq k_{\parallel}$.

The matching between the propagation constants can by achieved with two different configurations: The Kretschmann geometry consists of a metal layer with a dielectric on one side and the prism on the other. Due to the difference between the permittivity of the prism and the dielectric, the matching condition can be fulfilled by exciting a surface plasmon through the metal layer. The second configuration is the Otto geometry, where the prism is located above the dielectric-metal interface to yield a prism-dielectric-metal system.

In both cases, the evanescent waves from the total reflection at the prism-metal or prism-dielectric interfaces are coupling to the surface plasmons. The surface plasmon excitations appear as dips in the reflectivity spectra, in dependence of the incidence angle.

2.2.4 Grating coupling

Similar to the light coupling with high-refractive index prisms, the matching condition $\beta = k_{\parallel}$ can also be achieved by modification of the metal-dielectric interface. A surface grating, either by direct modification of the metal or by application of a dielectric, can modify the matching condition. A grating with lattice constant a results in the matching condition

$$\beta = k_{\parallel} \pm \frac{2\pi n}{a}, \tag{2.2.5}$$

with integer $n = 1, 2, ...$ In this experiment, the plasmon excitations will appear in the reflectivity spectra, too.

2.2.5 Microscopy techniques

A broad field of excitation and measurement of plasmons is available with different kinds of microscopes. For example, a microscope with a high numerical aperture allows to locally excite surface plasmons, because of the large spread of the incident beam allowing larger incidence angles than in the attenuated total reflection method. The excited surface plasmons radiate back into the microscope, where this leakage radiation can be analyzed. This method is well suited for analysis of the propagation width of a continuum of surface plasmons.

Similarly, near-field microscopy allows the localized excitation of surface plasmons, because of the sub-wavelength tip size and the resulting low numerical aperture. The leakage of plasmons out of the tip area allows the analysis of the effects of surface roughness.

Both methods can be also be used to analyze the surface plasmons excited by attenuated total reflection and grating coupling.

3 Fundamental theory in magnonics and plasmonics

The purpose of this chapter is the description of the underlying theory necessary to describe magnons and plasmons. It is a brief summary of the well-known fundamental principles, which were used for research and development presented in chapters 4 and 5.

On the one hand, for the calculation of magnonic excitations, it is necessary to describe the electronic properties of the systems of interest. The according calculations are performed in terms of the density functional theory. The given results can then be used to obtain the magnetic exchange parameters, which are required to calculate the magnetic properties in terms of the disordered Heisenberg Hamiltonian.

On the other hand, the investigation of plasmonic excitations requires the solution of the electromagnetic wave equation with special attention to the frequency-dependent complex permittivity. This equation is solved in terms of the classical Mie theory, which is extended to multiple scatterers. The necessary expansions of excitations in terms of the Spherical Vector Wave Functions are provided afterwards.

3.1 Magnon theory

The description of magnon excitations in the framework of this thesis will be done in terms of the well-known classical Heisenberg model (see section 3.1.4). This theoretical model is based on the exchange coefficients J_{ij}, which describe the energy needed to change the spin at site i under the influence of the spin at site j. They can be calculated in terms of the density functional theory[39] by investigation of the total energy, while the spins are infinitesimally deviated in opposite directions (keeping the total magnetisation constant). However, the treatment of the density functional theory with the Green's function method by Korringa, Kohn and Rostoker (KKR)[40,41] allows the application of the magnetic force theorem,[42] which provides a more precise and efficient approach for calculating

the exchange coefficients. These topics will be only discussed shortly, because they were not the main subject of this thesis.

3.1.1 Electron multiple scattering theory

The calculation of physical properties, like the aforementioned exchange coefficients, was performed in terms of the KKR method[40,41] as it is implemented in the computer program Hutsepot.[43,44] This method solves the Kohn-Sham equation[45] by application of a Green's function approach. As the KKR method is not the main part of this thesis, only a summary of the method is provided. A more thorough description, including a description of the relativistic variant of this algorithm, can be found, e.g., in the book of Zabloudil et al.[46]

The main idea of the KKR method is the solution of the Schrödinger equation

$$\mathcal{H}\psi = E\psi, \tag{3.1.1}$$

with the Hamiltonian $\mathcal{H}$ in terms of its resolvent

$$\mathcal{G}(z) = (z\mathcal{I} - \mathcal{H})^{-1}, \qquad z = \epsilon + \mathrm{i}\delta, \qquad \mathcal{G}(z^*) = \mathcal{G}(z)^\dagger. \tag{3.1.2}$$

The operator $\mathcal{I}$ is the identity operator, and z is the complex energy with its real and imaginary parts ϵ and δ.

The method's eponymous Green's function is defined as any representation of the resolvent $\mathcal{G}(z)$, e.g.,

$$\langle \boldsymbol{r} \,|\, \mathcal{G}(z) \,|\, \boldsymbol{r}' \rangle = G(\boldsymbol{r}, \boldsymbol{r}'; z). \tag{3.1.3}$$

The solution of the Schrödinger equation is, however, a non-trivial task. A possible ansatz is the definition of the system in terms of a free system with the potentials added as a perturbation:

$$\mathcal{H} = \mathcal{H}_0 + \mathcal{V}. \tag{3.1.4}$$

There are now two resolvents $\mathcal{G}$ and $\mathcal{G}_0$,

$$\mathcal{G}(z) = (z\mathcal{I} - \mathcal{H})^{-1}, \qquad \mathcal{G}_0(z) = (z\mathcal{I} - \mathcal{H}_0)^{-1}, \tag{3.1.5}$$

which are connected in terms of a Dyson equation

$$\mathcal{G}(z) = \mathcal{G}_0(z) + \mathcal{G}(z)\mathcal{V}\mathcal{G}_0(z) = \mathcal{G}_0(z) + \mathcal{G}_0(z)\mathcal{V}\mathcal{G}(z). \tag{3.1.6}$$

The iterative insertion of the formula allows to define the $\mathcal{T}$ operator

$$\mathcal{T}(z) = \mathcal{V} + \mathcal{V}\mathcal{G}_0(z)\mathcal{V} + \mathcal{V}\mathcal{G}_0(z)\mathcal{V}\mathcal{G}_0(z)\mathcal{V} + \dots, \tag{3.1.7}$$

which yields

$$\mathcal{G}(z) = \mathcal{G}_0(z) + \mathcal{G}_0(z)\mathcal{T}\mathcal{G}_0(z), \tag{3.1.8}$$

or

$$\mathcal{T}(z)\mathcal{G}_0(z) = \mathcal{V}\mathcal{G}(z). \tag{3.1.9}$$

In actual calculations, the corresponding Hamiltonian H is not given by the full Schrödinger Hamiltonian $\mathcal{H}$ including the full interaction between all involved electrons. The Hohenberg-Kohn-theorem[39] states that the ground state of a system of N electrons is already determined by their charge density $n(\boldsymbol{r})$. This charge density can be determined by solving the Kohn-Sham equations for N non-interacting electrons. However, this approach requires the treatment of the exchange and correlation between the N electrons in terms of this single-electron charge density. The easiest and well-known approaches to treat this problem are the local density approximation (LDA) and the generalized gradient approximation (GGA).

The Hamiltonian $H(\boldsymbol{r})$ is given by a kinetic energy K and an effective single particle potential $V(\boldsymbol{r})$, which contains the external potential from the lattice, the Coulomb interaction between the electrons and the exchange-correlation potential:

$$H(\boldsymbol{r}) = K + V(\boldsymbol{r}), \qquad V(\boldsymbol{r}) = \langle \boldsymbol{r} | \mathcal{V} | \boldsymbol{r} \rangle. \tag{3.1.10}$$

The effective potential $V(\boldsymbol{r})$ of a system is given by the individual effective potentials $V_i(\boldsymbol{r})$ of the individual scatterers at positions $\boldsymbol{R}_i$:

$$V(\boldsymbol{r}) = \sum_i^N V_i(\boldsymbol{r}_i), \qquad \boldsymbol{r}_i = \boldsymbol{r} - \boldsymbol{R}_i. \tag{3.1.11}$$

The individual potentials $V_i(\boldsymbol{r})$ are defined to be disjunct, i.e., not overlapping each other. A typical definition is given within the muffin-tin-approximation, where the total effective potential is given by non-overlapping spherical potentials with constant potential in the interstitial area. Another definition is the full-potential method, where the individual potentials are defined within the Voronoi

cell around each individual scatterer, which is comparable to their Wigner-Seitz-cell.

To account for multiple scattering, the $\mathcal{T}$ operator is expanded for the multiple scatterers, and thus for the potentials, in the system. By naming the single-site $\mathcal{T}$ operator of the potential $\mathcal{V}_n$ as t^n,

$$t^n = \mathcal{V}_n + \mathcal{V}_n \mathcal{G}_0 t^n = (\mathcal{I} - \mathcal{V}\mathcal{G}_0)^{-1}\mathcal{V}_n, \tag{3.1.12}$$

the multi-site $\mathcal{T}$ operator can be rewritten as

$$\mathcal{T} = \sum_n \mathcal{V}_n + \sum_{n,m} \mathcal{V}_n \mathcal{G}_0 \mathcal{V}_m + \sum_{n,m,k} \mathcal{V}_n \mathcal{G}_0 \mathcal{V}_m \mathcal{G}_0 \mathcal{V}_k + ... \tag{3.1.13}$$

$$= \sum_n t^n + \sum_{n,m} t^n \mathcal{G}_0(1 - \delta_{nm})t^m + \sum_{n,m,k} t^n \mathcal{G}_0(1 - \delta_{nm})t^m \mathcal{G}_0(1 - \delta_{mk})t^k$$

$$+ \sum_{n,m,k,j} t^n \mathcal{G}_0(1 - \delta_{nm})t^m \mathcal{G}_0(1 - \delta_{mk})t^k \mathcal{G}_0(1 - \delta_{kj})t^j. \tag{3.1.14}$$

Alternatively, the multi-site $\mathcal{T}$ operator can be defined in terms of the scattering path operators τ^{nm}

$$\mathcal{T} = \sum_{nm} \tau^{nm}, \tag{3.1.15}$$

$$\tau^{nm} = t^n \delta_{nm} + t^n \mathcal{G}_0(1 - \delta_{nm})t^m + \sum_k t^n \mathcal{G}_0(1 - \delta_{nk})t^k \mathcal{G}_0(1 - \delta_{km})t^m$$

$$+ \sum_{k,j} t^n \mathcal{G}_0(1 - \delta_{nk})t^k \mathcal{G}_0(1 - \delta_{kj})t^j \mathcal{G}_0(1 - \delta_{jm})t^m + ... \tag{3.1.16}$$

Combining the scattering path operators τ^{mn}, the single-site $\mathcal{T}$ operator t^n, and the structure constants $\mathcal{G}_0$ for the whole system in corresponding supermatrices $\underline{\tau}$, $\underline{t}$ and $\underline{\mathcal{G}}_0$, the main equation of the Green's function method can be written as

$$\underline{\tau} = \left(\underline{t}^{-1} - \underline{\mathcal{G}}_0\right)^{-1}. \tag{3.1.17}$$

An important similarity to the later presented T-matrix method in plasmonics can be observed, when the incoming and outgoing waves from a single particle, ψ_i^n and ψ_o^n, are related with the single-site scattering operator t^n:[47]

$$|\psi_o^n\rangle = \mathcal{G}_0 t^n |\psi_i^n\rangle. \tag{3.1.18}$$

The outgoing wave can be easily calculated from the incoming wave by application of the structure constant $\mathcal{G}_0$ and the single-site scattering operator t^n. After numerical expansion, this process yields a simple matrix multiplication.

3.1.2 Coherent potential approximation

The above description of the KKR method is limited to ordered structures. Therein, disorder can only be described by creating a large supercell, which is used as an approximation to the actual disorder. Unfortunately, this approach has two major problems: Increasing the size of the calculated cell means also a massive increase in computation time, and supercell calculations are still subject to periodic repetition of the used structure. The latter problem is especially important in smaller supercells, because this "ordered disorder" can lead to artifacts, which will not appear in the actual system.

In order to circumvent these problems, early approaches were done in terms of the Virtual Crystal Approximation (VCA). The VCA is implemented by averaging the potentials of the alloyed atoms V_i with their respective concentrations c_i:

$$V_{\mathrm{VCA}} = \sum_i c_i V_i. \tag{3.1.19}$$

This method yields satisfying results for small perturbations, e.g., from atoms with similar potentials, but breaks for systems with larger atomic potentials like they appear in systems with localized electronic states.

The next development was achieved by averaging the single-site scattering matrices t, resulting in the Average t-matrix Approximation (ATA). Similar to the VCA, the scattering matrices of the alloyed atoms t_i are weighted with their concentrations:

$$t_{\mathrm{ATA}} = \sum_i c_i t_i. \tag{3.1.20}$$

This method assumes small concentrations for the atoms to be able to neglect the inter-site scattering contributions but degrades for higher concentrations. It is essentially a non-self-consistent version of the Coherent Potential Approximation (CPA).

The CPA tries to tackle these problems by introducing a coherent t-matrix $\underline{t}_{\mathrm{C}}$.[43,48] The idea is to avoid the additional scattering contributions from the interaction of the alloyed atoms. An expression for the coherent t-matrix can be derived by starting with the weighted average of the scattering path operator,

$$\tau_{\mathrm{C}}^{nm} = \sum_i c_i \tau_i^{nm}. \tag{3.1.21}$$

This condition is, in practice, only required for $n = m = 0$. In comparison to eq. (3.1.17), the relation between the diagonal coherent scattering path operator τ_C^{00} and the coherent t-matrix $\underline{t}_C$ is given by

$$\tau_C^{00} = \frac{1}{\Omega_{BZ}} \int d\boldsymbol{k} \left(t_C^{-1} - \mathcal{G}_0(\boldsymbol{k}) \right)^{-1}, \qquad (3.1.22)$$

with the volume of the Brillouin zone Ω_{BZ}. The diagonal impurity scattering path operators can be obtained from a Dyson equation,

$$\tau_i^{00} = \frac{\tau_C^{00}}{1 + \tau_C^{00}(t_i^{-1} - t_C^{-1})}. \qquad (3.1.23)$$

By iteration of the following equation, a self-consistent solution to the above eqs. (3.1.22) and (3.1.23) can be obtained:[43]

$$t_C^{\text{new}} = \left(\frac{\tau_C^{00}\left(\sum_i c_i \tau_i \right)^{-1} - 1}{\left(\sum_i c_i \tau_i \right)^{-1}} + t_C^{-1} \right)^{-1} \qquad (3.1.24)$$

The CPA can successfully calculate the electronic properties of many random alloys. However, the single-site approximation cannot describe the influence of effects such as short-range order. The necessary extension of the sketched algorithm is given by the Multi-Sublattice Non-Local CPA (MS-NL-CPA), which is also implemented in the used computer program Hutsepot.[43,49]

3.1.3 Magnetic force theorem

The magnonic subsystem, i.e., the interaction of the spins, will be described in terms of the classical Heisenberg Hamiltonian. This effective Hamiltonian relates the existing spins with the magnetic exchange coefficients J_{ij} between the spins at sites i and j:

$$H = -\sum_{ij} J_{ij} \boldsymbol{S}_i \cdot \boldsymbol{S}_j. \qquad (3.1.25)$$

Following from this definition, positive exchange coefficients yield a ferromagnet and negative ones an anti-ferromagnet.

A straightforward way to calculate the interaction of a single spin with the rest of the ferromagnetic system is the deviation of this spin by a small angle θ.

According to the definition of the Heisenberg-Hamiltonian, this will result in an energy change of

$$\delta E_0 = 2 \sum_j J_{0j}(1 - \cos\theta) \approx J_0\theta^2, \tag{3.1.26}$$

$$J_0 = \sum_j J_{0j}. \tag{3.1.27}$$

The interaction between two spins at sites i and j can similarly be determined by deviating them to opposite angles $\pm\theta/2$, resulting in an energy change of

$$\delta E_{ij} = J_{ij}(1 - \cos\theta) \approx \tfrac{1}{2}J_{ij}\theta^2. \tag{3.1.28}$$

However, the calculation of this energy change is quite difficult in terms of the usual DFT calculations. The KKR method with its previously defined single-site $\mathcal{T}$ operators t^i and scattering path operators τ^{ij} can overcome this problem by employing Lloyd's formula to yield a compact definition of the exchange coefficients[42]

$$J_{ij} = -\frac{1}{4\pi} \operatorname{Im} \int_{-\infty}^{E_f} dE \operatorname{Tr}\left\{ \left[(t^i_\uparrow)^{-1} - (t^i_\downarrow)^{-1} \right] \tau^{ij}_\uparrow \left[(t^j_\uparrow)^{-1} - (t^j_\downarrow)^{-1} \right] \tau^{ij}_\downarrow \right\}. \tag{3.1.29}$$

The integral is performed by integrating over the occupied energy range, i.e., all energies below the Fermi energy E_f.[50,51]

3.1.4 Disordered Heisenberg-Hamiltonian

The taken approach to calculate the susceptibility of a magnetic system within the Heisenberg model is the equation of motion of a spin $\boldsymbol{S}_i$ in the (infinite) real space cluster. This spin is precessing due to the effective field $\boldsymbol{B}^i_{\text{eff}}$ resulting from the surrounding spins:

$$\partial_t \boldsymbol{S}_i = -\gamma \boldsymbol{S}_i \times \boldsymbol{B}^i_{\text{eff}}, \qquad \boldsymbol{B}^i_{\text{eff}} = \frac{1}{\mu_B S_i} \sum_j J_{ij} \boldsymbol{e}_j. \tag{3.1.30}$$

Assuming small deviations $e^+_i \equiv e^x_i + i e^y_i$ from a collinear ground state $\boldsymbol{e}_i \parallel \boldsymbol{e}_z$, this equation can be linearized:

$$\partial_t S_i \begin{pmatrix} e^x_i \\ e^y_i \\ e^z_i \end{pmatrix} = -\frac{\gamma}{\mu_B} \sum_j J_{ij} \begin{pmatrix} e^y_i e^z_j - e^z_i e^y_j \\ e^z_i e^x_j - e^x_i e^z_j \\ e^x_i e^y_j - e^y_i e^x_j \end{pmatrix}. \tag{3.1.31}$$

Therein, the spin $\boldsymbol{S}_i$ of an atom is defined by its magnitude S_i and the direction of its polarization $e_i^z = \pm 1$:

$$\boldsymbol{S}_i = S_i \begin{pmatrix} e_i^{\mathrm{x}} \\ e_i^{\mathrm{y}} \\ e_i^{\mathrm{z}} \end{pmatrix}. \tag{3.1.32}$$

In the next step, the first two components of the linearized equation of motion get combined. For easier notation, the magnitude e_i of the spin direction vector $\boldsymbol{e}_i$ shall be interpreted as the direction of the polarization $e_i \stackrel{!}{=} e_i^z$. Thus, $e_i = 1$ means that the moment of atom i points upwards and $e_i = -1$ represents a downward pointing moment:

$$\partial_t e_i^+ = -\frac{g}{S_i} \sum_j J_{ij}(e_i^{\mathrm{y}} e_j - e_i e_j^{\mathrm{y}} + \mathrm{i} e_i e_j^{\mathrm{x}} - \mathrm{i} e_i^{\mathrm{x}} e_j) \tag{3.1.33}$$

$$= \frac{\mathrm{i}g}{S_i} \sum_j J_{ij}(e_i^+ e_j - e_i e_j^+). \tag{3.1.34}$$

At this point, the deviations e_i^+ are time-dependent quantities. By introducing time-harmonic solutions

$$e_i^+(t) = e_i^+ \mathrm{e}^{\mathrm{i}\omega t}, \tag{3.1.35}$$

the eigenvalue problem for the realspace torque matrix can be derived:

$$\mathrm{i}\omega e_i^+ \mathrm{e}^{\mathrm{i}\omega t} = \frac{\mathrm{i}g}{S_i} \sum_j J_{ij}(e_i^+ \mathrm{e}^{\mathrm{i}\omega t} e_j - e_i e_j^+ \mathrm{e}^{\mathrm{i}\omega t}), \tag{3.1.36}$$

$$\omega e_i^+ = \frac{g}{S_i} \sum_j \Big(\delta_{ij} \sum_k J_{ik} e_j^+ e_k - J_{ij} e_i e_j^+ \Big). \tag{3.1.37}$$

Interpreting $\boldsymbol{e}_\lambda^+$ as the vector of the spin deviations for all atoms in the system with corresponding frequency ω_λ, the static torque matrix $\underline{\boldsymbol{T}} = \{T_{ij}\}$ can be derived:

$$\omega_\lambda e_{\lambda i}^+ = \sum_j T_{ij} e_{\lambda j}^+, \qquad T_{ij} = \frac{g}{S_i} \Big(\delta_{ij} \sum_k J_{ik} e_k - J_{ij} e_i \Big). \tag{3.1.38}$$

Since the investigated system is usually a translationally invariant (periodic) system, with cells $\boldsymbol{R}$ and position $\boldsymbol{r}_p$, the eigensolutions are plane waves

$$e_{\lambda i}^+ = e_{\lambda p}^+(\boldsymbol{q}) \mathrm{e}^{\mathrm{i}\boldsymbol{q}\cdot\boldsymbol{R}}, \tag{3.1.39}$$

or the Fourier transform can be performed. This, in turn, results in a split of the index i, which corresponds to the atoms in the infinite crystal, into an index p addressing the position in the (super-)cell, and the position $\boldsymbol{R}$ of the cell in the infinite crystal:

$$\omega_\lambda e_{\lambda p}^+ \mathrm{e}^{\mathrm{i}\boldsymbol{q}\cdot\boldsymbol{R}} = \sum_r \sum_{\boldsymbol{R}'} T_{(p,\boldsymbol{R}),(r,\boldsymbol{R}')} e_{\lambda r}^+ \mathrm{e}^{\mathrm{i}\boldsymbol{q}\cdot\boldsymbol{R}'}, \tag{3.1.40}$$

$$\omega_\lambda e_{\lambda p}^+ = \sum_r \sum_{\boldsymbol{R}'} T_{(p,\boldsymbol{R}),(r,\boldsymbol{R}')} e_{\lambda r}^+ \mathrm{e}^{\mathrm{i}\boldsymbol{q}\cdot(\boldsymbol{R}'-\boldsymbol{R})}. \tag{3.1.41}$$

In order to reduce eq. (3.1.41) back to a standard eigenvalue problem, it is necessary to include the summation over $\boldsymbol{R}'$ into the torque matrix $\underline{\boldsymbol{T}}$,

$$T_{pr} = \sum_{\boldsymbol{R}'} T_{(p,\boldsymbol{R}),(r,\boldsymbol{R}')} \mathrm{e}^{\mathrm{i}\boldsymbol{q}\cdot(\boldsymbol{R}'-\boldsymbol{R})} \tag{3.1.42}$$

$$= \frac{g}{S_p} \sum_{\boldsymbol{R}'} \Big(\delta_{pr} \delta_{\boldsymbol{R}\boldsymbol{R}'} \sum_l \sum_{\boldsymbol{R}''} J_{(p,\boldsymbol{R})}^{(l,\boldsymbol{R}'')} e_l \mathrm{e}^{\mathrm{i}\boldsymbol{q}\cdot(\boldsymbol{R}'-\boldsymbol{R})} - J_{(p,\boldsymbol{R})}^{(r,\boldsymbol{R}')} e_p \mathrm{e}^{\mathrm{i}\boldsymbol{q}\cdot(\boldsymbol{R}'-\boldsymbol{R})} \Big). \tag{3.1.43}$$

Distributing the sum with respect to $\boldsymbol{R}'$ allows to remove the first exponential due to the δ-function:

$$T_{pr} = \frac{g}{S_p} \Big(\delta_{pr} \sum_l e_l \sum_{\boldsymbol{R}''} J_{(p,\boldsymbol{R})}^{(l,\boldsymbol{R}'')} - e_p \sum_{\boldsymbol{R}'} J_{(p,\boldsymbol{R})}^{(r,\boldsymbol{R}')} \mathrm{e}^{\mathrm{i}\boldsymbol{q}\cdot(\boldsymbol{R}'-\boldsymbol{R})} \Big). \tag{3.1.44}$$

The translational invariance of the investigated system allows the summations to be shifted by $\boldsymbol{R}''$ and $\boldsymbol{R}'$, respectively:

$$T_{pr}(\boldsymbol{q}) = \frac{g}{S_p} \Big(\delta_{pr} \sum_l e_l J_{pl}(\boldsymbol{0}) - e_p J_{pr}(\boldsymbol{q}) \Big), \qquad J_{pr}(\boldsymbol{q}) = \sum_{\boldsymbol{R}} J_{(p,\boldsymbol{R})}^{(r,\boldsymbol{0})} \mathrm{e}^{-\mathrm{i}\boldsymbol{q}\cdot\boldsymbol{R}}, \tag{3.1.45}$$

$$\omega_\lambda e_{\lambda p}^+ = \sum_r T_{pr} e_{\lambda r}^+. \tag{3.1.46}$$

This dynamic torque matrix $\underline{\boldsymbol{T}}(\boldsymbol{q})$ is valid for a periodic system consisting of a unit cell with p atoms.

The summation over the interactions with neighboring atoms, which is theoretically an infinite sum, is naturally limited by the limited physical range of the J_{ij}. Depending on the magnetic atoms in a system, only the first two or three shells might be required. For example, Heusler alloys often show a short-range interaction, while 3d-metals like Fe, Co or Ni exhibit a long-range exchange. The actual limit, which has to be set manually to match the physical properties of the involved atoms, results in a certain sparsity of the torque matrix $\underline{\boldsymbol{T}}(\boldsymbol{q})$. The degree of sparsity depends on the ratio of atoms within the selected interaction range compared to the total number of atoms in the system.

Transverse magnetic susceptibility

The transverse magnetic susceptibility in terms of the Heisenberg model can be derived from the application of a small transverse field $B_p^+(\boldsymbol{q})\mathrm{e}^{\mathrm{i}\boldsymbol{q}\cdot\boldsymbol{R}}\mathrm{e}^{\mathrm{i}\omega t}$ and the corresponding change in spins $S_p e_p^+ \mathrm{e}^{\mathrm{i}\boldsymbol{q}\cdot\boldsymbol{R}}\mathrm{e}^{\mathrm{i}\omega t}$:[22]

$$\sum_r S_r^{-1}(\omega\delta_{pr} - T_{pr}(\boldsymbol{q}))S_r e_r^+(\boldsymbol{q}) = \gamma e_p \frac{1}{\mu_{\mathrm{B}}}(-\mu_{\mathrm{B}}B_p^+(\boldsymbol{q})). \tag{3.1.47}$$

Starting from the latter equation, the inverse of the transverse magnetic susceptibility can be defined by

$$\left(\chi^{-1}(\omega, \boldsymbol{q})\right)_{pr} = \mu_{\mathrm{B}}e_p\gamma^{-1}S_r^{-1}(\omega\delta_{pr} - T_{pr}(\boldsymbol{q})). \tag{3.1.48}$$

Inserting the definition of the torque matrix $\underline{\boldsymbol{T}}$ from eq. (3.1.45) and replacing the circular frequency ω with the complex energy z, which is possible due to the application of atomic units ($\hbar = 1$), yields a directly calculable expression for the inverse susceptibility matrix

$$\left(\chi^{-1}(z, \boldsymbol{q})\right)_{pr} = \frac{e_p z}{g S_r}\delta_{pr} - \frac{e_p}{g S_r}T_{pr}(\boldsymbol{q}) \tag{3.1.49}$$

$$= \frac{e_p z}{g S_r}\delta_{pr} - \frac{e_p}{g S_r}\Big(\delta_{pr}\sum_l J_{pl}(\boldsymbol{0}) - e_p J_{pr}(\boldsymbol{q})\Big). \tag{3.1.50}$$

Since this calculation will be performed in a supercell, it is important to care for the Bloch factors, introduced by the interactions $J_{pr}(\boldsymbol{q})$, when the summation wraps around the boundary of the supercell.

In principle, the formula above would be enough to calculate the loss from the susceptibility matrix $\underline{\boldsymbol{\chi}}$,

$$\mathcal{L} = \frac{1}{2\mathrm{i}}(\underline{\boldsymbol{\chi}} - \underline{\boldsymbol{\chi}}^\dagger), \tag{3.1.51}$$

associated with the susceptibility of a single disordered system. However, the main target is the calculation of the average susceptibility and the corresponding loss in a disordered supercell. This can be achieved by averaging the susceptibility matrices $\underline{\boldsymbol{\chi}}$ over a larger amount of differently occupied supercells (so called configurations). Afterwards, it is possible to fold the supercell back to the original supercell by application of a Fourier transformation

$$\chi(\boldsymbol{q}) = \sum_p \sum_r \mathrm{e}^{\mathrm{i}\boldsymbol{q}\cdot\boldsymbol{r}_p}\mathrm{e}^{-\mathrm{i}\boldsymbol{q}\cdot\boldsymbol{r}_r}\chi_{pr}(\boldsymbol{q}). \tag{3.1.52}$$
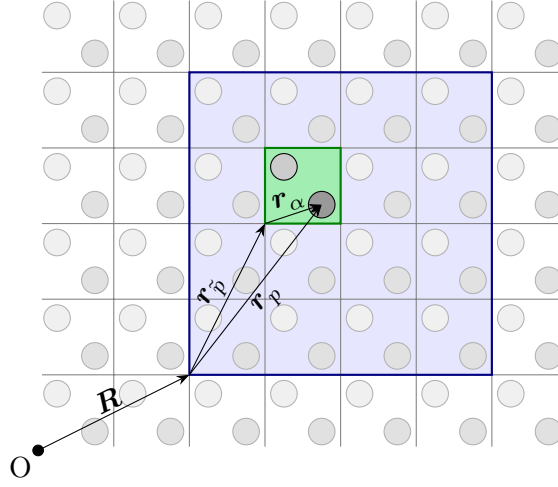
Figure 3.1.1: Definition of coordinates. The simulation domain is a supercell (blue) consisting of unit cells (green) with several basis atoms (circles).

A general extension to this algorithm is the introduction of an additional subdivision of the supercell $\boldsymbol{R}$ into basis sites α in a cell $\tilde{p}$ (see fig. 3.1.1) by splitting the vectors as

$$\boldsymbol{r}_i = \boldsymbol{R} + \boldsymbol{r}_p \tag{3.1.53}$$

$$= \boldsymbol{R} + \boldsymbol{r}_{\tilde{p}} + \boldsymbol{r}_\alpha. \tag{3.1.54}$$

This leads to the definition of the basis-resolved susceptibility

$$\chi_{\alpha\beta}(\boldsymbol{q}) = \sum_{\boldsymbol{r}_{\tilde{p}}} \sum_{\boldsymbol{r}_{\tilde{r}}} \mathrm{e}^{\mathrm{i}\boldsymbol{q}\cdot\boldsymbol{r}_{\tilde{p}}} \mathrm{e}^{-\mathrm{i}\boldsymbol{q}\cdot\boldsymbol{r}_{\tilde{r}}} \big(\chi(\boldsymbol{q})\big)_{(\tilde{p},\alpha),(\tilde{r},\beta)}. \tag{3.1.55}$$

The calculation of a complete susceptibility spectrum, with respect to energy z and wave vector $\boldsymbol{q}$, requires, in principle, the recalculation of the susceptibility matrix $\underline{\chi}$ for every wave vector $\boldsymbol{q}$ and a subsequent Fourier transform. However, the actual dependency of the susceptibility matrix $\underline{\chi}$ on the wave vector is given by $J_{pr}(\boldsymbol{q})$ (cf. eq. (3.1.45)) as

$$\mathrm{e}^{\mathrm{i}\boldsymbol{q}\cdot\boldsymbol{R}}, \quad \text{for any wave vector } \boldsymbol{R}. \tag{3.1.56}$$

Exploiting this fact by restricting the spectra to wave vectors where this factor vanishes allows to calculate the spectrum without having to recalculate the

susceptibility matrix. In particular, only the Fourier transform is required. This procedure is possible, because the introduction of plane waves in eq. (3.1.39) was performed in terms of the supercell (cf. fig. 3.1.1), while the final Fourier transform in eq. (3.1.52) was done with respect to the position of the atoms in the supercell.

The advantage of the aforementioned method is its ability to correctly represent the magnetic susceptibility as it results from disordered structures. Possible finite size effects will appear for small systems, but they vanish rapidly by increasing the size of the system (cf. section 5.1.1). A Monte Carlo approach can be used to keep the systems at intermediate sizes, while the finite-size effects are almost perfectly avoided. One caveat of the method is, however, that it requires the adiabatic approximation, which neglects any broadening due to interactions with electrons, photons, or with the Stoner continuum. This problem can be avoided by using the dynamic approximation within Monte Carlo calculations, but this was beyond the scope of the investigations in this thesis.

Alternatively, the calculation of disordered magnonic systems can be achieved with the CPA. This method was implemented by Paweł Buczek and the details can be found in the appendix of [T1].

The general idea is the similarity of several quantities between electronics and magnonics (cf. sections 3.1.1 and 3.1.2): The structure constant $\mathcal{G}_0$, defined in eq. (3.1.5), has the same structure as the free spin propagator, except that the Hamiltonian of the "free magnonic system" is $\mathcal{H}_0 = 0$:

$$G_0 = z^{-1}\mathcal{I}. \tag{3.1.57}$$

The potential $\mathcal{V}$ corresponds to the product of the electron's g-factor γ, the spin moment matrix S,

$$S_{pr} = S_p \delta_{pr}, \tag{3.1.58}$$

and the torque matrix T. Appropriately, the magnon spin propagator can be calculated from the equation

$$G = G_0 + G_0 \gamma STG, \tag{3.1.59}$$

which compares perfectly to eq. (3.1.6). The susceptibility χ is then defined as

$$\chi = \gamma GS. \tag{3.1.60}$$

3.2 Electromagnetic scattering theory

3.2.1 Wave equation

The starting point for electromagnetic scattering theory are Maxwell's equations:

$$\boldsymbol{\nabla} \cdot \boldsymbol{B} = 0, \qquad\qquad \boldsymbol{\nabla} \times \boldsymbol{E} = -\frac{\partial \boldsymbol{B}}{\partial t}, \qquad\qquad (3.2.1)$$

$$\boldsymbol{\nabla} \cdot \boldsymbol{D} = \rho, \qquad\qquad \boldsymbol{\nabla} \times \boldsymbol{H} = \boldsymbol{j} + \frac{\partial \boldsymbol{D}}{\partial t}. \qquad\qquad (3.2.2)$$

For both the electric and magnetic fields, a respective tensorial susceptibility describes the reaction of the medium resulting in electric polarization $\boldsymbol{P}$ and magnetization $\boldsymbol{M}$,

$$\frac{P_i}{\varepsilon_0} = \sum_j \chi_{\mathrm{e},ij}^{(1)} E_j + \sum_{jk} \chi_{\mathrm{e},ijk}^{(2)} E_j E_k + \sum_{jkl} \chi_{\mathrm{e},ijkl}^{(3)} E_j E_k E_l + \ldots, \qquad (3.2.3)$$

$$M_i = \sum_j \chi_{\mathrm{m},ij}^{(1)} H_j + \sum_{jk} \chi_{\mathrm{m},ijk}^{(2)} H_j H_k + \sum_{jkl} \chi_{\mathrm{m},ijkl}^{(3)} H_j H_k H_l + \ldots. \qquad (3.2.4)$$

The above equations can be linearized for small intensities by omitting terms of higher order. Furthermore, most materials can by described by an isotropic model, leaving a scalar susceptibility. By application of the material equations

$$\boldsymbol{D} = \varepsilon_0 \boldsymbol{E} + \boldsymbol{P} = \varepsilon_0 (1 + \chi_{\mathrm{e}}) \boldsymbol{E} = \varepsilon_0 \varepsilon_{\mathrm{r}} \boldsymbol{E}, \qquad\qquad (3.2.5)$$

$$\boldsymbol{B} = \mu_0 (\boldsymbol{H} + \boldsymbol{M}) = \mu_0 (1 + \chi_{\mathrm{m}}) \boldsymbol{H} = \mu_0 \mu_{\mathrm{r}} \boldsymbol{H}, \qquad\qquad (3.2.6)$$

the electric flux density $\boldsymbol{D}$ and the magnetic flux density $\boldsymbol{B}$ can be eliminated.

In general, both the relative permittivity ε_{r} and the relative permeability μ_{r} are frequency-dependent quantities. Especially, the complex-valued permittivity (cf. section 2.2) is necessary for the theoretical description of plasmons. The restriction to non-magnetic materials (i.e., $\mu_{\mathrm{r}} \approx 1$), which forbids calculation for spin-plasmonic applications, allows to reduce Maxwell's equations to

$$\boldsymbol{\nabla} \cdot \boldsymbol{H} = 0, \qquad\qquad \boldsymbol{\nabla} \times \boldsymbol{E} = -\mu_0 \frac{\partial \boldsymbol{H}}{\partial t}, \qquad\qquad (3.2.7)$$

$$\boldsymbol{\nabla} \cdot \varepsilon_{\mathrm{r}} \boldsymbol{E} = \frac{\rho}{\varepsilon_0}, \qquad\qquad \boldsymbol{\nabla} \times \boldsymbol{H} = \boldsymbol{j} + \varepsilon_0 \varepsilon_{\mathrm{r}} \frac{\partial \boldsymbol{E}}{\partial t}. \qquad (3.2.8)$$

Similar to the introduction of time-dependent solutions for the definition of the magnonic torque matrix (cf. eq. (3.1.35)), the electric and magnetic fields should have a harmonic time dependency, too. Due to different conventions in the

different fields of physics, the signs differ ($\mathrm{e}^{-\mathrm{i}\omega t}$ instead of $\mathrm{e}^{\mathrm{i}\omega t}$). The harmonic time dependency allows further reductions in the induction and circuital law

$$\boldsymbol{\nabla} \cdot \boldsymbol{H} = 0, \qquad\qquad \boldsymbol{\nabla} \times \boldsymbol{E} = \mathrm{i}\omega\mu_0 \frac{\partial \boldsymbol{H}}{\partial t}, \qquad\qquad (3.2.9)$$

$$\boldsymbol{\nabla} \cdot \varepsilon_\mathrm{r} \boldsymbol{E} = \frac{\rho}{\varepsilon_0}, \qquad\qquad \boldsymbol{\nabla} \times \boldsymbol{H} = \boldsymbol{j} - \mathrm{i}\omega\varepsilon_0\varepsilon_\mathrm{r} \frac{\partial \boldsymbol{E}}{\partial t}. \qquad\qquad (3.2.10)$$

In homogeneous media without free charges ρ and currents $\boldsymbol{j}$, the homogeneous wave equations can be derived from the above induction and circuital law

$$\boldsymbol{\nabla} \times \boldsymbol{\nabla} \times \boldsymbol{E} = -\mu_0\mu_\mathrm{r}\varepsilon_0\varepsilon_\mathrm{r} \frac{\partial^2 \boldsymbol{E}}{\partial t^2}, \qquad\qquad (3.2.11)$$

$$\boldsymbol{\nabla} \times \boldsymbol{\nabla} \times \boldsymbol{H} = -\mu_0\mu_\mathrm{r}\varepsilon_0\varepsilon_\mathrm{r} \frac{\partial^2 \boldsymbol{H}}{\partial t^2}. \qquad\qquad (3.2.12)$$

The definition of the vacuum speed of light $c_0 = \frac{1}{\sqrt{\mu_0\varepsilon_0}}$ and the refraction index $n = \sqrt{\mu_\mathrm{r}\varepsilon_\mathrm{r}}$ yields the well known wave equations

$$\Delta\boldsymbol{E} - \frac{n^2}{c_0} \frac{\partial^2 \boldsymbol{E}}{\partial t^2} = 0, \qquad\qquad (3.2.13)$$

$$\Delta\boldsymbol{H} - \frac{n^2}{c_0} \frac{\partial^2 \boldsymbol{H}}{\partial t^2} = 0. \qquad\qquad (3.2.14)$$

Due to the relation between the electric and magnetic field, where the latter can be calculated from the former with the induction law, further discussion can be restricted to the electric field.

3.2.2 Single-sphere scattering

In a scattering experiment with a single sphere, three fundamental fields appear: the incident field $\boldsymbol{E}_\mathrm{inc}$, the internal field $\boldsymbol{E}_\mathrm{int}$ and the scattered field $\boldsymbol{E}_\mathrm{scat}$. They are related by the boundary condition at the surface of the sphere (with normal vector $\boldsymbol{n}$)

$$(\boldsymbol{E}_\mathrm{inc} + \boldsymbol{E}_\mathrm{sca} - \boldsymbol{E}_\mathrm{int}) \times \boldsymbol{n} = 0. \qquad\qquad (3.2.15)$$

The expansion of these fields is done in terms of the spherical vector wave functions (SVWF) $\boldsymbol{M}_{mn}^{(1,3)}$ and $\boldsymbol{N}_{mn}^{(1,3)}$ (cf. eqs. (A.5) and (A.6))

$$\boldsymbol{E}_{\text{inc}} = \sum_{n=1}^{\infty} \sum_{m=-n}^{n} a_{mn}\boldsymbol{M}_{mn}^{(1)} + b_{mn}\boldsymbol{N}_{mn}^{(1)}, \qquad (3.2.16)$$

$$\boldsymbol{E}_{\text{int}} = \sum_{n=1}^{\infty} \sum_{m=-n}^{n} c_{mn}\boldsymbol{M}_{mn}^{(1)} + d_{mn}\boldsymbol{N}_{mn}^{(1)}, \qquad (3.2.17)$$

$$\boldsymbol{E}_{\text{sca}} = \sum_{n=1}^{\infty} \sum_{m=-n}^{n} f_{mn}\boldsymbol{M}_{mn}^{(3)} + g_{mn}\boldsymbol{N}_{mn}^{(3)}. \qquad (3.2.18)$$

The boundary condition helps to relate the expansion coefficients of the incident field a and b to the expansion coefficients of the scattered field f and g. In the case of a sphere, the relation is given by the well-known Mie coefficients

$$T_n^1 = -\frac{(m_{\text{r}}L_n(m_{\text{r}}x) + n/x)j_n(x) - j_{n-1}(x)}{(m_{\text{r}}L_n(m_{\text{r}}x) + n/x)h_n^{(1)}(x) - h_{n-1}^{(1)}(x)}, \qquad (3.2.19)$$

$$T_n^2 = -\frac{(L_n(m_{\text{r}}x)/m_{\text{r}} + n/x)j_n(x) - j_{n-1}(x)}{(L_n(m_{\text{r}}x)/m_{\text{r}} + n/x)h_n^{(1)}(x) - h_{n-1}^{(1)}(x)}, \qquad (3.2.20)$$

which depend on the relative refractive index $m_{\text{r}} = \sqrt{\varepsilon_{\text{i}}/\varepsilon_{\text{s}}}$ with the relative permittivities ε_{i} and ε_{s}, inside the sphere and in its surrounding, respectively. The dimensionless size parameter $x = kR$ is the product of the wave number and the radius of the sphere. The functions $j_n(x)$ and $h_n^{(1)}$ are spherical Bessel and Hankel functions, respectively. The logarithmic derivative L_n is defined as

$$L_n(\tilde{x}) = \frac{\text{d}}{\text{d}\tilde{x}}\left[\ln(\tilde{x}j_n(\tilde{x}))\right]. \qquad (3.2.21)$$

The relation between the expansion coefficients is now simply

$$f_{mn} = T_n^1 a_{mn}, \qquad\qquad g_{mn} = T_n^2 b_{mn}, \qquad (3.2.22)$$

which can be rewritten in matrix form

$$\begin{pmatrix} \boldsymbol{f} \\ \boldsymbol{g} \end{pmatrix} = \underline{\boldsymbol{T}}\begin{pmatrix} \boldsymbol{a} \\ \boldsymbol{b} \end{pmatrix} = \begin{pmatrix} \underline{\boldsymbol{T}}^1 & 0 \\ 0 & \underline{\boldsymbol{T}}^2 \end{pmatrix}\begin{pmatrix} \boldsymbol{a} \\ \boldsymbol{b} \end{pmatrix}, \qquad (3.2.23)$$

where $\underline{\boldsymbol{T}}$ defines the scattering matrix (T-matrix) for a single spherical particle.

At this point, the similarity of the different approaches of electronics and plasmonics become obvious. Equation (3.2.23) shows the relation between the expansion coefficients of the incident and scattered fields as a matrix product, similar to the scattering expression in eq. (3.1.18).

3.2.3 Multi-sphere scattering

The generalization of the T-matrix method of a single scatterer towards multiple scatterers can be achieved in several ways.

The first method is a direct approach, where the T-matrix of each scatterer is calculated and then related by application of translation coefficients for the SVWFs. For a dimer of spheres, this means, that at first the T-matrices $\underline{\boldsymbol{T}}_1$ and $\underline{\boldsymbol{T}}_2$ are calculated. In order to create the system's T-matrix $\underline{\boldsymbol{T}}_0$, several translation matrices $\underline{\mathfrak{T}}_{ij}^{(1,3)}$ have to be used, to translate the incident and scattered fields, denoted by the respective superscript (1) and (3), between the coordinate systems of the scatterers, themselves, and the system of scatterers as a whole:[28]

$$
\begin{aligned}
\underline{\boldsymbol{T}}_0 = {}& \underline{\mathfrak{T}}_{01}^{(1)}\underline{\boldsymbol{T}}_1(\underline{\boldsymbol{I}} - \underline{\mathfrak{T}}_{12}^{(3)}\underline{\boldsymbol{T}}_2\underline{\mathfrak{T}}_{21}^{(3)}\underline{\boldsymbol{T}}_1)^{-1}(\underline{\boldsymbol{I}} + \underline{\mathfrak{T}}_{12}^{(3)}\underline{\boldsymbol{T}}_2\underline{\mathfrak{T}}_{21}^{(1)})\underline{\mathfrak{T}}_{10}^{(1)} \\
& + \underline{\mathfrak{T}}_{02}^{(1)}\underline{\boldsymbol{T}}_2(\underline{\boldsymbol{I}} - \underline{\mathfrak{T}}_{21}^{(3)}\underline{\boldsymbol{T}}_1\underline{\mathfrak{T}}_{12}^{(3)}\underline{\boldsymbol{T}}_2)^{-1}(\underline{\boldsymbol{I}} + \underline{\mathfrak{T}}_{21}^{(3)}\underline{\boldsymbol{T}}_1\underline{\mathfrak{T}}_{12}^{(1)})\underline{\mathfrak{T}}_{20}^{(1)}.
\end{aligned}
\tag{3.2.24}
$$

Theoretically, this scheme could by expanded to systems with more scatterers, but the explicit inversions pose a difficult numerical problem. Even for a system of dimers, the maximum expansion order n is severely limited by the stability of the matrix inversion.

The second method is the Generalized Multiparticle Mie method.[29,30] In this approach, the scattering coefficients of all scatterers are related in a large system of equations. It is again necessary to translate the SVWFs expansion coefficients between the respective scatterers i and j with translation coefficients $A_{mn}^{\mu\nu}(j,i)$ and $B_{mn}^{\mu\nu}(j,i)$. These coefficients translate the scattered waves from particle j with indices μ, ν into incident waves on particle i with indices m, n:

$$
f_{mn}^i = T_{i,n}^1\left(a_{mn}^i - \sum_{\substack{j=1 \\ i \neq j}}^{N}\sum_{\nu=1}^{\infty}\sum_{\mu=-\nu}^{\nu}\left(f_{\mu\nu}^j A_{mn}^{\mu\nu}(j,i) + g_{\mu\nu}^j B_{mn}^{\mu\nu}(j,i)\right)\right), \quad (3.2.25)
$$

$$
g_{mn}^i = T_{i,n}^2\left(b_{mn}^i - \sum_{\substack{j=1 \\ i \neq j}}^{N}\sum_{\nu=1}^{\infty}\sum_{\mu=-\nu}^{\nu}\left(f_{\mu\nu}^j B_{mn}^{\mu\nu}(j,i) + g_{\mu\nu}^j A_{mn}^{\mu\nu}(j,i)\right)\right). \quad (3.2.26)
$$

This system of equations can be easily recast in matrix form making standard solvers for linear systems of equations applicable:

$$
\begin{aligned}
\left[\begin{pmatrix} \underline{\boldsymbol{I}} & 0 \\ 0 & \underline{\boldsymbol{I}} \end{pmatrix} + \begin{pmatrix} \underline{\boldsymbol{T}}^1 & 0 \\ 0 & \underline{\boldsymbol{T}}^2 \end{pmatrix}\begin{pmatrix} \underline{\boldsymbol{A}} & \underline{\boldsymbol{B}} \\ \underline{\boldsymbol{B}} & \underline{\boldsymbol{A}} \end{pmatrix}\right]\begin{pmatrix} \boldsymbol{f} \\ \boldsymbol{g} \end{pmatrix} &= \begin{pmatrix} \underline{\boldsymbol{T}}^1 & 0 \\ 0 & \underline{\boldsymbol{T}}^2 \end{pmatrix}\begin{pmatrix} \boldsymbol{a} \\ \boldsymbol{b} \end{pmatrix} \\
&= \begin{pmatrix} \tilde{\boldsymbol{a}} \\ \tilde{\boldsymbol{b}} \end{pmatrix}.
\end{aligned}
\tag{3.2.27}
$$

The matrices $\underline{A}$ and $\underline{B}$, containing the translation coefficients $A_{mn}^{\mu\nu}(j,i)$ and $B_{mn}^{\mu\nu}(j,i)$, can be determined using Mackowski's three-step-method:[52]

$$\underline{A}_{ij}(\boldsymbol{r}_{ij}) = \underline{R}^{-1}(\boldsymbol{r}_{ij})\underline{\tilde{A}}_{ij}(r_{ij})\underline{R}(\boldsymbol{r}_{ij}), \qquad (3.2.28)$$

$$\underline{B}_{ij}(\boldsymbol{r}_{ij}) = \underline{R}^{-1}(\boldsymbol{r}_{ij})\underline{\tilde{B}}_{ij}(r_{ij})\underline{R}(\boldsymbol{r}_{ij}). \qquad (3.2.29)$$

The matrices $\underline{\tilde{A}}_{ij}(r_{ij})$ and $\underline{\tilde{B}}_{ij}(r_{ij})$ describe the axial translations between the different coordinate systems, and the unitary matrix $\underline{R}$ describes the rotation of the coordinate system.

In contrast to the T-matrix method, which yields a single set of expansion coefficients for the whole system, the Generalized Multiparticle Mie method calculates a separate set of coefficients for each scatterer.

3.2.4 Excitation with light and electrons

A critical part of the scattering experiment is the kind of excitation. For many experiments, this is simply an incoming laser beam, which can be represented as plane wave or a focused gaussian beam.[28] On the other hand, in an STM, the scattering system is excited by the field induced from a passing electron.[53]

To be able to calculate the scattering, it is necessary to expand these incident fields into SVWFs. Since the SVWFs form a complete set of orthogonal basis functions on the unit sphere, the expansion coefficients can be calculated by integration of the incident field $\boldsymbol{E}_{\mathrm{inc}}$ over an auxiliary sphere:

$$a_{mn} = \frac{\int_0^\pi \mathrm{d}\theta \int_0^{2\pi} \mathrm{d}\varphi \, \boldsymbol{E}_{\mathrm{inc}} \boldsymbol{M}_{mn}^{(1)} \sin\theta}{\int_0^\pi \mathrm{d}\theta \int_0^{2\pi} \mathrm{d}\varphi \, |\boldsymbol{M}_{mn}^{(1)}|^2 \sin\theta}, \qquad (3.2.30)$$

$$b_{mn} = \frac{\int_0^\pi \mathrm{d}\theta \int_0^{2\pi} \mathrm{d}\varphi \, \boldsymbol{E}_{\mathrm{inc}} \boldsymbol{N}_{mn}^{(1)} \sin\theta}{\int_0^\pi \mathrm{d}\theta \int_0^{2\pi} \mathrm{d}\varphi \, |\boldsymbol{N}_{mn}^{(1)}|^2 \sin\theta}. \qquad (3.2.31)$$

For example, for an incident plane wave, the following non-vanishing expansion coefficients can be determined:

$$a_{1,n} = -a_{-1,n} = \mathrm{i}^{n-1}\sqrt{2n+1}, \qquad (3.2.32)$$

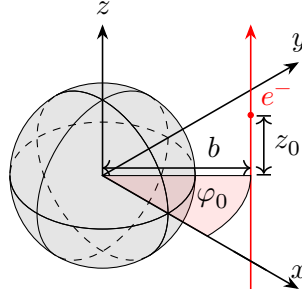$$b_{1,n} = b_{-1,n} = \mathrm{i}^{n-1}\sqrt{2n+1}. \qquad (3.2.33)$$

Figure 3.2.1: Coordinates of the electron beam passing a sphere.[T2]

However, the field resulting from a passing electron requires a more sophisticated derivation. The chosen approach is the description of the electric field $\boldsymbol{E}$ in terms of the scalar potential ϕ and vector potential $\boldsymbol{A}$

$$\boldsymbol{E} = -\boldsymbol{\nabla}\phi - \frac{\partial \boldsymbol{A}}{\partial t}. \tag{3.2.34}$$

The potentials are defined by the charge density ρ and current density $\boldsymbol{j}$,

$$\rho(\boldsymbol{r}, t) = -\delta(\boldsymbol{r} - \boldsymbol{r}_{\mathrm{e}}(t)), \tag{3.2.35}$$

$$\boldsymbol{j}(\boldsymbol{r}, t) = -\boldsymbol{v}\delta(\boldsymbol{r} - \boldsymbol{r}_{\mathrm{e}}(t)). \tag{3.2.36}$$

The time-dependent position of the passing electron $\boldsymbol{r}_{\mathrm{e}}(t)$ shall be limited to a trajectory in z-direction. This does not limit the possibilities, since the simulated system could be translated/rotated to fit this requirement:

$$\boldsymbol{r}_{\mathrm{e}}(t) = \boldsymbol{r}_0 + \boldsymbol{v}t, \qquad\qquad \boldsymbol{v} \parallel \boldsymbol{e}_{\mathrm{z}}. \tag{3.2.37}$$

Furthermore, the initial position $\boldsymbol{r}_0$ is given in cylindrical coordinates with radius b, azimuthal angle φ_0, and initial height z_0 (see fig. 3.2.1).

Inserting the time-dependent retarded Green's function into the definition of the electric field (3.2.34) yields a definition in terms of the retarded Green's function in the frequency domain:[54]

$$\boldsymbol{E}(t) = (\boldsymbol{\nabla} - \mathrm{i}k\boldsymbol{v}) \int_{-\infty}^{\infty} \mathrm{d}t'\, \mathrm{e}^{\mathrm{i}\omega t'} g_{\omega}^{+}(\boldsymbol{r}, \boldsymbol{r}_{\mathrm{e}}(t)). \tag{3.2.38}$$

Performing a multipole expansion for the Green's function g_ω^+ finally yields the expansion coefficients a_{mn} and b_{mn},[T2]

$$a_{mn} = R_m \frac{i^{n-2m} k}{\pi} \left(\frac{2}{n(n+1)} \right)^{\frac{1}{2}} m P_n^{|m|}(v^{-1}), \qquad (3.2.39)$$

$$b_{mn} = R_m \frac{i^{n-2m} k}{\pi} \left(\frac{2}{n(n+1)} \right)^{\frac{1}{2}} \frac{i}{2v\gamma}$$
$$\times \left(c_{m-1}^+ \sqrt{(n-m+1)(n+m)} P_n^{|m-1|}(v^{-1}) \right.$$
$$\left. - c_{m+1}^- \sqrt{(n+m+1)(n-m)} P_n^{|m+1|}(v^{-1}) \right), \qquad (3.2.40)$$

$$R_m = K_m \left(\frac{\omega b}{v} \frac{1}{\gamma} \right) \exp\left(-im\varphi_0 - i\frac{\omega b}{v} \frac{z_0}{b} \right). \qquad (3.2.41)$$

The functions $P_n^{|m|}$ are associated Legendre polynomials, and K_m are modified Bessel functions of the second kind. The Lorentz factor is given by $\gamma^{-1} = \sqrt{1 - v^2}$. The factors $c_m^{+/-}$ appear due to definition of the associated Legendre polynomials with $|m|$ as given by Doicu et al.[28] and correct the sign with respect to m:

$$c_m^+ = \begin{cases} 1 & m < 0 \\ -1 & m \geq 0 \end{cases}, \qquad c_m^- = \begin{cases} 1 & m \leq 0 \\ -1 & m > 0 \end{cases}. \qquad (3.2.42)$$

4 Combination and improvement of numerical techniques

The calculation of magnonic properties and the optimization of plasmonic nanostructures require the application of special numerical techniques to get satisfying result within a reasonable time. This chapter summarizes the investigations concerning the generation of random structures for magnonic systems, the analytic continuation of the magnetic susceptibility, and the optimization of plasmonic nanostructures. They are necessary for the calculations in the next chapter.

4.1 Generation of random structures

The generation of random structures, i.e., different occupations of the simulated supercells, is a critical part in the calculation of the susceptibility of disordered systems and plays an important role in the success of the method. The main goal of the following algorithms is to resemble real physical structures as closely as possible.

Especially for surface structures, it is important to find reasonable methods, because the growth process will impact the resulting structures: Figure 4.1.1a shows 7 monolayers of Co deposited on Cu(001), which yields a rugged surface
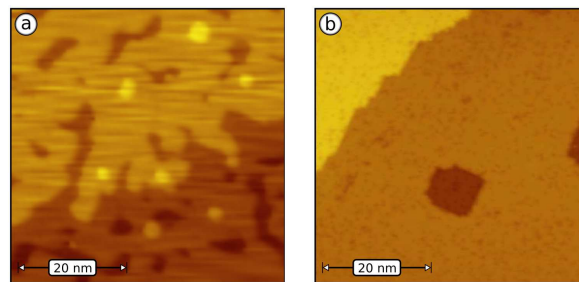

Figure 4.1.1: (a) As-deposited 7ML Co/Cu(100), (b) Co/Cu(100) after annealing at 370 K. Different colors denote different surface heights.[13]

structure with several different thicknesses and plateaus with diameters of a few nm. To reduce the impact of this disorder, the sample was annealed at 370 K to obtain a much smoother surface (cf. fig. 4.1.1b).[13] However, since films with less than 6 monolayers of Co on Cu(100) suffer from diffusion of Cu to the surface, while annealing,[13] the rugged structures are a necessary target for the structure generation algorithm. For the simulation of smooth annealed surfaces, an algorithm capable of avoiding a surplus amount of point defects would be favorable.

In the following, three major algorithms are presented, which were used for the creation of random structures. They are focused on performance and tunability of the resulting outputs. Because of their versatility and good comparison with the shown experimental surfaces, they were chosen over more complex algorithms, like kinetic Monte Carlo approaches.

4.1.1 Direct random structure generation and Fisher-Yates-Shuffle

The most straightforward approach to create random structures is the use of standard pseudorandom numbers (PRN). A given setup and equally distributed PRNs in the right-open interval $[0..1)$ – the output of most standard PRN generators – lead to two basic ways to create the desired random distribution of atoms.

The first method is the direct use of the random numbers by dividing the interval according to the probabilities of each species at a given site. For example, a probability of 40 % for species A and 60 % for species B would result in species A for all random numbers $p < 0.4$ and species B, otherwise. An important caveat of this method is the possibility of an unbalanced system, where the actual final composition does not meet the desired probabilities (if at all possible due to the limited amount of lattice positions in the supercell). In this case, an additional rebalancing step might be necessary (cf. eq. (5.1.1) in section 5.1.1).

The second method is the use of the Fisher-Yates-Shuffle (cf. algorithm 1).[55]

Algorithm 1 Fisher-Yates-Shuffle

Require: $a(1 : n)$ contains desired composition
    for $i = $ n **downto** 2 **do**
        $j \leftarrow$ random integer $1 \leq j \leq i$
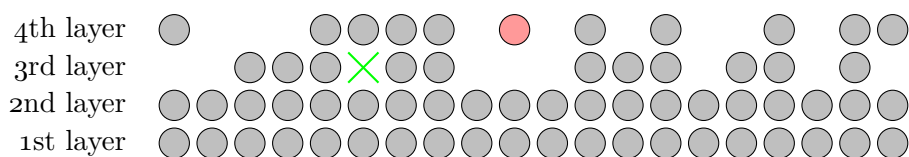   swap $a(i) \leftrightarrow a(j)$
    end for

Figure 4.1.2: Sideview of a possible random configuration for 3ML Co/Cu(001) where 50 % of the atoms from the 3rd layer are moved to the 4th layer. Possibly undesired floating atoms (red) and holes (green) were created.

For a given site in the original unit cell, a list of all corresponding positions in the supercell is created and filled with the desired composition of species in an arbitrary order. Applying the above example to a system with 25 sites would result in a list filled with 10 entries of A and 15 entries of B. Then, the Fisher-Yates-Shuffle will create a completely random permutation of this composition, which can then be used for further calculations.

Nevertheless, both methods can produce unphysical or undesired results. For example, the calculation of the system 3ML Co/Cu(001) where 50 % of Co atoms from the 3rd layer are moved to the 4th layer will most likely produce floating atoms or holes (see fig. 4.1.2).

4.1.2 Perlin noise method

This method is based on the popular Perlin noise,[56,57] which is commonly used for procedural creation of textures in computer graphics. The idea of this approach is to model the surface in terms of a smooth noise function. Some form of downsampling is applied to create a closed hilly surface which can be used in susceptibility calculations.

In order to create Perlin noise on a grid (in this case, the supercell), a second grid with a lower resolution is generated and its vertices are populated with random gradient vectors. Then, for every point in the supercell, i.e., the high-resolution grid, the contributions from the nearest gradient vectors are weighted to get a smooth noise function. In the 1-dimensional case (see fig. 4.1.3), the gradients from the vertices to the left and to the right are used and the resulting linear functions are interpolated. In the 2-dimensional case, the interpolation would be calculated from the 4 vertices of the circumscribing rectangle.

In fig. 4.1.3, it becomes apparent that this definition of Perlin noise results in the value "zero" at each of the low-resolution grid's vertices. For that reason,

an additional contribution of cubically interpolated regular noise, which is also defined at the vertices of the low-resolution grid, was added to the Perlin noise. The generation of the final structure from the Perlin noise is then achieved with the help of a level-set method (see fig. 4.1.4). In this method, one or more thresholds are defined and compared to the noise function at every position in the grid. The example in the figure can be interpreted as a 1-dimensional surface. Positions, where the noise function is less than the 1st level, would get assigned no atoms, positions with a value between the two levels get assigned one atom and positions with a value above the 2nd level get assigned two atoms.

This method has the same problems concerning stoichiometry as the purely random distribution of atoms. To get closer to the desired composition, the thresholds of the level set method can be adapted to fit the needs of the calculation. Another problem is the fact that this method can only be defined on a rectangular grid. As a result, the application of Perlin noise to a non-rectangular supercell, which is needed for calculations of, e.g., a hexagonal surface represented by rhombic unit cells, would result in a distorted grid with a strong anisotropy. In particular, one diagonal of the unit cell is longer than the other resulting in a structure, which is stretched along the longer diagonal. A possible solution is provided by simplex noise,[58] a later invention of Perlin, which is defined on a triangular grid.

4.1.3 Random structures from Voronoi tessellation

The third possible method is based on a Voronoi tessellation of the supercell.

To create the desired distribution of atoms in the supercell, some points P_k (which get marked with a species label) are put into the supercell and the Voronoi tessellation (with cyclical boundary conditions) is computed. The Voronoi regions R_k get the same species label as the corresponding points (see fig. 4.1.5). In the next step, the atoms in the supercell get assigned the appropriate species, determined by the species label of the Voronoi region at the corresponding position (see fig. 4.1.6).

Similar to the other methods, additional steps are needed to get the desired stoichiometry. This can be achieved using a weighted Voronoi tessellation and optimizing the weights w_k towards the desired composition:

$$R_k = \left\{ \boldsymbol{x} \in \mathbb{R}^n \mid d(\boldsymbol{x}, k) \leq d(\boldsymbol{x}, j), \ \forall \ j \neq k \right\}, \tag{4.1.1}$$

$$d(\boldsymbol{x}, k) = w_k \cdot \left\| \boldsymbol{x} - \boldsymbol{P}_k \right\|_2. \tag{4.1.2}$$

Due to the fact that the Voronoi regions are defined by the points in the supercell, there are no limitations to the shape of the supercell. Additionally, the size of
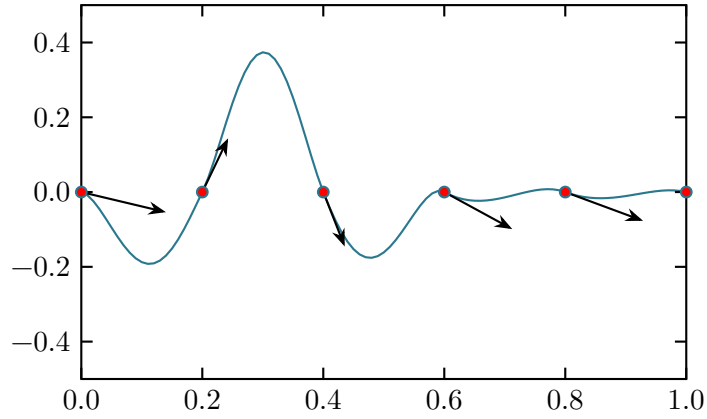
Figure 4.1.3: 1-dimensional Perlin noise (blue line). The low-resolution grid is defined at the red points and the gradient vectors are represented by arrows.
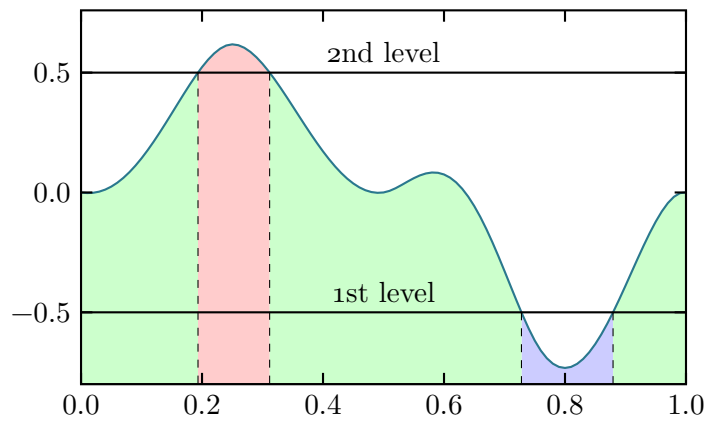

Figure 4.1.4: Level-set method with 2 levels at 0.5 and −0.5 applied to 1-dimensional Perlin noise. The blue area is below the 1st level, the green areas between both levels and the red area is above the 2nd level.
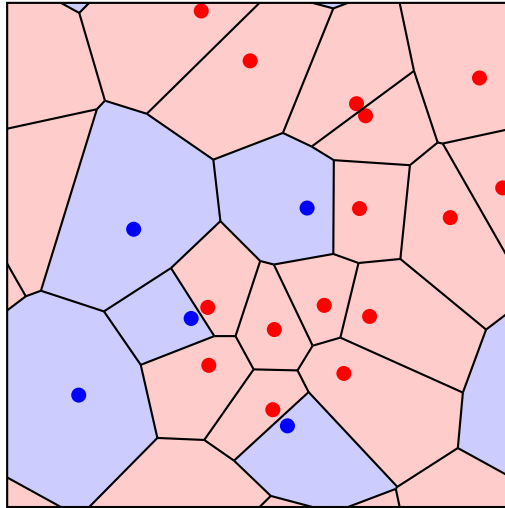
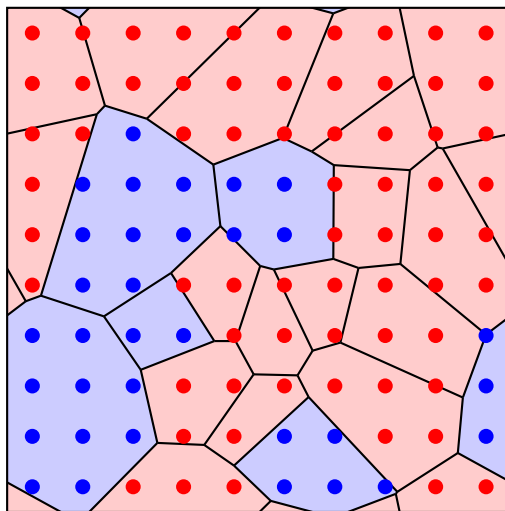Figure 4.1.5: 2-dimensional voronoi tesselation with 2 different species.

Figure 4.1.6: Resulting distribution of atom species from voronoi tesselation in fig. 4.1.5.

the generated structures (i.e., clusters of similar atoms) can be tuned by the composition and amount of the initial points $\boldsymbol{P}_k$.

4.1.4 Application of generators

From the properties of the three methods, it is straightforward to determine which method should be used for a given system: The 2-dimensional system of 7ML Co/Cu(100) could be created with the Perlin method. Depending on the size of the surface's features, a varying resolution of the coarse grid can be used. While the annealed system can be obtained from the algorithm as described, the unannealed system could be generated with a high-resolution "coarse" grid to effectively switch of its smoothing capability. On the other hand, a purely random composition might produce acceptable results for the unannealed structure, but this was not used in actual calculations.

For 3-dimensional systems, the most important property is the short-range order of the system. If the atoms of the different species are randomly distributed, a purely random generation is preferred, and if a clustering of similar atoms is observable, the Voronoi tessellation is the method of choice. In the latter case, a 3-dimensional variant of the Perlin method would also be possible, but this was not implemented because of the limitations apparent from the 2-dimensional version.

4.2 Analytic Continuation

The calculation of magnon dispersion relations is additionally bound to the problem of diverging poles on the real energy axis. In the calculations of section 5.1, this problem manifests itself in slowly converging spectra (i.e., a huge amount of random configurations is needed to obtain a smooth spectrum). It is possible to work around this problem by adding a small imaginary part to the energy, but the resulting spectra show artificially broadened peaks. For example, fig. 4.2.1 shows the increasing noise in the spectra of an $Fe_{0.7}Al_{0.3}$ alloy when the artificial broadening γ, i.e., the imaginary part of the energy, is reduced from $\gamma_1 = 5\,\text{meV}$ to $\gamma_2 = 0.1\,\text{meV}$.

A possibility to circumvent both problems, i.e., the noise for small imaginary energies and the increased artificial broadening for larger imaginary energies, is given by the analytic continuation. The idea of the analytic continuation is to calculate the susceptibility for energies with a higher imaginary part, which allows the sufficient convergence of the spectrum, and to shift this result towards the real axis to get a better converged susceptibility (see fig. 4.2.2). Figure 4.2.1
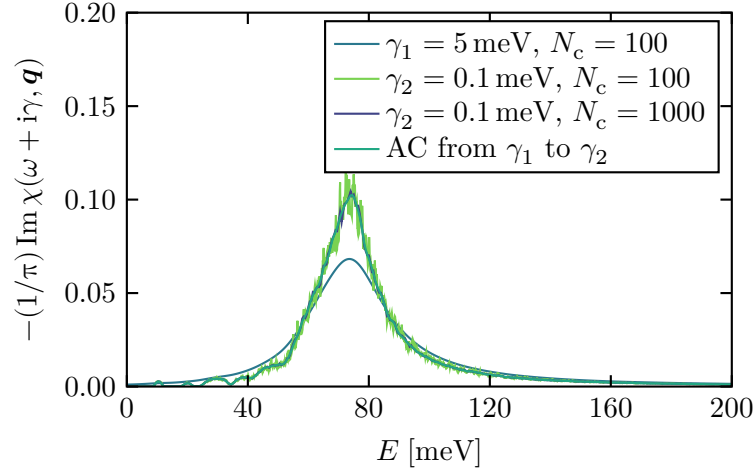
Figure 4.2.1: Comparison of susceptibility spectra for an $Fe_{0.7}Al_{0.3}$ alloy with two different artificial broadenings $\gamma_1 = 5\,\mathrm{meV}$ and $\gamma_2 = 0.1\,\mathrm{meV}$. The spectrum with the artificial broadening γ_1 is analytically continued towards an artificial broadening of γ_2.

shows the analytic continuation applied to the previously calculated susceptibility with $\gamma_1 = 5\,\mathrm{meV}$. The resulting spectrum contains much less numerical noise than the directly calculated counterpart with $\gamma_2 = 0.1\,\mathrm{meV}$.

The reasoning behind the analytic continuation is the Cauchy-Riemann differential equations,

$$\frac{\partial u}{\partial x} = \frac{\partial v}{\partial y}, \tag{4.2.1}$$

$$\frac{\partial u}{\partial y} = -\frac{\partial v}{\partial x}, \tag{4.2.2}$$

which can be applied to a complex function $f(z)$ as

$$\mathrm{i}\frac{\partial f}{\partial x} = \frac{\partial f}{\partial y}. \tag{4.2.3}$$

This relation is obtained by understanding the arguments x and y as the real and imaginary part of the argument z, respectively. Similarly, the function f is composed by its real and imaginary part u and v, respectively.

In the context of the analytic continuation of the magnetic susceptibility, this means that any interpolation of the susceptibility in the direction of the real
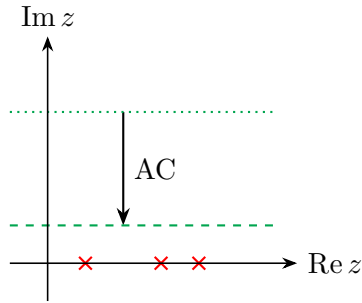
Figure 4.2.2: Due to poles on the real axis (red crosses), the susceptibility has to be calculated at complex energies. Analytic continuation can be used to interpolate a solution closer to the real axis.

energy should have locally the same derivative in both directions. Depending on the convergence of the interpolation, this allows the extrapolation of the function in direction of imaginary energy towards the real axis.

Below, several methods are presented, which can be used to perform the analytic continuation. While three of these methods are directly based on the Cauchy-Riemann differential equation, two other methods are trying to reverse the broadening, which results from the added imaginary energy.

4.2.1 Padé approximation

The first approach for analytic continuation is the use of the Padé approximant of the susceptibility. To perform the analytic continuation, the calculated susceptibility is interpolated around the energy of interest and the Padé approximant is then used to calculate the value for a smaller imaginary part of the energy.

In general, a Padé approximant is determined by the order of its numerator m and denominator n:

$$f(x) \approx R_{[m/n]}(x) = \frac{P_m(x)}{Q_n(x)} = \frac{1 + \sum_{j=1}^{m} a_j x^j}{\sum_{j=0}^{n} b_j x^j}. \qquad (4.2.4)$$

However, the exact definition of the Padé approximant is not standardized. Deviating from the above definition, where the coefficient $a_0 = 1$ is fixed, often the constraint $b_0 = 1$ is used instead. The result of this difference is simply a constant factor scaling all coefficients.

For a given analytic function, a valid approach for determining the $(m+n+1)$ coefficients would be the comparison of the first $(m+n)$ derivatives and the

actual functions themselves, around some evaluation point x_0. However, in the case of numerical data, like for the calculated susceptibility, this is not possible.

An alternative approach is the solution of the system of equations given by $N = (m + n + 1)$ data points x_i with their corresponding values y_i:

$$f(x_i) = y_i = \frac{P_m(x_i)}{Q_n(x_i)}. \tag{4.2.5}$$

By rearranging this system of equations by moving the sums to the left-hand side, it is easily possible to derive a matrix equation for the set of expansion coefficients a_i and b_i:

$$\begin{pmatrix} x_1 & x_1^2 & \cdots & x_1^m & y_1 & y_1 x_1 & y_1 x_1^2 & \cdots & y_1 x_1^n \\ x_2 & x_2^2 & \cdots & x_2^m & y_2 & y_2 x_2 & y_2 x_2^2 & \cdots & y_2 x_2^n \\ \vdots & \vdots & & \vdots & \vdots & \vdots & \vdots & & \vdots \\ x_N & x_N^2 & \cdots & x_N^m & y_N & y_N x_N & y_N x_N^2 & \cdots & y_N x_N^n \end{pmatrix} \cdot \begin{pmatrix} a_1 \\ \vdots \\ a_m \\ b_0 \\ \vdots \\ b_n \end{pmatrix} = \begin{pmatrix} 1 \\ \vdots \\ 1 \\ 1 \\ \vdots \\ 1 \end{pmatrix}. \tag{4.2.6}$$

The matrix in this equation contains two blocks, which are responsible for the numerator and the denominator, respectively. These blocks are similar to Vandermonde matrices, which are well known from polynomial interpolation, but avoided because of their bad condition. It is possible to circumvent the resulting numerical problems by using stepwise interpolation and, thus, smaller matrices. Alternatively, there is also a recursive algorithm, similar to the Neville interpolation, which provides are more stable method to calculate the Padé approximation.[59] This recursive algorithm allows the construction of a single Padé approximation for several hundred points, without any noticeable numerical error.

Another caveat of the Padé approximation are occasional zeros of numerator and denominator, although the interpolated function does not have a pole. In theory, both zeros should cancel out, but numerical noise in the calculation can lead to sharp spikes in the resulting interpolation.

4.2.2 Finite difference method

Another approach for the analytic continuation, which is based on the Cauchy-Riemann differential equations, is the application of finite differences. An approximation of the derivative is calculated along (i.e., parallel to) the real energy axis and then a step towards the real axis is performed.[60,61]

The principle approach is the determination of an approximate formula for the derivative by application of the Taylor expansion. For example, the derivative along the real energy axis could be calculated with 5 data points, while the derivative along the imaginary energy axis is done with an Euler step. Assuming a step width of $h = \Delta E$ in both directions, the energy can be defined as

$$E = E_0 + x\,h + y\,\mathrm{i}h, \qquad\qquad f(E) = f_{x,y}. \qquad (4.2.7)$$

The Taylor expansion around E_0, i.e., for $x = y = 0$,

$$
\begin{aligned}
f_{-2,0} &= f_{0,0} \;-2hf'_{0,0} + 2h^2 f''_{0,0} - \tfrac{4}{3}h^3 f^{(3)}_{0,0} + \tfrac{2}{3}h^4 f^{(4)}_{0,0} - \tfrac{4}{15}h^5 f^{(5)}_{0,0} + \dots, \\
f_{-1,0} &= f_{0,0} \;-hf'_{0,0} + \tfrac{1}{2}h^2 f''_{0,0} - \tfrac{1}{6}h^3 f^{(3)}_{0,0} + \tfrac{1}{24}h^4 f^{(4)}_{0,0} - \tfrac{1}{120}h^5 f^{(5)}_{0,0} + \dots, \\
f_{0,0} &= f_{0,0}, \\
f_{1,0} &= f_{0,0} \;+hf'_{0,0} + \tfrac{1}{2}h^2 f''_{0,0} + \tfrac{1}{6}h^3 f^{(3)}_{0,0} + \tfrac{1}{24}h^4 f^{(4)}_{0,0} + \tfrac{1}{120}h^5 f^{(5)}_{0,0} + \dots, \\
f_{2,0} &= f_{0,0} \;+2hf'_{0,0} + 2h^2 f''_{0,0} + \tfrac{4}{3}h^3 f^{(3)}_{0,0} + \tfrac{2}{3}h^4 f^{(4)}_{0,0} + \tfrac{4}{15}h^5 f^{(5)}_{0,0} + \dots, \\
f_{0,-1} &= f_{0,0} \;-\mathrm{i}hf'_{0,0} - \tfrac{1}{2}h^2 f''_{0,0} + \mathrm{i}\tfrac{1}{6}h^3 f^{(3)}_{0,0} + \tfrac{1}{24}h^4 f^{(4)}_{0,0} - \mathrm{i}\tfrac{1}{120}h^5 f^{(5)}_{0,0} + \dots,
\end{aligned}
$$
$$(4.2.8)$$

can be inserted in the finite difference formula:

$$\mathrm{i}\underbrace{\left(\tilde{a}\,f_{-2,0} + \tilde{b}\,f_{-1,0} + \tilde{c}\,f_{0,0} + \tilde{d}\,f_{1,0} + \tilde{e}\,f_{2,0}\right)}_{\partial_x f} = \underbrace{\tilde{g}\,f_{0,0} + \tilde{k}\,f_{0,-1}}_{\partial_y f}, \qquad (4.2.9)$$

$$a\,f_{-2,0} + b\,f_{-1,0} + c\,f_{0,0} + d\,f_{1,0} + e\,f_{2,0} = f_{0,-1}. \qquad (4.2.10)$$

Comparison of coefficients, i.e., with respect to the derivatives of f, provides a system of equations for the coefficients a to e,

$$
\begin{pmatrix}
1 & 1 & 1 & 1 & 1 \\
-2 & -1 & 0 & 1 & 2 \\
2 & \tfrac{1}{2} & 0 & \tfrac{1}{2} & 2 \\
-\tfrac{4}{3} & -\tfrac{1}{6} & 0 & \tfrac{1}{6} & \tfrac{4}{3} \\
\tfrac{2}{3} & \tfrac{1}{24} & 0 & \tfrac{1}{24} & \tfrac{2}{3}
\end{pmatrix}
\cdot
\begin{pmatrix}
a \\ b \\ c \\ d \\ e
\end{pmatrix}
=
\begin{pmatrix}
1 \\ -\mathrm{i} \\ -\tfrac{1}{2} \\ \mathrm{i}\tfrac{1}{6} \\ \tfrac{1}{24}
\end{pmatrix},
\qquad (4.2.11)
$$

which in turn yields the expression

$$f_{0,-1} \approx \tfrac{1-2\mathrm{i}}{12}f_{-2,0} - \tfrac{5-5\mathrm{i}}{6}f_{-1,0} + \tfrac{5}{2}f_{0,0} - \tfrac{5+5\mathrm{i}}{6}f_{1,0} + \tfrac{1+2\mathrm{i}}{12}f_{2,0}. \qquad (4.2.12)$$
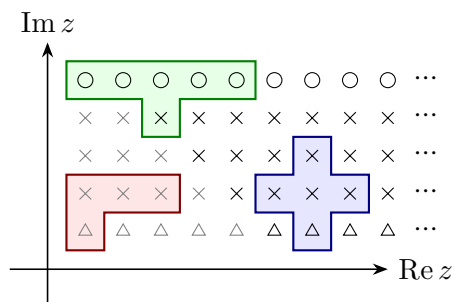
Figure 4.2.3: Application of finite difference formulae to calculate the analytic continuation. Equation (4.2.12) is marked in green, eq. (4.2.13) is marked in blue and an asymmetric formula for recovery of edge points is marked in red. The calculated susceptibility ($\circ$) is analytically continued via intermediate steps ($\times$) to an interpolation close to the real axis ($\triangle$). The gray points could be recovered with asymmetric finite difference formulae.

Since it was assumed before that the step width along both the real and imaginary axis should be equal, several finite difference steps might be necessary to calculate an interpolation sufficiently close to the real axis. In order to keep a larger data range – the above formula "destroys" two data points at each end of the dataset – and to have a better approximation for the derivative along the imaginary energy axis, Hass et al.[60] proposed the use of the centered derivative formula

$$f_{0,-1} = 4f_{0,0} - f_{0,1} - f_{-1,0} - f_{1,0}, \qquad (4.2.13)$$

instead of an Euler step for further steps of the analytic continuation (see fig. 4.2.3). However, this formula still suffers from a loss of one data point per continuation step. The lost data points can be recovered by using asymmetric finite difference formulae, which can be obtained by solving the above system of equations for, e.g., $f_{0,0}$, $f_{1,0}$, $f_{2,0}$ and $f_{0,-1}$.

Using this method, one has to keep in mind that by successive execution of continuation steps, an accumulation of errors can appear, which renders the results unusable.[61] It is also necessary to mention that by trying to improve the results by inclusion of more data points in the finite difference formulae, it is likely that the accumulation of numerical errors is sped up.

4.2.3 Spline approximation

The spline approximation is another application of the Cauchy-Riemann differential equations. This approximation is a polynomial interpolation, which consists of cubic polynomials S_i in each interval of points $[x_i, x_{i+1}]$ $(i = 0 \ldots n)$:[62]

$$S_i(x) = a_i + b_i(x - x_i) + c_i(x - x_i)^2 + d_i(x - x_i)^3, \quad x \in [x_i, x_{i+1}]. \quad (4.2.14)$$

In the case of natural splines, the coefficients a_i, b_i, c_i and d_i are determined by the boundary conditions at the boundaries of the data set,

$$S''(x_0) = 0, \qquad\qquad S''(x_n) = 0, \qquad\qquad (4.2.15)$$

and at the boundaries of the intervals

$$S_{i-1}(x_i) = S_i(x_i), \quad S'_{i-1}(x_i) = S'_i(x_i), \quad S''_{i-1}(x_i) = S''_i(x_i), \quad i = 1 \ldots (n-1). \quad (4.2.16)$$

The condition that the original data should be exactly replicated $(S_i(x_i) = y_i)$ immediately yields $a_i = y_i$. The coefficients c_i are then determined by solving a tridiagonal matrix, which can be achieved very efficiently. The remaining coefficients b_i and d_i can be calculated directly from c_i and c_{i+1}.

4.2.4 Fourier transformation

A completely different approach was proposed by Natoli et al.[63] The authors propose to use the Fourier transform to perform the analytic continuation of an electron Green's function.

The principle idea can be summarized as the application of a time shift in the complex domain,

$$\mathcal{F}[f(x - a)] = \mathrm{e}^{-\mathrm{i}ak}\mathcal{F}[f(x)], \qquad\qquad (4.2.17)$$

to "move" the function towards the real axis. By analysis of the four possible cases of sign combinations for k and the imaginary energy, the master equation

$$G(x, 0^\pm) = \frac{1}{2\pi}\mathcal{F}^{-1}\left[\mathrm{e}^{|k||y|}\mathcal{F}[G(x', y)]\right] \qquad\qquad (4.2.18)$$

could be derived. The exponential $\mathrm{e}^{|k||y|}$ shows clearly the ill-posed nature of this approach, including the exponential amplification of any error in the calculated Green's function $G(x', y)$.

It is further proposed to perform the calculations by application of the Fast-Fourier-Transform (FFT). To reduce possible numerical errors and noise, it is necessary to choose an appropriate step width for the FFT, which fits the desired shift in direction of imaginary energy $\Delta_{\mathrm{x}} \approx |y|$. Additionally, it is proposed that an additional term is included to damp oscillations of higher frequency:

$$G(x, 0^{\pm}) = \frac{1}{2\pi} \mathcal{F}^{-1}\left[\mathrm{e}^{|k||y|}\mathrm{e}^{-\frac{4}{\pi^2}\Delta_{\mathrm{x}}^2 k^2} \mathcal{F}\left[G(x', y)\right]\right]. \tag{4.2.19}$$

4.2.5 Stochastic Optimization Method

The method proposed by Mishchenko[64] is in principle similar to the FFT method, since a direct relation between the calculated function $G(x')$ and the analytically continued function $A(x)$ is used:

$$G(x') = \int_{-\infty}^{\infty} \mathrm{d}x\, \mathcal{K}(x, x')A(x). \tag{4.2.20}$$

The integration kernel $\mathcal{K}$ describes a smearing of the function A on the real axis by shifting it towards a larger imaginary energy y resulting in G.

Given the kernel $\mathcal{K}$, an inverse approach is taken to determine $A(x)$: It is parametrized as a sum of rectangles, whose smearing can ideally be determined analytically, and by successive modification of these parameters, a set of approximations $\tilde{A}$ of $A(x)$ is determined. The application of the smearing integral to the approximations $\tilde{A}$ yields the set of approximations $\tilde{G}$ for the calculated function $G(x')$. The objective function

$$D = \sum_{m=1}^{M} |\Delta(m)|, \tag{4.2.21}$$

defined by the deviation function

$$\Delta(m) = \frac{G(m) - \tilde{G}(m)}{\mathcal{S}(m)}, \tag{4.2.22}$$

which relates the measured function G, the approximated function $\tilde{G}$ and the known standard deviation $\mathcal{S}$, provides a way to estimate the original function as a selective mean over the set of approximations $\tilde{A}$:

$$A(x) = \frac{1}{L_{\mathrm{good}}} \sum_{j=1}^{L} \theta\left\{2\min\left[D(\tilde{A}_j)\right] - D(\tilde{A}_j)\right\}\tilde{A}_j(x), \tag{4.2.23}$$

$$L_{\mathrm{good}} = \sum_{j=1}^{L} \theta\left\{2\min\left[D(\tilde{A}_j)\right] - D(\tilde{A}_j)\right\}. \tag{4.2.24}$$

4.2.6 Implementation, test and comparison

Within the scope of this thesis, several of the above mentioned methods were implemented, to provide an analytic continuation for susceptibility calculations. The implemented methods include:

1. Padé approximation with matrix method (section 4.2.1)

2. Padé approximation with recursive method (section 4.2.1)

3. Finite Difference method (section 4.2.2)

4. Spline-Approximation (section 4.2.3)

5. Fast-Fourier-Transform method (section 4.2.4)

In the following part, these five methods are compared by application to two test functions: At first, an analytic function, where the analytic continuation is naturally known, is tested. Afterwards, an actually measured susceptibility spectrum, where the analytic continuation is known from calculations with very small imaginary energy, is compared.

The Padé approximation, which was calculated within the matrix method, was implemented with $m = 2$ and $n = 2$. This means that the interpolation was achieved by interpolating the nearest 5 data points, which are usually centered around the requested data point, but at the edges of the data set. The recursive Padé approximation by Press et al.[59] was used to interpolate the whole dataset at once.

In order to provide more flexibility for the finite difference method, an anisotropic step width was used. In particular, instead of the isotropic difference $\Delta_x = \Delta_y = h$, the energy differences $\Delta_{x/y}$ were used directly. The stability of the method could be improved by splitting the step width in direction of imaginary energy into multiple steps (n) to get an approximate isotropic step width $\Delta_x \approx h_y = \Delta_y/n$.

Because of the flexibility of the spline approximation, no special requirements were necessary for this method.

However, the FFT method requires that the step widths along the real and imaginary energy axes are roughly the same. The following first example was constructed to fit this requirement approximately. For the second example, the number of data points was halved for this method to allow a larger step towards the real energy axis. The omitted points were reinterpolated afterwards by Neville interpolation.

Analytic function

The first test is an analytic function, whose analytic continuation is, naturally, already known. Because of the nature of the susceptibility, the selection of Lorentzians is a good choice. The test function consists of three Lorentzians: The first two peaks result from peaks on the real axis and should become sharper by performing the analytic continuation towards the real axis. The third peak results from two peak symmetrically off the real axis and should become broader:

$$f(z) = \underbrace{\frac{0.2}{1 + (z - (1 + i))^2}}_{\text{1st peak}} + \underbrace{\frac{1}{0.1 + (z - (2 + 0.1i))^2}}_{\text{2nd peak}} + \underbrace{\frac{1}{0.1 + (z - 3)^2}}_{\text{3rd peak}}. \quad (4.2.25)$$

The result in fig. 4.2.4 shows clearly, that both versions of analytic continuation by Padé approximation give excellent results. While the matrix-based method is perfectly suitable for the approximation of the local poles (the difference in the height of the first pole is less than $1\,\text{‰}$), the recursive approximation can fit the data exactly achieving the same outcome as the analytic expression.

In contrast to this, the other methods are failing. While the finite difference method and the spline approximation – both are based on polynomials – show very good agreement for both broad peaks, the narrow peak is underestimated with oscillations at the base of the peak.

The FFT method is even further off and fails to correctly continue all three peaks. It is important to note that, while the continuation trend for the first two peaks is correct, the third peak got more narrow, too. This is an artifact related to the prerequisites of the method, which, in short, require the peaks to be on the real axis.

Susceptibility

The second example is the continuation of an actual susceptibility spectrum for a system of 4ML Co on a Cu(111) surface, where some Co atoms from the surface layer have moved to the layer above, effectively building an island structure. The susceptibility was calculated for two imaginary energies $\text{Im}\, z_1 = 0.01\,\text{eV}$ and $\text{Im}\, z_2 = 0.001\,\text{eV}$. For all methods, but the FFT method, 521 data points were used, the FFT method was restricted to 261 data points.

In fig. 4.2.5, it is again apparent that both Padé approximants yield excellent results for the analytic continuation. However, the results of the matrix-based method disagree slightly in the range $E = 0.00 \ldots 0.07\,\text{eV}$. At this point, one should start to consider the necessary computation time. While, for this example,
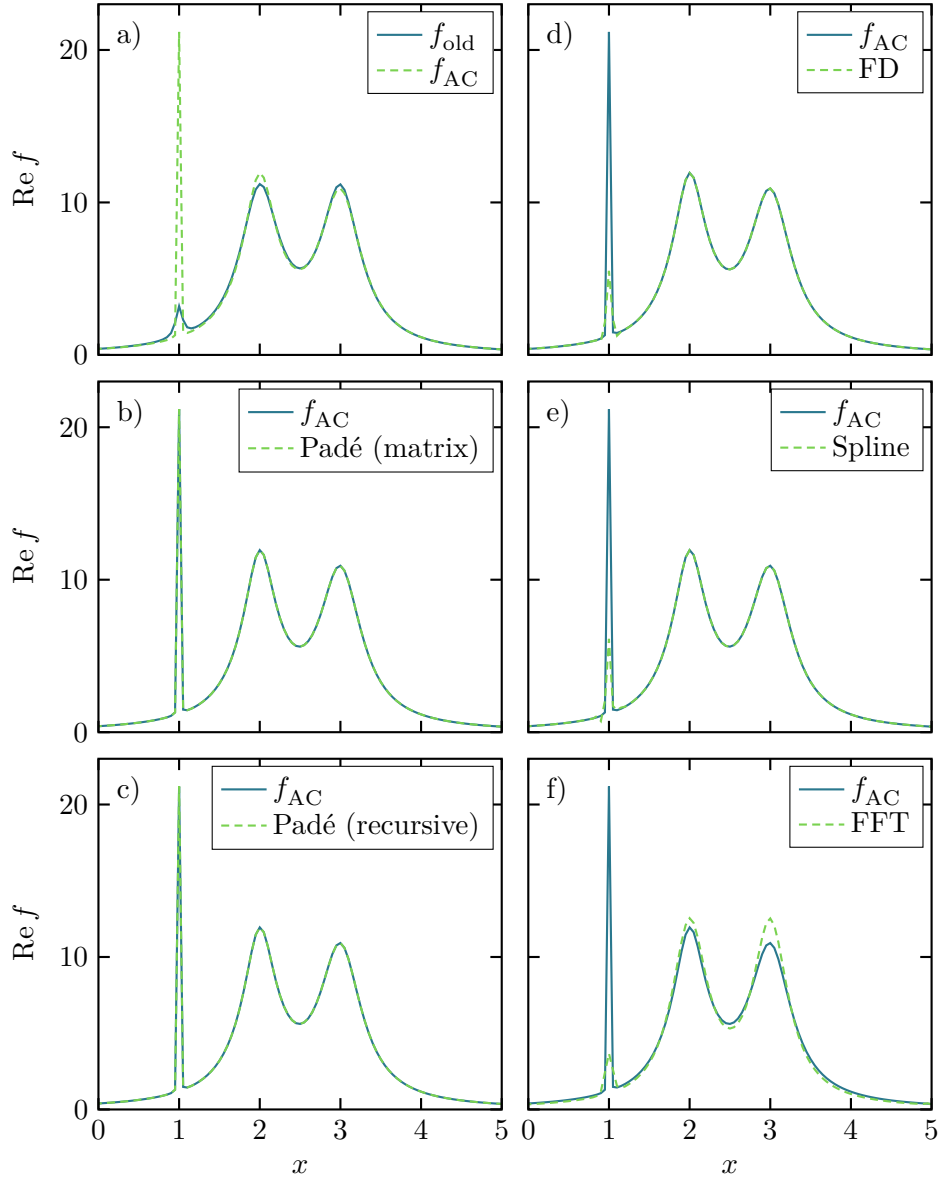
Figure 4.2.4: Analytic continuation of eq. (4.2.25) with $\Delta_{\mathrm{x}} = 0.05$ from $\mathrm{Im}\, z = 0.05$ (f_{old}) to $\mathrm{Im}\, z = 0.005$ (f_{AC}). (b)-(f) Comparison of the analytically continued functions with the exact result f_{AC}.
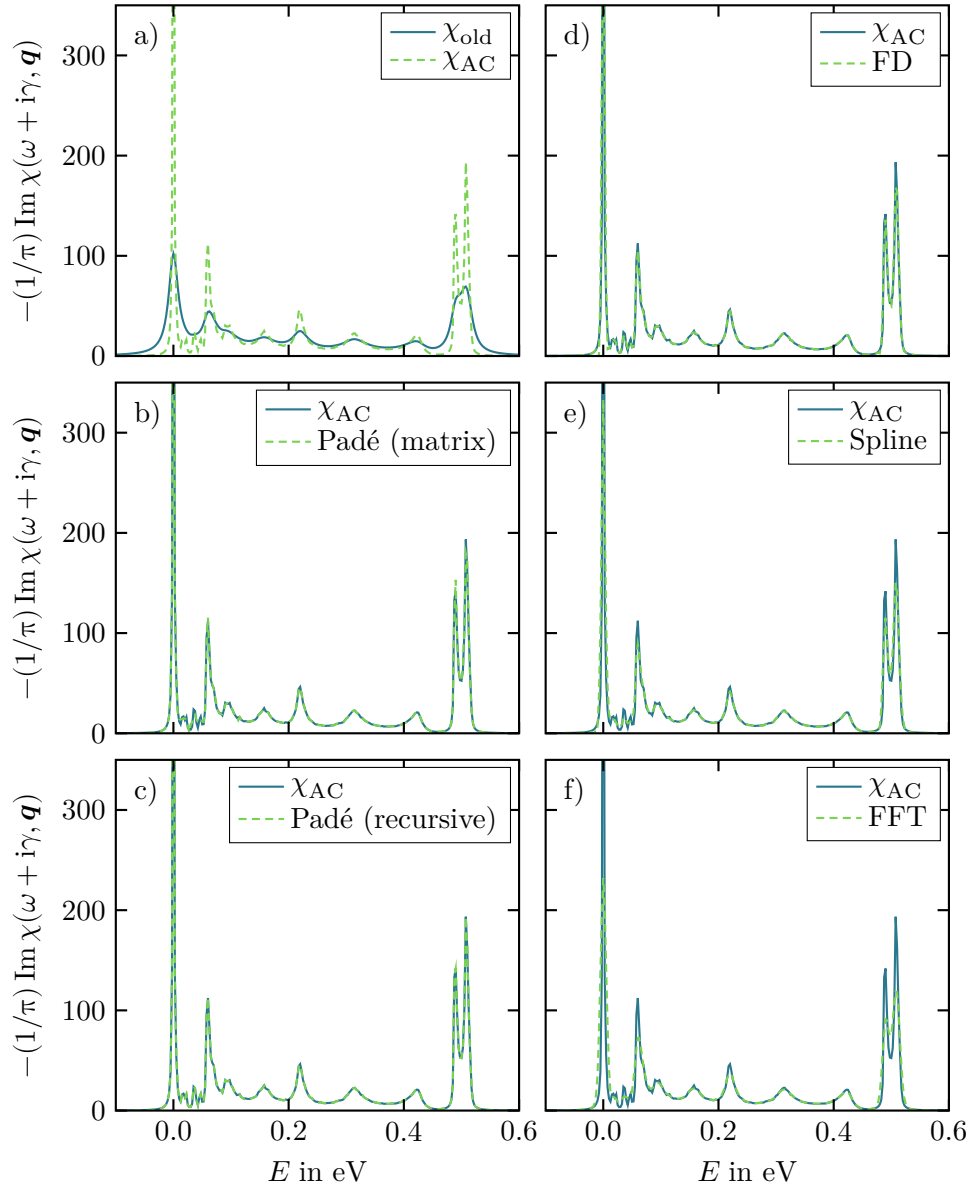
Figure 4.2.5: Analytic continuation of the susceptibility of 4ML Co on Cu(111). (a) The calculated spectra at $\mathrm{Im}\,z = 0.01\,\mathrm{eV}$ (χ_{old}) and $\mathrm{Im}\,z = 0.001\,\mathrm{eV}$ (χ_{AC}). (b)-(f) Analytic continuation of χ_{old} compared to the calculated result χ_{AC}.

the solution of 521 systems of equations consisting of 5 equations can be found very quickly, the calculation of 521 interpolations by recursing over all 521 data points, requires a more serious computational effort.

Similar to the results of the analytic function, the other three methods showed worse results. However, the finite difference approach resembles most of the peaks with surprising accuracy, while the biggest issue are the oscillations at the base of the narrow peaks (e.g., around the zero-peak and next to the peak at $0.5\,\text{eV}$). In comparison to this, the spline approximation yields fewer oscillations but does not correctly describe the sharp peaks. The worst method is again the FFT method, which fails to accurately reproduce the analytically continued peaks. Nevertheless, the continuation shows the correct trend and fails most likely, because of the necessary stability adjustments (cf. eqs. (4.2.18) and (4.2.19)).

In conclusion, the Padé approximation, especially the iterative implementation from Press et al.,[59] is still the best tested method for the analytic continuation of the magnetic susceptibility. The methods based on the spline approximation and the FFT yield results, which are too bad to be considered as a replacement for the Padé approximation. Solely, the finite-difference-based method might be considered for the analytic continuation, because its computational requirements are, depending on the applied finite-difference formula, very low and grow only linearly with the number of points and necessary analytic continuation steps (cf. the number of steps n on page 49).

4.3 Optimization techniques

Similar to the analytic continuation, the field of optimization techniques is already well-investigated. However, it is always a challenge to select the best-suited methods for the optimization of an existing problem.

For the optimization of plasmonic nanostructures, a two-step approach was used to overcome the principal problems of many optimization algorithms: Most algorithms are either only suitable for local searches and get stuck in local minima within the search space, or they are simply not precise enough, to get an acceptable final solution. Hence, the optimization was started by application of genetic algorithms and afterwards refined with the simplex algorithm of Nelder and Mead.[65]

Genetic algorithms are a class of algorithms, which are motivated by natural evolution processes. The general idea is the creation of a population of different configurations, which ideally evolves towards the global minimum of an objective function (also called fitness) by performing biologically motivated modifications

of the configurations. These modifications could be intermixing of two config-
urations' parameters (similar to breeding), simply the random variation of a
single parameter of a configuration (analog to mutation), or even the generation
of completely new configurations. The repeated generation of new generations,
the selective dropping of "bad" configurations (i.e., configurations with a poor
fitness), and the selection of the configurations with good fitness (i.e., the concept
of elitism) should result in the improvement of the overall fitness. In combina-
tion with the large amount of individual configurations, this should lead to a
convergence towards the vicinity of the global minimum.

However, it is difficult to use the random-based genetic algorithms, to system-
atically converge to the exact position of a minimum. Therefore, the simplex
algorithm is used to perform this necessary step. The simplex algorithm for a
system with n parameters can be started from a single configuration, by gener-
ating n additional configurations as small deviations from the single one, or by
selecting the $n + 1$ best configurations from the genetic algorithms. These $n + 1$
configurations are the vertices of a simplex in the parameter space. The optimiza-
tion is performed by the systematical replacement of the vertices with the worst
fitness. If no better vertex is found, the whole simplex gets contracted toward its
center. By the repeated optimization of the simplex' vertices, the whole vertex
converges towards a local minimum, which should be the global minimum, due
to the previous optimization with genetic algorithms. The big advantage of this
method is the low number of necessary evaluations of the objective function and
the waiver of derivatives.

The objective function is usually a measurable quantity. In the field of
plasmonic nanostructures, this could be the field strength at a certain position,
or, what is used later for the optimization of plasmonic filters, the ratio of the
electric field's magnitude for two different wavelengths

$$F = \log\left(\frac{|\boldsymbol{E}_{\lambda_1}|}{|\boldsymbol{E}_{\lambda_2}|}\right). \tag{4.3.1}$$

This particular definition was inspired by typical near-field enhancement opti-
mizations, where the intensity at a certain point gets compared to the intensity of
the incoming plane wave excitation,[66] and the optimization of surface structures
for surface enhanced raman spectroscopy (SERS).[67]

The biggest problem when using the genetic algorithms is the quick reduction
in search space, due to the intermixing of the configurations. It is possible to
avoid this problem by massively increasing the number of used configurations,
or by application of more sophisticated algorithms, which preserve/restore the

spanned parameter space. A good method to achieve this is the principal component analysis (PCA). PCA provides a numerical technique to detect lost dimensions in the search space. Therefore, the eigensystem of the covariance matrix of the configurations is analyzed with respect to vanishing eigenvalues. The corresponding lost dimensions can be recovered by random sampling of new configurations. One method that implements this dimension-recovering technique (and a variant of the simplex algorithm) is the shuffled complex evolution with principal components analysis-University of California at Irvine (SP-UCI), which was also used for the optimization of plasmonic nanostructures.[68]

5 Application of multiple scattering approaches to investigate magnonic, plasmonic and electronic systems

In the following chapter, the previously presented multiple scattering approaches for magnons, plasmons and electrons are applied to selected physical systems. As far as possible, the calculated results are compared to existing experimental or theoretical findings to verify the correctness of the used approach.

5.1 Magnons in disordered systems

The study of magnons in disordered systems was performed with respect to diluted magnets.[T1] Diluted magnets are systems, where the magnetic atoms were partially substituted by non-magnetic atoms. From the theoretical point of view, the investigation of diluted magnets has the advantage that only a subset of the possible interactions in the system has to be considered in comparison to an alloy of several magnetic atoms. This research is motivated by several important systems like the ultrastrong low-density steels based on FeAl[69] or the class of diluted magnetic semiconductors with respect to their application in spintronics.[70–73]

5.1.1 Dimensionality studies

Besides the typical bulk systems, like the aforementioned FeAl alloy, there is also interest in the investigations of lower-dimensional systems like the thin-film systems of Fe/Ir(001)[31] or Co/Cu(001).[1] However, the behavior of magnetic systems is highly dimensionality dependent: Important features include the differing behavior of the Stoner density of states[1] and the proposed absence of magnetic order in 1- and 2-dimensional Heisenberg systems.[74,75]
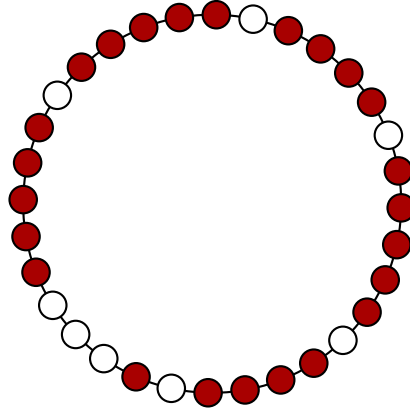
Figure 5.1.1: 1-dimensional diluted magnet with magnetic (filled circles) and non-magnetic atoms (empty circles).[T1]

The dimensionality studies are performed for a hypothetical material with only nearest-neighbor magnetical interactions of $J = 1/8$. Due to the quick-diminishing nature of the interactions, this model is often a good approximation for a real system, while allowing an easy theoretical description.

1-dimensional system

A 1-dimensional system can be described as a ring of atoms (see fig. 5.1.1). The shown structure was generated by placing magnetic atoms with probability $c = 0.7$ on a total of $N_\mathrm{s} = 32$ sites, without limiting their actual composition (here: $24/32 = 0.75$). Apart from the fact that an occupation of $c = 0.7$ is impossible to achieve in a system of 32 atoms, this allows the inclusion of systems with similar, but differing, occupation rates, which might appear locally in any actual system. In larger simulated systems, this is of no bigger concern anymore, because the relative standard deviation, for what is essentially a Bernoulli process,

$$\frac{\sigma}{n} = \frac{\sqrt{n\,c(1-c)}}{n} \propto \frac{1}{\sqrt{n}} \tag{5.1.1}$$

reduces like $n^{-\frac{1}{2}}$. In a typical 3-dimensional cell with $N_\mathrm{s} = 32^3$ and a concentration of $c = 0.7$, more than $95\,\%$ of compositions are differing less than $1\,\%$ from the desired concentration.

In this 1-dimensional system, every atom can interact at most with its two neighboring atoms, resulting in isolated magnetic clusters. The localized modes

in these clusters manifest themselves in the spin excitation spectrum (fig. 5.1.2a) as a series of sharp peaks, whose line-width is only induced by the artificial broadening of $\gamma = 10^{-2}$. Each peak corresponds to a localized spin excitation with infinite lifetime. The height of the peaks is a result of the number of states, as well as the overlap integral between the particular spin excitation and the plane wave with wave vector $\boldsymbol{q}$.

By increasing the number of sites N_s, more different clusters appear in the system resulting in more peaks at different energies (cf. fig. 5.1.2a for $N_\mathrm{s} = 128$). A further increase of the number of sites will finally lead to convergence (see fig. 5.1.2b for $N_\mathrm{s} = 2048$ and $N_\mathrm{s} = 4096$).

A big problem with this approach is the massive computation time, which is necessary to calculate the spectrum. The computation has essentially a complexity of $\mathcal{O}(N_\mathrm{s}^3)$, due to the inversion of the susceptibility matrix $\underline{\boldsymbol{\chi}}$ in eq. (3.1.50). This could be improved by appropriate algorithms like the Strassen algorithm for matrix multiplication, or by algorithms, which exploit the sparse structure of the matrices. To work around this problem, several configurations N_c with intermediate size are calculated and their respective susceptibilities averaged. This has the added benefit that it is possible to calculate a standard deviation for the susceptibility.

Figure 5.1.2b shows the good agreement of a single huge system ($N_\mathrm{s} = 4096$, $N_\mathrm{c} = 1$) compared to the average of several intermediate-sized systems ($N_\mathrm{s} = 128$, $N_\mathrm{c} = 100$) with small differences around $\omega = 0.4$ and $\omega = 0.6$. This behavior is expected since the isolated chains do not interact with each other and can be calculated separately, while the smaller system is restricted by its size and the occupation ratio to chains of a shorter maximum length. In particular, in a system with $N_\mathrm{s} = 32$ atoms, a continuous chain of 30 atoms is unlikely because it is far off the desired concentration of $c = 0.7$ and a chain of 40 atoms is simply not possible. The corresponding contributions will not appear in the spectrum.

2- and 3-dimensional systems

In systems of a higher dimensionality, a new phenomenon appears, which will only appear in completely filled 1-dimensional systems: the problem of site percolation, i.e., the appearance of a continuous chain or cluster of interacting atoms along the whole simulated system.

In a 1-dimensional system, e.g., a magnetic nano wire, with only nearest-neighbor interactions, an interacting cluster ends when a single atom is missing. Thus the percolation threshold, i.e., the occupation ratio needed for a continuous cluster, is $c_\mathrm{p} = 1$. In a 2-dimensional rectangular grid, it is possible to build a
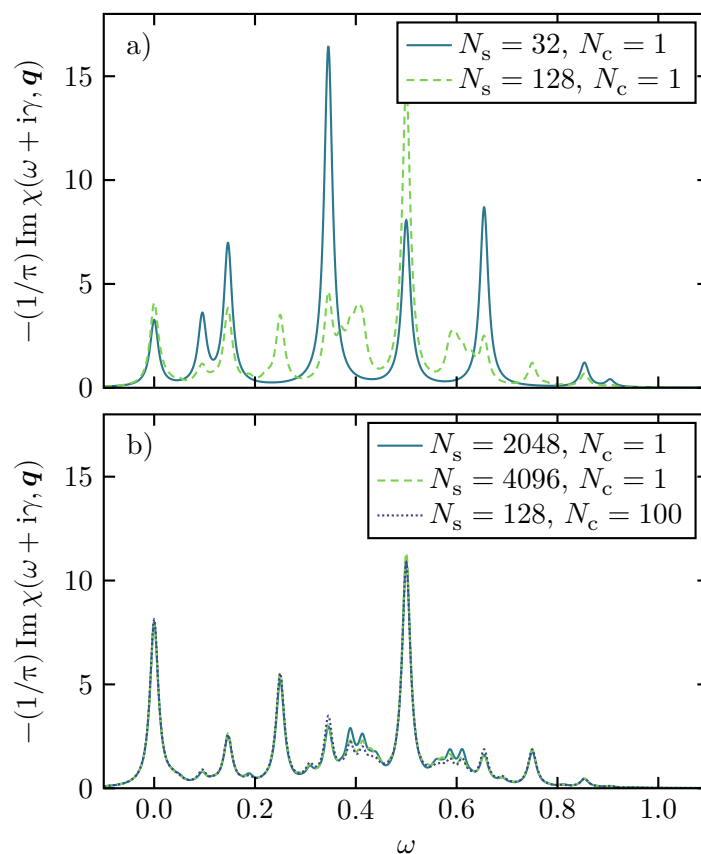
Figure 5.1.2: Spin-wave spectra for one-dimensional random alloys with concentration $c = 0.7$ and wave-number $q = 0.25 \cdot 2\pi/a$. The spectrum in panel (a) with $N_\mathrm{s} = 32$ and $N_\mathrm{c} = 1$ corresponds to the structure in fig. 5.1.1.[T1]

continuous cluster "around" missing atoms, which results in a percolation threshold of around 0.59.[76] Similarly it is even easier on a 3-dimensional simple cubic grid, resulting in a value of around 0.31.[77,78] The usual systems appearing in physics, the face-centered cubic and body-centered cubic systems, have percolation thresholds of 0.20 and 0.25, respectively.[78] For example, Mn-doped GaAs, or Mn- or Co-doped ZnO have the magnetic atoms on their face-centered cubic sublattice.[4]

The impact of percolation can be observed in the spin excitation spectra in fig. 5.1.3. While the spectrum of the 1-dimensional system with $N_s = 128$ sites is made out of single peaks with artificial broadening $\gamma = 10^{-2}$, resulting from standing spin excitations, the spectra of the systems in two and three dimensions with respective number of sites $N_s = 64^2$ and $N_s = 16^3$ feature a continuum of peaks with intrinsic finite width because of the better connectivity of clusters in higher dimensions. The broadening of the peaks can be interpreted as spin excitations with finite lifetime. The sharp peaks in the spectrum of the 2-dimensional system result from isolated islands, which can also appear above the percolation threshold. Due to the lower percolation threshold of the 3-dimensional system, isolated islands are rarer and only a single broad peak appears.

Reducing the concentration of magnetic atoms in a system of higher dimension to a value below the percolation threshold (cf. fig. 5.1.4), results again in localized spin excitations with corresponding sharp peaks. By estimating the intensity of the zero-frequency peak, i.e., the Goldstone mode, it can be shown that the contribution of the localized spin excitations vanishes for increasing concentration of magnetic atoms.[T1]

5.1.2 Magnon CPA

The next step is the comparison of the exact Monte Carlo calculations to the results of the CPA calculations in the magnonic subsystem. Figure 5.1.5 shows the comparison of Monte Carlo, CPA and VCA calculations. While the Monte Carlo calculation features a series of localized spin excitations and corresponding peaks in the spectrum, the CPA yields a continuum of states. This wrong behavior is mainly a result of the mean field character of the CPA, which fails to describe the localized features of the island-like structure.

Careful inspection of the zero-energy peak of the CPA spectrum in fig. 5.1.5 shows a small shift to the region of negative energies. This stems from the poor performance of the CPA in 1-dimensional systems and the difficulty to perform an analytic continuation of this strongly asymmetric peak. The tail towards negative energies, however, will remain in the spectrum even for higher
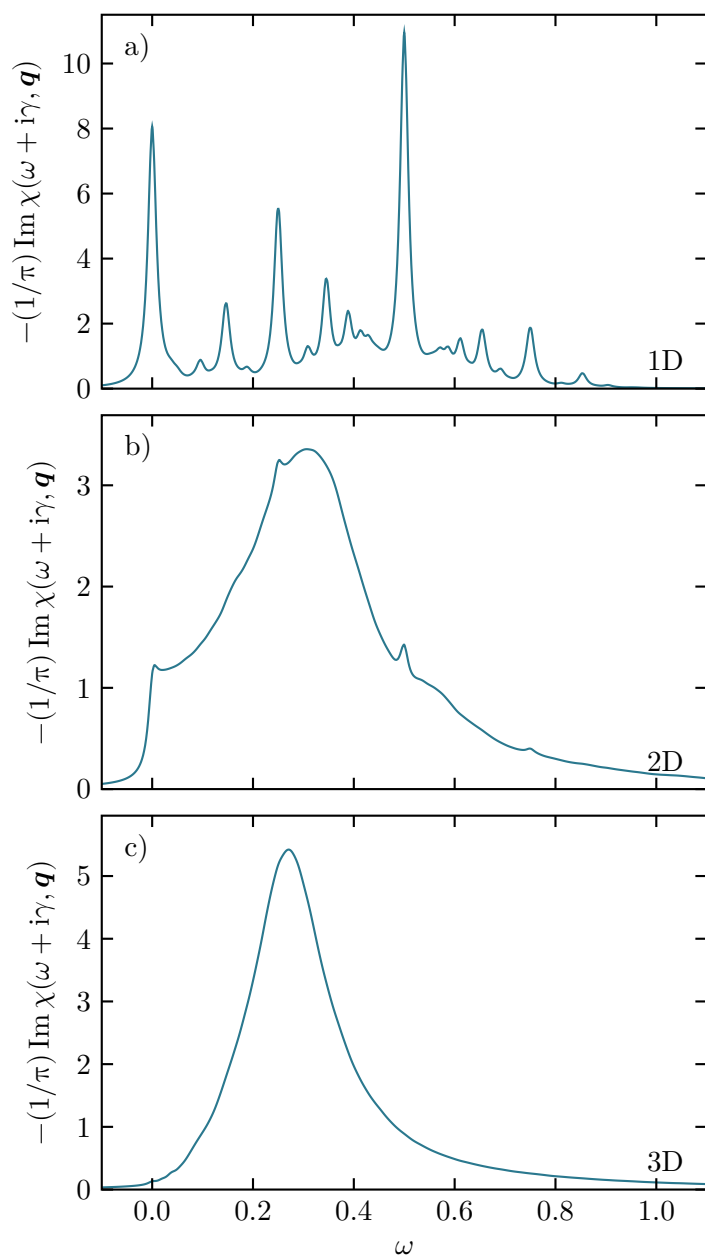
Figure 5.1.3: Spin-wave spectra for random alloys in different dimensions with wave vector $\boldsymbol{q} = (0.25, 0, 0) \cdot 2\pi/a$ and concentration $c = 0.7$. An artificial broadening of $\gamma = 10^{-2}$ was applied.[T1]
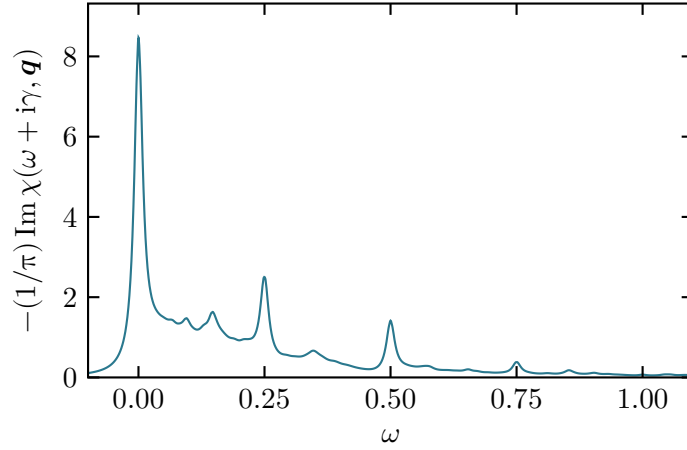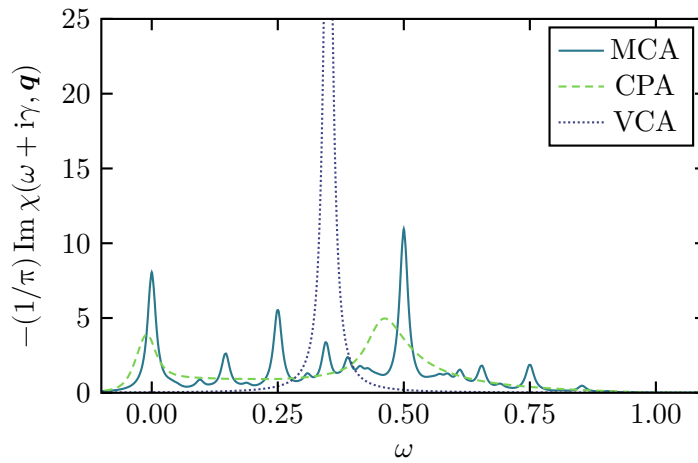
Figure 5.1.4: Spin-wave spectrum for a two-dimensional random alloy with wave vector $\boldsymbol{q} = (0.25, 0, 0) \cdot 2\pi/a$ and concentration $c = 0.4$. An artificial broadening of $\gamma = 10^{-2}$ was applied.[T1]

Figure 5.1.5: Spin-wave spectrum for a one-dimensional random alloy with wave vector $\boldsymbol{q} = (0.25, 0, 0) \cdot 2\pi/a$ and concentration $c = 0.7$. An artificial broadening of $\gamma = 10^{-2}$ was applied.[T1]

dimensions, because it is the result of the artificial broadening γ. The VCA calculation fails completely as it results in a single long living magnon mode because of the static character of its self-energy.

In calculations for higher dimensions (e.g., in fig. 5.1.6), the CPA performs much more satisfactorily. The spectra resemble most of the features of the Monte Carlo calculations. This is the result of the better connectivity and the vanishing influence of localized features of the magnetic system.

5.1.3 Long-wavelength limit

Another interesting investigation can be done with respect to the behavior of the spin-waves in the long-wavelength limit, or in other words, in the center of the Brillouin zone.

In contrast to the results for 1-dimensional systems, the spectra in 2 and 3 dimensions exhibit the interesting behavior that they are showing regular Lorentzian-shaped peaks. These Lorentzians can be characterized by their position ω_q, i.e., the energy of the peak, and their full width at half maximum (FWHM). The calculations show that the peak's energies grow quadratically with respect to the wave vector q. The proportionality parameter D is called the stiffness constant, which depends on the magnetic interaction J, the lattice constant a and the gyromagnetic ratio g as

$$D = gaJ. \tag{5.1.2}$$

For the further considerations, the lattice constant is taken to be $a = 1$, the gyromagnetic ratio is $g = 2$ and the magnetic interaction was previously defined as $J = 1/8$ (cf. section 5.1.1), resulting in a stiffness constant of $D = 1/4$ in all dimensions.

Both the stiffness constant D and the FWHM are dimensionality and concentration dependent (cf. fig. 5.1.7). However, the stiffness constant obtained from the VCA calculation does not depend on the dimensionality and yields a linear dependence on the concentration. Due to the infinite lifetime of the resulting modes, the FWHM is 0 for all concentrations. On the other hand, the stiffness obtained from the CPA calculations shows very good agreement with the Monte Carlo calculations down to the percolation threshold, where the description of the "spin-wave quasiparticle" breaks down. The results for the FWHM are also in good agreement for high concentrations, but show significant deviations for lower concentrations approaching the percolation threshold. This hints a dependence of the damping on the local properties, which are insufficiently described by the CPA method.
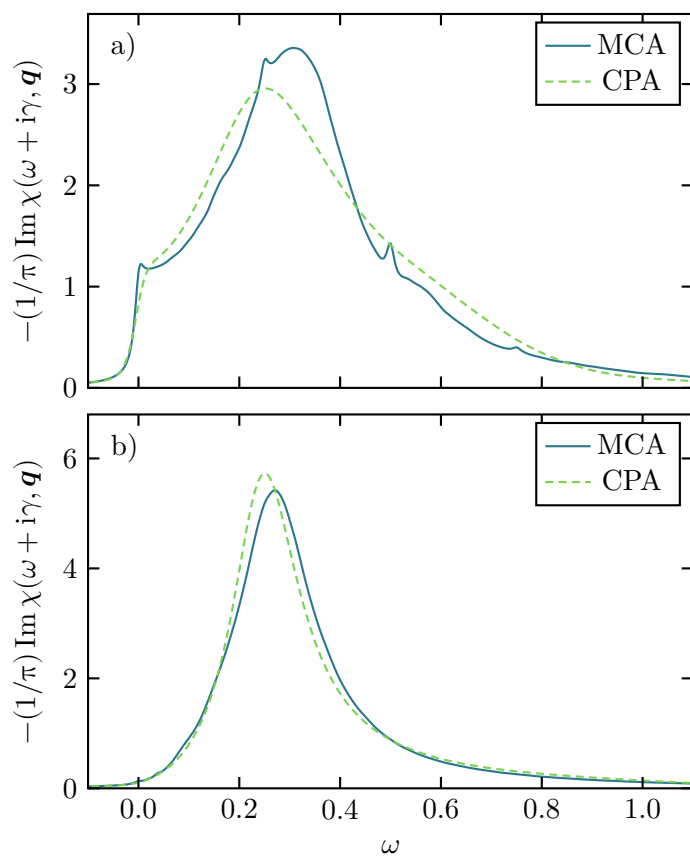
Figure 5.1.6: Spin-wave spectra for two- and three-dimensional random alloys with wave vector $\boldsymbol{q} = (0.25, 0, 0) \cdot 2\pi/a$ and concentration $c = 0.7$. An artificial broadening of $\gamma = 10^{-2}$ was applied.[T1]
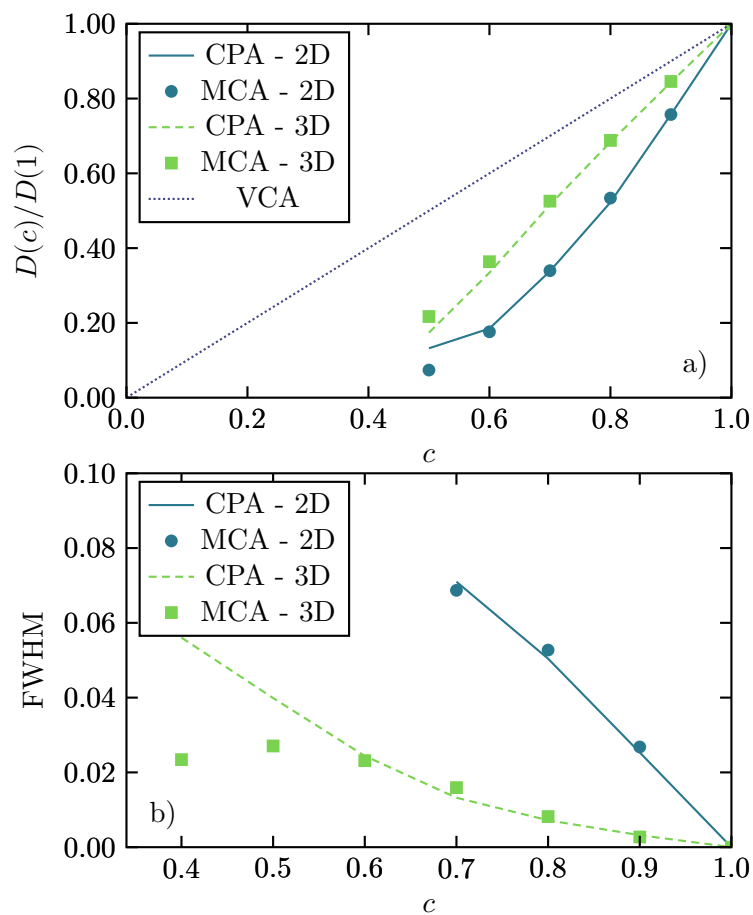
Figure 5.1.7: (a) Normalized spin-wave stiffness D and (b) FWHM for the wave vector $\boldsymbol{q} = (0.125, 0, 0) \cdot 2\pi/a$ in two and three dimensions. An artificial broadening of $\gamma = 10^{-2}$ was applied.[T1]

5.1.4 Impact of electronic structure

In contrast to the model system in the previous section, an actual physical system can have a much longer magnetic interaction range. As a result of this, magnetically isolated clusters are much rarer and, typically, a continuous spectrum can be observed for smaller concentrations of magnetic atoms.

The system considered here is the ultrastrong low-density steels based on $Fe_c Al_{1-c}$, which enjoy a renewed attention.[69] However, nothing is known about the spin dynamics of this alloy consisting of magnetic and non-magnetic atoms. This system is considered for low concentrations of Al at $(1-c) < 0.3$, in a random alloy phase. In this regime, the system features a bcc lattice structure with ferromagnetic ordering[79,80] and a lattice constant, which is linearly increasing with growing Al content.[81]

The electronic structure was calculated in terms of the KKR method based on the local density approximations and the coherent potential approximation, to model the alloying of the system. The resulting magnetic moments range from $2.27\,\mu_B$, for the pure bcc-Fe, up to $2.32\,\mu_B$, for $Fe_{0.9}Al_{0.1}$, and then decreasing down to $2.206\,\mu_B$, for $Fe_{0.7}Al_{0.3}$. The exchange parameters are evaluated using eq. (3.1.29) and taking advantage of the vertex cancellation theorem in the disordered case (cf. fig. 5.1.8).[82,83] It becomes apparent that there are significant contributions to the second-nearest-neighbor interactions, which are strongly varying, but not diminishing, with varying Al content. The 2-dimensional magnetic interactions (see publication [T1]), exhibit a similar behavior with less dependence on the concentration.

The spin excitations of the $Fe_c Al_{1-c}$ system, which were obtained with the Monte Carlo method, exhibit a much more complex behavior in the long-wavelength limit than their counterpart for the theoretical system in the previous section (cf. fig. 5.1.7). Figure 5.1.9 shows both the normalized spin-wave stiffness D and the normalized FWHM for the system in two and three dimensions. Additionally, another calculation (3Dc) was performed, where the magnetic exchange parameters for the perfect Fe system ($c = 1$) were used for all concentrations.

Due to the more complex magnetic interactions including negative exchange parameters in the 3rd and 4th shell, the spin-wave stiffness in the 2-dimensional system decreases with reducing concentration of magnetic atoms slightly faster than the previously studied theoretical model. In three dimensions, an initial increase can be observed, which has its maximum at around $c \approx 0.8$. This change can be explained by the increase of the nearest-neighbor magnetic exchange interaction and the diminishing negative interaction in the more extended shells as can be seen in fig. 5.1.8.
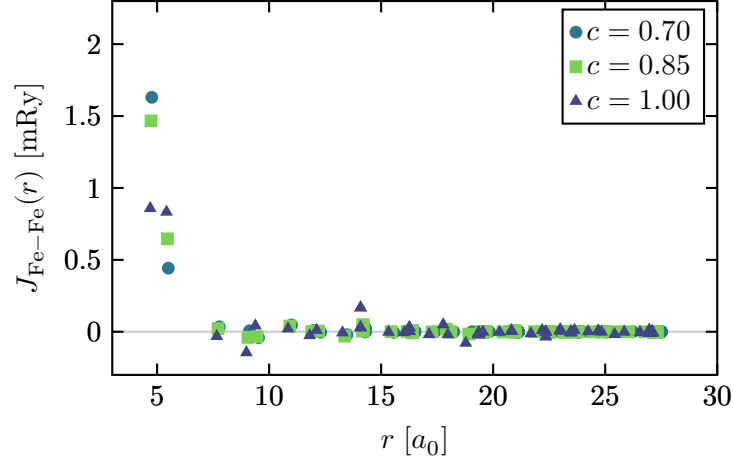
Figure 5.1.8: The exchange parameters between Fe moments in $\mathrm{Fe}_c\mathrm{Al}_{1-c}$ as a function of concentration in three dimensions.[T1]

The results from the calculation with a fixed magnetic exchange interaction (i.e., the influence of the electronic structure is switched off) are similar to the theoretical predictions, which are in principle discarding all interactions beyond the nearest-neighbor interaction. This is the expected behavior, because the influence of the first two shells is similarly affected by the disorder and they are dominating the interaction, compared to the smaller interactions of the farther shells.

The normalized FWHM increases with increasing concentration of Al atoms and the effect is stronger for the 2-dimensional system. The comparison of the two 3-dimensional cases shows that the electronic structure and the corresponding change in magnetic interactions, have a strong influence on the FWHM.

Finally, the CPA calculations are performed for the $\mathrm{Fe}_{0.7}\mathrm{Al}_{0.3}$ system. Figure 5.1.10 shows the good performance of the method, which shows good agreement for the size, position and width of the peaks, especially for longer wavelengths.

Summarizing the investigations, it can be seen that a well-suited method for investigation of magnons in disordered systems was developed. The study of 1-, 2- and 3-dimensional model systems with nearest-neighbor interactions was successfully compared to the respective theoretical predictions. Additionally, a CPA approach for magnons in disordered systems was presented and applied to the alloy $\mathrm{Fe}_{0.7}\mathrm{Al}_{0.3}$ for comparison with the MCA method.
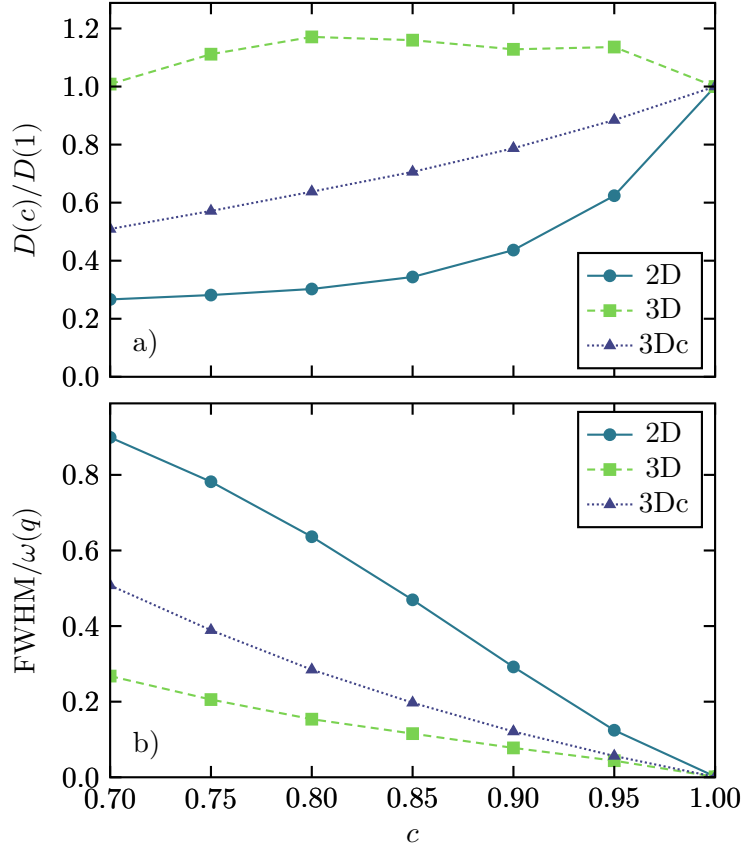
Figure 5.1.9: (a) Normalized spin-wave stiffness D and (b) normalized FWHM for the wave vector $\boldsymbol{q} = (0.125, 0, 0) \cdot 2\pi/a$ for Fe_cAl_{1-c} for two (2D) and three (3D) dimensions and in three dimensions with fixed magnetic exchange parameters (3Dc).[T1]
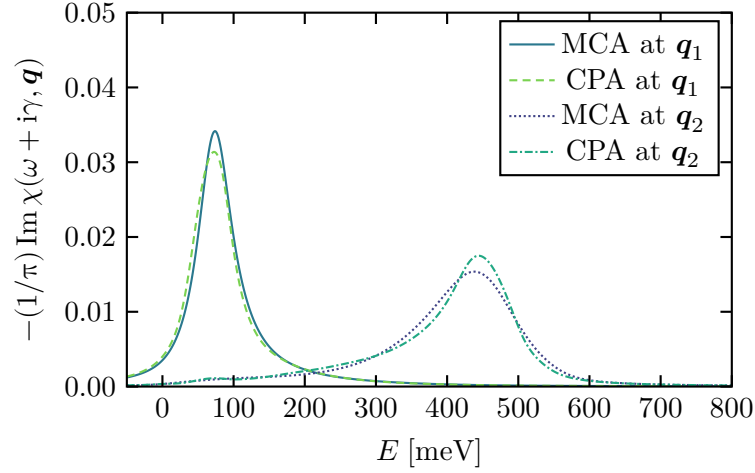
Figure 5.1.10: Comparison of Monte Carlo (MCA) and CPA calculations for the system $Fe_{0.7}Al_{0.3}$ at two different wave vectors $\boldsymbol{q}_1 = (0.125, 0, 0) \cdot 2\pi/a$ and $\boldsymbol{q}_2 = (0.375, 0, 0) \cdot 2\pi/a$. An artificial broadening of $\gamma = 10^{-2}$ was applied.[T1]

5.2 Excitation of plasmons in metallic nanostructures by means of electron beams

The optimization of plasmonic nanostructures is an important topic with regards to the development of optical devices. Therefore, there is a wide range of available methods, which were developed to calculate the optical scattering properties of various structures.

The two major requirements for these methods with respect to the optimization of plasmonic nanostructures are a fast solution of Maxwell's equations and a sufficient flexibility in the systems, which can be calculated. The used Generalized Multiparticle Mie method (cf. section 3.2.3 and publication [T2]) is both fast and flexible. It is possible to calculate multiple scattering of ensembles of particles, whose T-matrix is known. The restriction of the multi-scattering T-matrix (cf. eq. (3.2.24)), i.e., that any source of excitation has to be outside of the smallest circumscribing sphere, is still existent, but only relevant for each individual particle. With respect to the calculation of scattering properties of ensembles of spherical particles with the GMM method, this poses only the restriction that the excitation can't be inside of a scatterer.

5.2.1 Electron energy loss spectroscopy

To verify the correctness of the implemented Generalized Multiparticle Mie method (GMM), the electron energy loss spectra and cathodoluminescence spectra of a dimer of two gold spheres (radius $r = 10\,\text{nm}$ and distance of $1\,\text{nm}$) were compared to the results of the T-matrix method (TMM) and the Discontinuous Galerkin Time Domain method (DGTD).[27,84] The electron passes the dimer with an impact parameter of $b = 10.5\,\text{nm}$, i.e., $0.5\,\text{nm}$ above the surface of one of the gold spheres, and a velocity of $30\,\%$ of the speed of light at the outer edge.

Although the permittivity is the most important property for calculations of plasmonic systems containing all necessary material properties (cf. section 2.2), similar to the importance of the magnetic exchange coefficients J_{ij} in magnonics, the DGTD requires the restriction to an analytic model. The model of choice is the already introduced Drude model for a free electron gas,

$$\varepsilon_{\text{r}}(\omega) = 1 - \frac{\omega_{\text{p}}^2}{\omega(\omega + \mathrm{i}\eta)}, \tag{5.2.1}$$

to get a reasonably fast calculation. The parameters in the Drude model are the plasma frequency ω_{p} and the relaxation rate η. Fitting the Drude model to the experimental data from Johnson and Christy[36] yielded the parameters $\hbar\omega_{\text{p}} = 9.073\,\text{eV}$ and $\hbar\eta = 0.071\,\text{eV}$.[53] These results are similar to previously published parameters.[85–87]

Nevertheless, it is well known that gold can be described much better by adding Lorentzians,[88]

$$\varepsilon(\omega) = \varepsilon_\infty - \frac{\omega_{\text{p},0}^2}{\omega(\omega + \mathrm{i}\eta_0)} + \frac{\omega_{\text{p},1}^2}{\omega_{0,1}^2 - \omega(\omega + \mathrm{i}\eta_1)}, \tag{5.2.2}$$

or critical points describing the interband transitions,[89,90]

$$\varepsilon(\omega) = \varepsilon_\infty - \frac{\omega_{\text{p},0}^2}{\omega(\omega + \mathrm{i}\eta_0)}$$
$$+ \sum_{j=1}^2 C_j \left(\frac{\mathrm{e}^{\mathrm{i}\beta_j}}{(\omega_{0,j} - \omega - \mathrm{i}\eta_j)^{-\mu}} + \frac{\mathrm{e}^{-\mathrm{i}\beta_j}}{(\omega_{0,j} + \omega + \mathrm{i}\eta_j)^{-\mu}} \right). \tag{5.2.3}$$

The performance of these three approaches is compared in fig. 5.2.1.[34] The shown Drude model works well for long wavelengths but fails for wavelengths below $700\,\text{nm}$. However, in contrast to the definition in eq. (5.2.1), the permittivity for
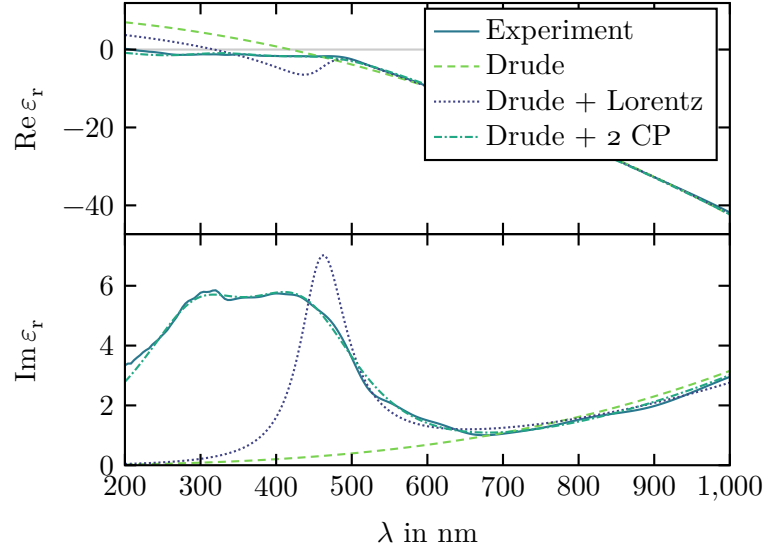
Figure 5.2.1: Permittivity of gold from Johnson and Christy[36] in comparison with the Drude model,[88] the Drude model with Lorentzians[88] and the Drude model with critical points.[34,89,90]

small wavelengths is not fixed to 1 but set to the value $\varepsilon_\infty = 9.0685$ to avoid a systematic misrepresentation of the real part of the permittivity. The description with an added Lorentzian extends the range of well-represented wavelengths down to 500 nm but adds a bump in the real part of the permittivity. The introduction of critical points shows a very good agreement over the whole examined wavelength range. Due to the complexity of the Drude model with added Lorentzians or critical points, these models are not suitable for usage with the DGTD method because of the necessary computation time. The TMM and GMM don't have this restriction and can be used with arbitrary permittivities including the experimental data.

The calculation of scattering in the (sub-)nanometer regime requires careful consideration of non-local effects. These include the difference in permittivity due to finite size effects compared to the used bulk permittivity. A possible implementation could be achieved in terms of the hydrodynamical model as an extension to the present Drude model by adding an additional damping term.[91] The influence on such calculations was already discussed in theory[92] and in comparison of theory and experiment.[93] Ultimately, García de Abajo[92] showed that the typical effects, i.e., blue-shift of the resonances and plasmon broadening,

won't appear in the used regime of spheres of $10\,\mathrm{nm}$ radius and distance of $1\,\mathrm{nm}$, but well below this distance. Concluding, the non-local effects were not taken into account in the following calculations.

The electron energy loss probability $P_{\mathrm{EELS}}(\omega)$ is the probability that an electron passing the scatterer loses $\Delta E = \hbar\omega$ of energy

$$\Delta E = \hbar \int_0^\infty \mathrm{d}\omega\,\omega P(\omega). \tag{5.2.4}$$

The energy loss can be determined by integrating the force on the electron along its path, which appears due to the interaction with the scattered field $\boldsymbol{E}_{\mathrm{sca}}$,

$$\Delta E = e \int_{-\infty}^\infty \mathrm{d}t\,\boldsymbol{v}_{\mathrm{e}}(t) \cdot \boldsymbol{E}_{\mathrm{sca}}(\boldsymbol{r}_{\mathrm{e}}(t), t). \tag{5.2.5}$$

Exploiting the no-recoil approximation, i.e., the electron's momentum is constant, this can be reformulated as an integral in the frequency domain. Comparing the result with eq. (5.2.4) yields an expression for the electron energy loss probability

$$P_{\mathrm{EELS}} = \frac{2e}{\hbar\omega} \int_{-\infty}^\infty \mathrm{d}t\,\mathrm{Re}\Big\{\boldsymbol{v}_{\mathrm{e}}(t) \cdot \boldsymbol{E}_{\mathrm{sca}}(\boldsymbol{r}_{\mathrm{e}}(t), \omega)\mathrm{e}^{-\mathrm{i}\omega t}\Big\}. \tag{5.2.6}$$

By further application of the no-recoil approximation, i.e., by substitution of $\boldsymbol{r}_{\mathrm{e}}(t) = \boldsymbol{r}_0 + \boldsymbol{v}t$, this expression becomes suitable for frequency domain calculations. Additionally, the restriction that the electron only travels in z-direction is set:

$$P_{\mathrm{EELS}} = \frac{2e}{\hbar\omega} \int_{-\infty}^\infty \mathrm{d}z\,\mathrm{Re}\Big\{\boldsymbol{e}_{\mathrm{z}} \cdot \boldsymbol{E}_{\mathrm{sca}}(\boldsymbol{r}_0, \omega)\mathrm{e}^{-\mathrm{i}\omega z/v}\Big\}. \tag{5.2.7}$$

On the other hand, the cathodoluminescence probability is simply given by the amount of scattered energy and can thus be calculated by integrating the Poynting vector over a closed surface around the scatterer:

$$\Delta E = \int_0^\pi \mathrm{d}\theta \int_0^{2\pi} \mathrm{d}\varphi \int_{-\infty}^\infty \mathrm{d}t\,r^2 \boldsymbol{e}_{\mathrm{r}} \cdot (\boldsymbol{E} \times \boldsymbol{H}). \tag{5.2.8}$$

Similar to eq. (5.2.4), this energy loss can be expressed by integrating the cathodoluminescence probability

$$\Delta E = \hbar \int_0^\pi \mathrm{d}\theta \int_0^{2\pi} \mathrm{d}\varphi \int_0^\infty \mathrm{d}\omega\,\omega P_{\mathrm{CL}}(\omega, \theta, \varphi). \tag{5.2.9}$$
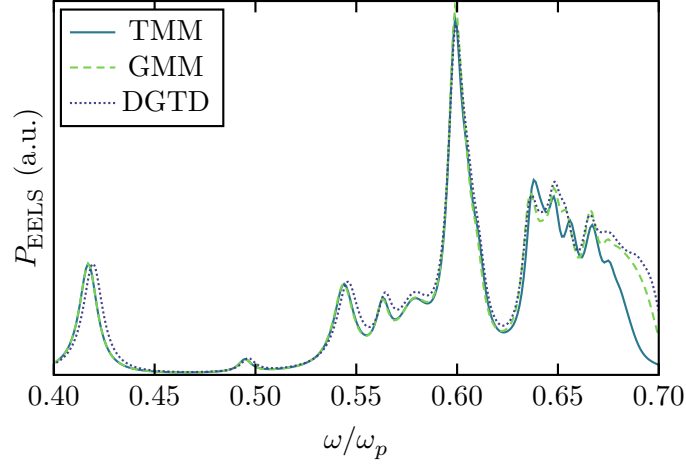
Figure 5.2.2: Comparison of the electron energy loss probability $P_{\mathrm{EELS}}(\omega)$ for a Au dimer, calculated with T-matrix method (TMM), Generalized Multiparticle Mie method (GMM) and Discontinuous Galerkin Time-Domain method (DGTD).[T2]

Comparing this with the Fourier transform of eq. (5.2.8) yields an expression for the angular-dependent cathodoluminescence probability, which can easily be calculated in the far-field limit of the fields:

$$P_{\mathrm{CL}}(\omega, \theta, \varphi) = \frac{1}{\hbar \omega} \sqrt{\frac{\varepsilon_{\mathrm{s}}}{\mu_{\mathrm{s}}}} \left| \boldsymbol{E}(\theta, \varphi) \right|^2. \qquad (5.2.10)$$

The comparison of the three methods (GMM, TMM and DGTD) can be seen in fig. 5.2.2. The spectra of GMM and TMM were calculated with a maximum multipole order of $n = 16$ to get comparable results. This maximum expansion order was limited by the stability of the TMM, while the GMM is more stable[94] and can achieve much higher expansion orders. The curves are normalized to the height of the first peak.

For lower frequencies, the GMM and TMM show a very good agreement, while there are some larger differences for frequencies $\omega \geq 0.65\omega_{\mathrm{p}}$. This could be explained by poorer convergence properties of the TMM. Overall, the TMM uses (in this case) only half the number of expansion coefficients the GMM uses because there is essentially only a single expansion center. The GMM expands the fields in the centers of the two spheres. However, by increasing the multipole order of the TMM, a clear trend towards the GMM's solution can be seen.
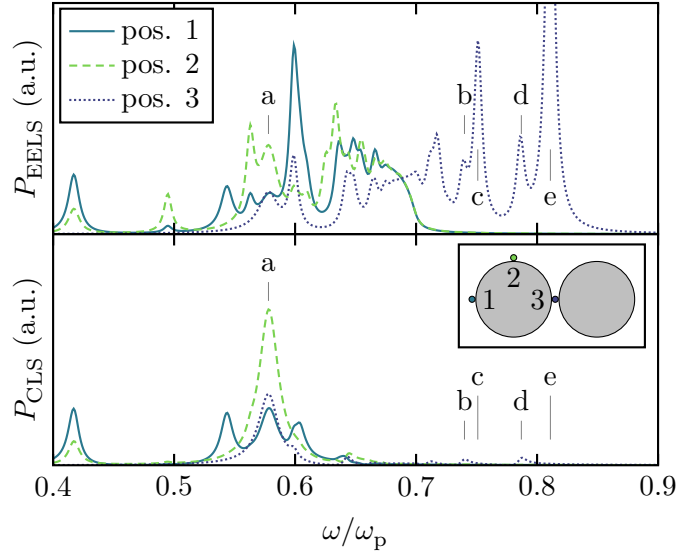
Figure 5.2.3: Electron energy loss probability and cathodoluminescence probability for a Au dimer excited at three different points.[T2]

The results of the DGTD show a slight frequency shift towards higher frequencies and the results at higher frequencies show some minor differences, too. The reason for this could also be missing convergence: A very fine spatial mesh is necessary to describe the interaction of electron and dimer, and a very long simulation in the time-domain is necessary to acquire a reasonable Fourier transform.

As the GMM is more versatile, i.e., it does not pose restrictions on the path of the electron beam, two other trajectories were investigated (cf. fig. 5.2.3). The first path is, again, outside the dimer, the second is at the side of one sphere, and the third path goes through the center of the dimer. The spectra corresponding to paths 1 and 2 show contributions mainly in the lower frequency range, while the spectrum of path 3 has most contributions in the higher frequency range. This is indeed the expected behavior because the excitations at point 1 and 2 excite modes, which "bounce" along the long axis of the dimer. On the other hand, the symmetry requires excitations at point 3 to be symmetrically restricted to a single sphere.

By examining the cathodoluminescence spectrum, which is a far-field quantity, it is possible to examine so called dark and bright modes. Dark modes are modes, which exist locally, but don't couple to the far-field because their contributions cancel out. An example would be the excitation at position 3, when the excited

mode is symmetrically oscillating in the two sphere. On the other hand, an excitation from position 1 could oscillate in both sphere in the same direction, yielding a high contribution to the far-field and, thus, exhibiting a bright mode. In the spectrum in fig. 5.2.3, the modes c and e show no contribution to the cathodoluminescence probability and can be considered to be dark modes, while the modes b and d show some contributions and are thus optical bright modes. The mode a is prominent for all three positions. Its frequency corresponds to the frequency of the dipole mode of a single sphere, which is directed along the electron path.

5.2.2 Plasmonic filter

The usual optimizations, which are found in the literature, are carried out for a near-field enhancement like it is needed for the surface enhanced Raman spectroscopy (SERS).[95,96] However, in this section, another target will be used to optimize plasmonic nanostructures: a plasmonic filter.

A plasmonic filter can be understood as a device, which filters an incoming excitation or signal and lets only pass a certain frequency or frequency range. Thus, the plasmonic filter could be considered as the plasmonic equivalent of bandpass filters in acoustics and electronics. In this case, the excitation is an electron beam with an electron's velocity of $v = 0.3c_0$.

The predefined structure consists of a single fixed sphere next to the reference point and additionally five spheres, which should be positioned by the optimization process in a box given by $x, y \in -30 \dots 30$ nm and $z \in -25 \dots 125$ nm. All spheres have a fixed radius of 10 nm. The goal was the creation of a filter, which enhances the field for the wavelength of $\lambda = 600$ nm, while blocking the field for $\lambda = 500$ nm. That is, the fitness was given by the function

$$F = \log\left(\frac{|\boldsymbol{E}_{600\,\mathrm{nm}}|}{|\boldsymbol{E}_{500\,\mathrm{nm}}|}\right). \tag{5.2.11}$$

Over the course of the coarse optimization with genetic algorithms, several different structures were generated indicating a complicated fitness function. However, at the end, the best results, which were then optimized with the simplex algorithm, consisted of a single sphere "catching" the electron's field and an arc guiding the scattered field towards the reference point (cf. fig. 5.2.4).

A separate optimization with the SP-UCI method (cf. section 4.3) showed similar result. For this method, there are no intermediate, coarse results available, because it already contains a simplex algorithm for fine optimization. The
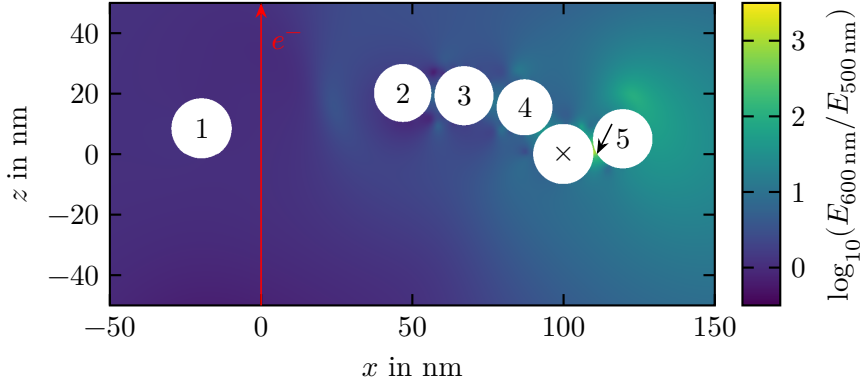
Figure 5.2.4: Contrast between scattered fields for $\lambda = 500\,\text{nm}$ and $\lambda = 600\,\text{nm}$. The black arrow shows the point, where the field is measured to optimize the system. The white areas indicate the spheres. The sphere marked with ($\times$) is fixed.[T2]

Sphere	x in nm	y in nm	z in nm
1	−19.5	−0.4	8.4
2	47.0	−2.9	20.1
3	67.2	−2.1	19.2
4	87.2	−3.8	15.4
fixed sphere ($\times$)	100.0	0.0	0.0
5	119.6	−1.6	5.0

Table 5.2.1: Optimized positions for the plasmonic filter (see fig. 5.2.4).

results obtained from the SP-UCI method were in general better than the results obtained from genetic algorithms and simplex algorithm.

The best result, obtained from the optimization, has all its spheres positioned almost perfectly in the x-z-plane (cf. table 5.2.1). There is indeed a tendency towards a perfectly in-plane structure, but the optimization of tightly packed spheres with the restriction of a minimum distance or no overlap is numerically very expensive.

As a comparison, an additional optimization was performed for the raw near-field enhancement for both wavelengths. The setup for this optimization was the same, but the fitness function was simply the magnitude of the electric field $F = |\boldsymbol{E}|$. The resulting structures, which can be seen in fig. 5.2.5, differ by
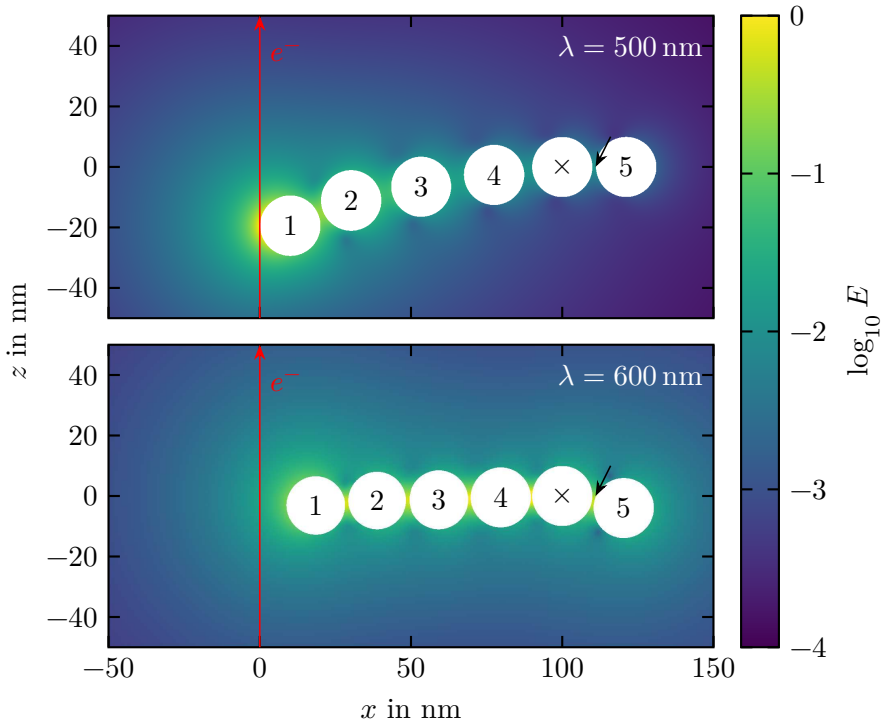
Figure 5.2.5: Optimized structures for both wavelengths. The fields are measured at the points indicated by the black arrows. The spheres marked with ($\times$) are fixed.[T2]

consisting of a stretched structure between the electron beam and the reference point, for $\lambda = 500$ nm (cf. table 5.2.2), and a tightly packed rod of spheres for $\lambda = 600$ nm (cf. table 5.2.3). The field's intensity differs by an order of magnitude between the two wavelengths. Additionally, the numerical complexity of optimizing a tightly packed structure is again apparent from the results. While the stretched structure of the 500 nm optimization has its spheres perfectly in-plane, the tightly packed structure for 600 nm differs several nm from the perfect placement.

At this point, it is important to note, that the results include particle distances down to 0.2 nm and are probably subject of non-local effects. Therefore, further calculations might be necessary.

The Generalized Multiparticle Mie method has proven itself as a fast and reliable tool for the calculation of plasmonic excitations and the optimization

Sphere	x in nm	y in nm	z in nm
1	10.1	0.0	-19.4
2	30.2	0.0	-11.1
3	53.4	0.0	-6.5
4	77.5	0.0	-2.6
fixed sphere ($\times$)	100.0	0.0	0.0
5	121.1	0.0	0.0

Table 5.2.2: Optimized positions for 500 nm (see fig. 5.2.5).

Sphere	x in nm	y in nm	z in nm
1	18.5	2.3	-3.1
2	38.8	2.9	-1.5
3	59.2	1.9	-1.3
4	79.7	0.5	-0.5
fixed sphere ($\times$)	100.0	0.0	0.0
5	120.3	0.3	-4.0

Table 5.2.3: Optimized positions for 600 nm (see fig. 5.2.5).

of metallic nanostructures. It is more versatile than the T-matrix method and faster than the DGTD method.

5.3 Functional materials

In the following section, the investigation of several interesting functional materials is presented, starting with the electromechanical semiconductor ZnO. Afterwards, another semiconductor with strain-dependent electronic properties, $Pb_xSn_{1-x}Te$, is investigated. This section is then concluded with two studies of the electronic and magnetic properties of the Heusler alloys $Ca(Co_xRu_{1-x})O_3$, Pd_2MnSn, Ni_2MnSn and Cu_2MnAl.

5.3.1 Zinc oxide wires – a nanoelectromechanical system

ZnO is a semiconductor with a large band gap of $3.37\,eV$ and is therefore a good target to study the effects of mechanical strain on the electronic properties to optimize the performance in nanoelectromechanical systems.[T3] The large band gap makes ZnO a promising material for light-emitting devices in the range of blue to ultraviolet colors. Additionally, it is a well-established material for strain generators and piezoelectric sensors. However, despite efforts in theoretical and experimental research, the deformation parameters, which describe the relation between the strain and the electronic structure, remain uncertain.

The experimental investigation of strain in ZnO is typically performed by growing a thin film of ZnO on a substrate with smaller or larger lattice constant. The relaxation of the thin film, i.e., the stretching or shrinking with respect to its bulk equilibrium lattice constant, yields typical strains, which are characteristic for the respective substrate. A more flexible approach is the bending of microwires of ZnO, because a continuous range of strains (from compressive to tensile) can be observed along the diameter of the microwire.

The microwire's bending, as seen in fig. 5.3.1, was investigated with the finite element (FEM) simulation package COMSOL Multiphysics.[97] A microwire with a diameter of $8.5\,\mu m$ and a length of $100\,\mu m$ was fixed at its center and a downward pointing force was applied to both ends. Along the diameter (top to bottom) the change of strain from tensile to compressive can be observed. The elastic constants c_{ij}, which were necessary to perform the FEM calculation, were calculated with the Vienna Ab initio Simulation Package (VASP) by employing the algorithm from Fast et al.[98] and Ahuja et al.[99] The gist of this method is the calculation of the total energy for the bulk system under certain distortions of varying degrees. The resulting curves of total energy versus lattice distortion
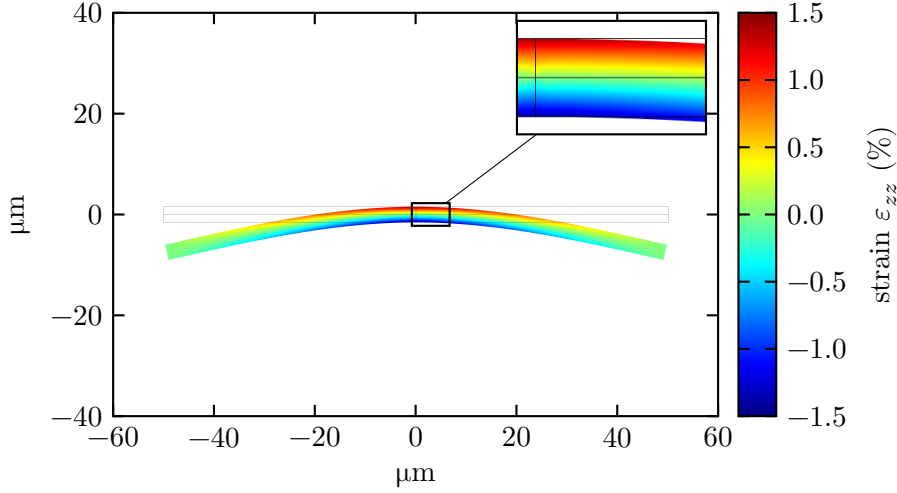
Figure 5.3.1: Simulation of the bending of ZnO microwires with COMSOL Multiphysics.[T3;97]

can be fitted to directly obtain the required elastic constants. The calculations were performed with a Hubbard U of $U_{\text{eff}} = 6.5\,\text{eV}$ on the d orbitals of Zn to get a better agreement with the experimental band gap. The resulting elastic constants are in good agreement with other theoretical and experimental results (cf. table 5.3.1).

To perform further investigations on the band gap, a base point for the further calculations had to be determined. This was achieved by performing total energy calculations for a large number of strains in x- and z-direction to determine the structural ground state of ZnO (cf. fig. 5.3.2).

	Theory		Experiment	
	This work[T3]	Ahuja et al.[99]	Bateman[100]	Kobiakov[101]
c_{11}	2.225	2.30	2.096	2.070
c_{12}	1.181	0.82	1.211	1.177
c_{13}	1.273	0.64	1.051	1.061
c_{33}	2.152	2.47	2.109	2.095
c_{55}	0.510	0.75	0.425	0.448

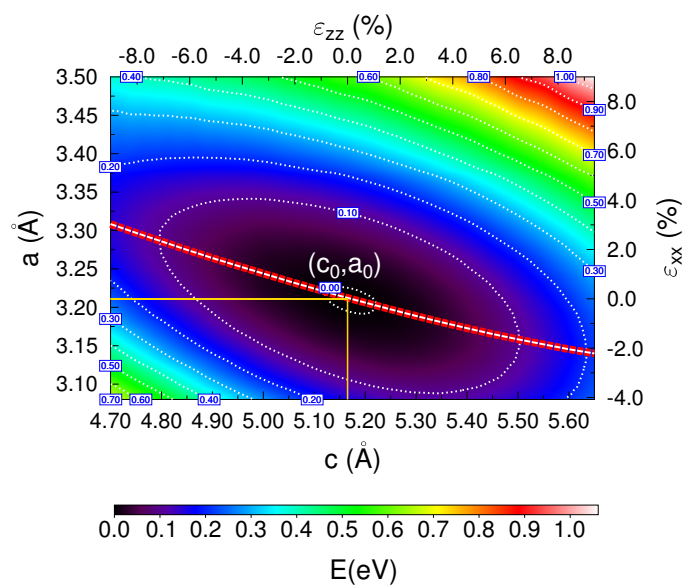Table 5.3.1: Elastic constants c_{ij} obtained from GGA+U ($U_{\text{eff}} = 6.5\,\text{eV}$).

Figure 5.3.2: Determination of the equilibrium lattice parameters c_0 and a_0 of unstrained bulk ZnO as calculated from GGA+U. The red dashed line marks the equilibrium lattice parameters of the strained system. The energy is given relative to the equilibrium energy.[T3]
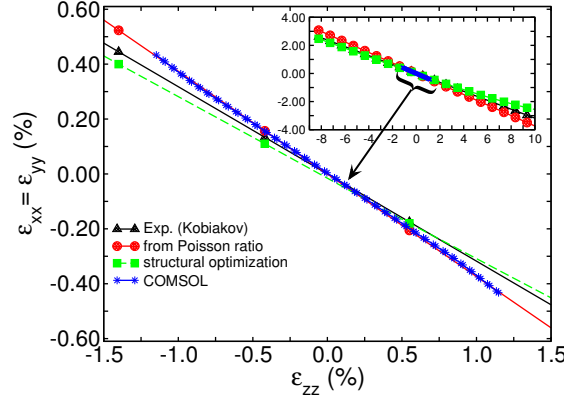
Figure 5.3.3: Comparison of lateral strain ε_{xx} and ε_{zz}.[T3]

Figure 5.3.3 shows the relation of lateral strain ε_{xx} versus ε_{zz} as calculated from the FEM calculation and from the red dashed line in fig. 5.3.2. Additionally, the curve resulting from the Poisson ratio

$$\varepsilon_{xx} = -\nu\varepsilon_{zz}, \qquad\qquad \nu = \frac{c_{13}}{c_{11}+c_{12}}, \qquad\qquad (5.3.1)$$

which was calculated from the elastic constants of Adeagbo et al.[T3] in table 5.3.1, and the curve from the Poisson ratio from the experimental results by Kobiakov[101] are shown. There is a good agreement between all four curves, especially the results from COMSOL fit almost perfectly to the curve from Poisson's ratio of Adeagbo et al.[T3]

The quantity, which was finally obtained, was the deformation potential parameter D. This parameter measures the change of band gap with respect to the uniaxial strain:

$$\Delta E_{\text{gap}} = E_{\text{A/B}} - E_{\text{A/B}}(0), \qquad\qquad (5.3.2)$$

$$E_{\text{A/B}} = E_{\text{A/B}}(0) + D\varepsilon_{zz}. \qquad\qquad (5.3.3)$$

From the latter equation, it is apparent that the deformation potential parameter D can be calculated from the slope of the band gap change ΔE_{gap} with respect to the uniaxial strain ε_{zz}, which can be seen in fig. 5.3.4. The value, resulting from this slope is $D = -2.91\,\text{eV}$, which differs from an experimentally determined value of $D = -2.04(2)\,\text{eV}$.[102] However, one has to keep in mind that there is a large dependence on the used exchange-correlation functional and the respective U_{eff} parameter. Reducing the value of U_{eff} in the GGA+U calculations leads
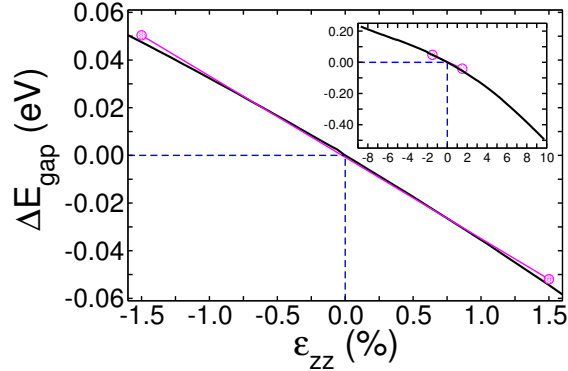
Figure 5.3.4: Change of the band gap ΔE_{gap} with respect to the uniaxial strain ε_{zz} as calculated from GGA+U ($U_{\text{eff}} = 6.5\,\text{eV}$). The pink line approximates the slope around the equilibrium position.[T3]

to a decrease of the deformation potential parameter. By omitting U_{eff}, i.e., by performing a regular GGA calculation, a value of $D = -2.18\,\text{eV}$ can be obtained, but the band gap also reduces to $E_{\text{gap}} \approx 0.75\,\text{eV}$.

The discussion of the used functionals for the calculation of deformation potential parameter D can be further extended: In table 5.3.2 several theoretic calculations are compared to the experimental results for the deformation potential parameter,[102] the position of the d band of Zn[103–105] and the band gap.[106,107] While using LDA or GGA functionals, the theoretical results are systematically too large but still close to the experimental value. The application of Coulomb correlation corrections as in the GGA+U and the HSE screened hybrid-functional approach increase the deviation. Especially, the increase of the parameter U changes the slope of the curve in fig. 5.3.4 and thus the corresponding deformation potential parameter to the worse. Additional treatment of the GGA results with many-body perturbation theory within the GW approximation yields large deviations.

The electronic structure of the system is calculated with full structural relaxation for LDA, GGA and GGA+U functionals. The other functionals were used with the equilibrium lattice constants of the GGA calculation, because the equilibrium structural parameters are differing by only a few percents when using different functionals. Although the meta-GGA calculations can in principle also be performed with full-relaxation, those results were showing a too strong deviation incomparable to the experimental measurements. Using the GGA parameters, the meta-GGA functional yielded the best results, overall. The

Functional	D	$E(\mathrm{Zn_d})$ in eV	E_{gap} in eV
LDA	-2.26	-5.59	0.67
GGA	-2.18	-5.57	0.73
GGA + $(U_{\mathrm{d}} = 1.0\,\mathrm{eV})$	-2.22	-5.77	0.86
GGA + $(U_{\mathrm{d}} = 2.5\,\mathrm{eV})$	-2.39	-6.14	1.03
GGA + $(U_{\mathrm{d}} = 4.0\,\mathrm{eV})$	-2.61	-6.67	1.19
GGA + $(U_{\mathrm{d}} = 6.5\,\mathrm{eV})$	-2.91	-7.41	1.45
meta-GGA	-2.09	-5.60	0.73
HSE $(\alpha = 0.375)$	-2.90	-7.24	3.28
PBE0	-2.81	-6.55	3.09
GGA + $\mathrm{G_0W_0}$	-3.70	-6.35	2.14
GGA + GW	-4.02	-7.05	3.20
Experiment	$-2.04(2)$	$-7.4...-8.6$	3.43

Table 5.3.2: Deformation potential parameter, location of the $\mathrm{Zn_d}$ states and band gap from theoretical calculations compared to experiments. Only the LDA, GGA and GGA+U calculations were performed with full relaxation.

differences in electronic structure of LDA, GGA and meta-GGA are mainly due to the underestimation of the band gap and the overestimation of the hybridization of $\mathrm{Zn_d}$ and $\mathrm{O_p}$ orbitals. Attempting a correction by adding an additional orbital-specific Hubbard correlation (U), both the location of the $\mathrm{Zn_d}$ band and the band gap are systematically improved. However, the optimal choice of the U parameter is open for discussion, because the increase of U results in a systematically increasing deviation of the deformation potential parameter D.

In these calculations, the results from the LDA, GGA and meta-GGA calculations are reliably describing the structural properties. The higher level GGA+U and hybrid functional methods show an improved picture of the electronic structure, but fail to determine accurate values for the deformation potential parameter. The results from the GGA+U calculations imply a change of electronic structure with respect to each strain value. This means that the parametric calculations need a new set of parameters (e.g., a new value of U in GGA+U) for each calculation. However, missing a proper scheme to determine these parameters, one is intended to stick to a fixed set of parameters for all calculations. The big advantage of the basic functionals is their independence from parameters. Additionally, the errors of exchange and correlation cancel out to some degree,

increasing the quality of the final results.[108]

In summary, the variation of the band gap was investigated with density function theory under consideration of several exchange-correlation functionals. The LDA and GGA functionals provide the most reliable results for the deformation potential parameter. The mechanical properties were successfully compared to calculations within the finite-element method implemented by COMSOL Multiphysics. In the future, these studies should be extended to other functional oxide materials to understand their rich properties.

5.3.2 Band gap inversion of $Pb_xSn_{1-x}Te$

The investigation of the effects of hydrostatic pressure on the electronic structure of $Pb_xSn_{1-x}Te^{T4}$ is related to the previous topic. This semiconductor is used in infrared photodetectors and the fabrication of thermoelectric materials. A recent interest developed in the carrier controlled ferromagnetism of the material, while doping. Additionally, it is a topological crystalline insulator with robust conducting states.

The latter property is related to the band gap inversion observed during the alloying process from SnTe to PbTe. During the substitution of Sn atoms with Pb atoms, the band gap closes and reopens. Additionally, the character of upper valence band and the lower conduction band are inversed. This interesting phenomenon can be observed by comparing the anion and cation contributions to the Bloch spectral function A_B for the pure systems PbTe and SnTe at the band gap along the high-symmetry line Γ–L–W, as calculated by the fully relativistic KKR method.[44] Figure 5.3.5 shows the difference between both contributions

$$\Delta A_B = A_B^{cation} - A_B^{anion}. \qquad (5.3.4)$$

While the investigation of PbTe shows the typical behavior of a semiconductor, i.e., the valence band is dominated by anion contributions and the conduction band is dominated by cation contributions, a different behavior can be observed for SnTe: The contributions of anion and cation are exchanged or, in other words, inverted. Therefore, the band gap is called "inverted band gap". Inverted band gaps are described as band gaps with negative energy.

Investigating this feature with group theory,[35] the characterization of the bands exhibits the same behavior. The valence and conduction bands of PbTe show even (L_6^+) and odd (L_6^-) symmetry, respectively, while the bands of SnTe show the exact opposite behavior.

By application of the CPA method, it is possible to investigate the actual process of inversion. In fig. 5.3.6 the dependence of the band gap on the change
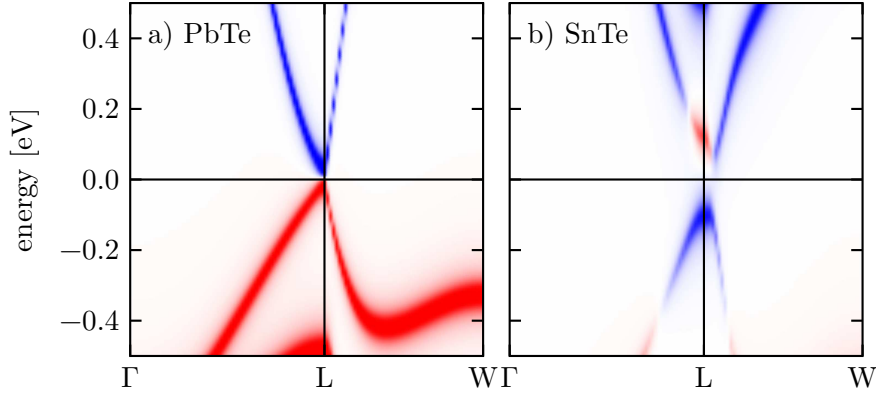
Figure 5.3.5: Difference between the contributions of the cation and the anion to the Bloch spectral function eq. (5.3.4). Larger contributions by the anion (Te) are denoted in red, larger contributions by the cation (Pb or Sn) are denoted in blue.[T4]
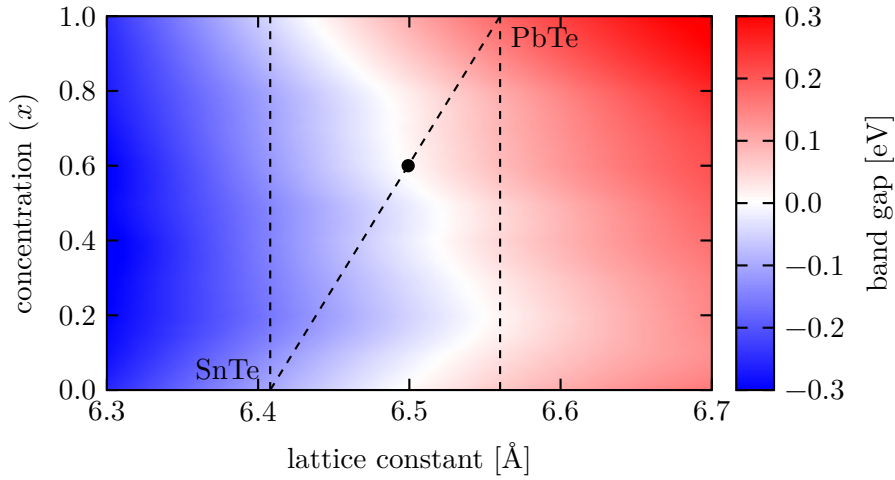

Figure 5.3.6: Band gap of $Pb_xSn_{1-x}Te$ with respect to concentration x and lattice constant. The dashed diagonal line represents Vegard's law. The alloy, for which the band gap vanishes, is marked as black dot.[T4]

of lattice constant and concentration x can be observed. The white area marks the vanishing band gap, which can be observed for all concentration ranges by changing the lattice constant of the system. Along the experimentally accessible Vegard's law,

$$l(x) = x\, l_{\mathrm{PbTe}} + (1-x)\, l_{\mathrm{SnTe}}, \tag{5.3.5}$$

which is shown as dashed line, the three possible states (regular band gap, no band gap and inverted band gap) can be observed. A black dot marks the point on Vegard's law, where the band gap vanishes. The determined value of $x \approx 60\,\%$ is in good agreement with experimental values.[109–111]

This behavior can be explained by referring to the tight-binding model,[112] where an analytical expression for the band gap

$$E_{\mathrm{gap}} \approx \Delta_0 + 10 t_{\mathrm{sp}}^2 (\Delta_1^{-1} - \Delta_2^{-1})/3 \tag{5.3.6}$$

with abbreviations

$$\Delta_0 = \bar{\epsilon}_{\mathrm{p,Pb/Sn}} - \bar{\epsilon}_{\mathrm{p,Te}}, \tag{5.3.7}$$

$$\Delta_1^{-1} = \bar{\epsilon}_{\mathrm{p,Pb/Sn}} - \epsilon_{\mathrm{s,Te}}, \tag{5.3.8}$$

$$\Delta_2^{-1} = \bar{\epsilon}_{\mathrm{p,Te}} - \epsilon_{\mathrm{s,Pb/Sn}} \tag{5.3.9}$$

can be derived. The abbreviations Δ_i depend on the relativistic and non-relativistic orbital energies, $\bar{\epsilon}_{l,\mathrm{X}}$ and $\epsilon_{l,\mathrm{X}}$, respectively, which are related by $\bar{\epsilon}_{l,\mathrm{X}} = \epsilon_{l,\mathrm{X}} \pm 2\lambda_{\mathrm{X}}$. The coefficient λ_{X} is the spin-orbit coupling strength of element X. Equation (5.3.6) yields two effects competing over the size of the band gap: On the one hand, the dependence of Δ_0 and the effective hopping interaction t_{sp} on the volume of the unit cell, and on the other hand, the dependence of the strength of the spin-orbit interaction λ_{X} on the concentration x. Barone et al.[112] suggest that the first criterion is dominating the band gap, which is in agreement with fig. 5.3.6.

In conclusion, the relation between the band gap, the lattice constant, and the concentration x of $\mathrm{Pb}_x\mathrm{Sn}_{1-x}\mathrm{Te}$ was investigated. The experimental findings of a closing band gap at around $x \approx 60\,\%$ could be reproduced. As a consequence, the investigated material is a promising candidate for the fabrication of topological switches.
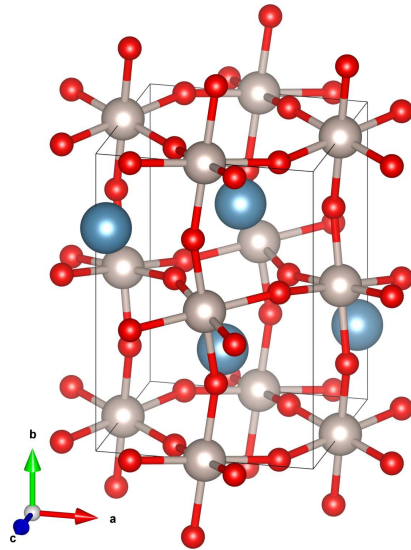
Figure 5.3.7: Structure of the orthorhombic CaRuO$_3$. This structure is also valid for small substitutions of Ru with Co.[T5]

5.3.3 Ca(Co$_x$Ru$_{1-x}$)O$_3$ – a model system for a quantum spin liquid

The Heusler system Ca(Co$_x$Ru$_{1-x}$)O$_3$ (cf. fig. 5.3.7 for the structure of CaRuO$_3$) for small concentrations of Co is a good candidate for an artificial spin-½ system, where magnetic frustrations can be investigated.[T5] This is of particular interest, because it allows to study quantum spin liquids (valence bond liquids), which were originally proposed for 2-dimensional triangular lattices, where an anti-ferromagnetic interaction results in unstable configurations.

The case of the 2-dimensional frustrated triangular lattice can be explained very easily: While a ferromagnetic interaction would result in a parallel orientation of all magnetic moments, it is more difficult to describe the same system with anti-ferromagnetic interaction. A dimer with anti-ferromagnetic interaction has its magnetic moments in anti-parallel orientation. Adding a third atom to the system results in the problem that the interactions with the atoms of the dimer effectively cancel out, allowing the spin to fluctuate.

At this point, the Ca(Co$_x$Ru$_{1-x}$)O$_3$ was proposed as a possible research subject in three dimensions, where non-magnetic Ru atoms were substituted by magnetic Co atoms. Theoretical calculations with the CPA-KKR method show magnetic moments of $1.04 \ldots 1.15 \, \mu_{\mathrm{B}}$, almost linearly increasing over the concentration
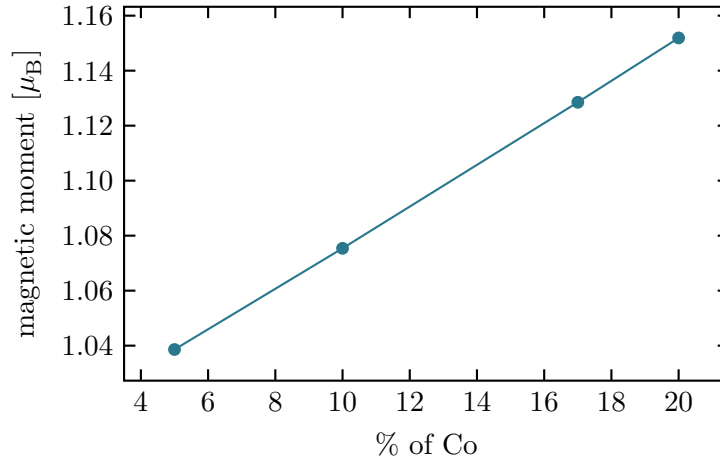
Figure 5.3.8: Magnetic moment of Co in $Ca(Co_xRu_{1-x})O_3$ in dependence of substitution concentration x as calculated with the CPA-KKR method.[T5]

range from $x = 5\%$ up to $x = 20\%$ (cf. fig. 5.3.8). This magnetic moment of approximately $1\,\mu_B$ matches a spin-½ system. The magnetic exchange between nearest-neighbor Co atoms was determined to be $-6.86\ldots-5.98\,meV$, which is in agreement with the experimentally determined interaction of $-5.6\,meV$. The next interactions are rapidly decreasing.

For a chemical substitution in the range of $x = 8.25\ldots17\%$, at least one Ru atom per unit cell is replaced by a Co atom. As a result, different magnetic dimers, that involve nearest-neighbor and farther interactions, form. Due to the anti-ferromagnetic nearest-neighbor interaction, the respective dimers have a net magnetic moment of $m \approx 0$ and show a paramagnetic behavior. It was found that the dimer-dimer interaction exhibits magnetic properties similar to those of 2-dimensional frustrated spin-½ lattices. For example, neither elastic neutron scattering measurements nor heat capacity measurements with and without applied magnetic field could detect any form of magnetic order.

However, temperature-dependent inelastic neutron scattering experiments with $Ca(Co_{0.17}Ru_{0.83})O_3$ showed two interesting features: For low temperatures, starting from $T = 80\,mK$ to $T = 30\,K$, a strong localized excitation at $Q = 1\,\text{Å}^{-1}$ and a weaker one at $Q = 2\,\text{Å}^{-1}$ could be detected with an energy of $E \approx 5.9\,meV$, which is close to the nearest-neighbor interaction between the Co atoms (cf. fig. 5.3.9a-c). The intensity spectrum of the wave vector $Q = 1\,\text{Å}^{-1}$ is well
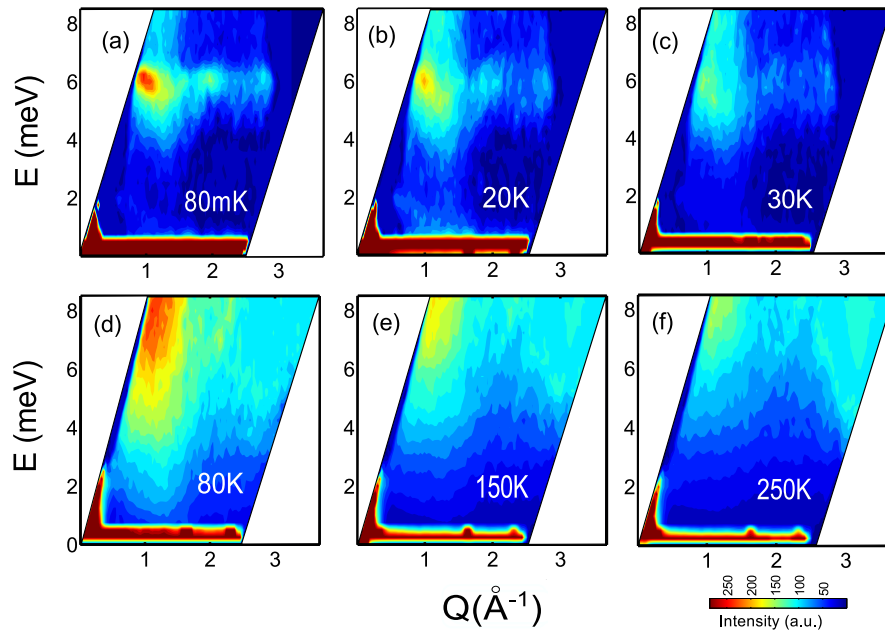
Figure 5.3.9: Spectrum of $Ca(Co_{0.17}Ru_{0.83})O_3$ from inelastic neutron scattering at different temperatures. The plots are background corrected and thermally balanced by multiplying with the Bose factor.[T5]

described by the singlet-to-triplet excitations of spin dimers, involving nearest and next-nearest-neighbor interactions:

$$I(Q) = |F(Q)|^2 \sum_i m_i^2 \left(1 - \frac{\sin(Qd_i)}{Qd_i}\right). \tag{5.3.10}$$

The magnetic moments per formula unit, $m_1^2 = 0.33\,\mu_B^2$ and $m_2^2 = 0.18\,\mu_B^2$, which are obtained from fitting to the experimental spectrum, are consistent with similar previous observations.[T5] The distances $d_1 = 3.18\,\text{Å}$ and $d_2 = 7.88\,\text{Å}$ are close to the lattice values. For higher temperatures starting at around $T = 80\,\text{K}$, a broad continuous excitation appears for the wave vector $Q = 1\,\text{Å}^{-1}$ at $E \approx 7.8\,\text{meV}$ (cf. fig. 5.3.9d-f). This is most likely the result of the breaking of the dimer pairs.

The measurements allow to take three conclusions: Although the disorder in the system would prohibit the valence bond liquid state, the creation of dimers allows the moments to point in random directions. The dimer-dimer interaction results in a gapped singlet-to-triplet excitation. The breaking of the dimer pairs at higher temperatures create freely fluctuating spins that occupy a large part of the energy-momentum space. This quasi-continuum spectrum extends to an unusually high temperature, which extends the study to the semi-classical regime. And finally, the introduction of disorder in a non-frustrated lattice can provide a new platform for further research on quantum magnetism.

5.3.4 Magnetic properties of Heusler alloys

Besides the specialized application of a Heusler alloy in the previous section, the Heusler alloys, in general, have a variety of possible applications including spintronics[113] and magnonics.[2,114] Also a possible application in the fabrication of hard magnets was proposed.[115] Unfortunately, since their discovery more than 100 years ago no full theoretical understanding of their magnetic properties could be achieved.

To obtain this understanding a good agreement between theoretical and experimental results is necessary. Appropriate quantities are spin-wave spectra and Curie temperatures, which, on the one hand, can be measured directly and, on the other hand, can be easily deduced from first principle calculations. Additionally, the magnetic exchange parameters J_{ij} can be used for comparison. However, they are usually not measured directly but obtained by fitting a Heisenberg Hamiltonian to a spin-wave dispersion. As such, they are subject to an assumed model including a certain magnetic interaction range and a predefined kind of anisotropy contributions.

Compound	X	Y	Z	Total
Pd$_2$MnSn, exp.	–	–	–	4.23[118]
Pd$_2$MnSn, theo.	0.07	4.13	−0.07	4.20
Ni$_2$MnSn, exp.	–	–	–	4.05;[118] 3.98[119]
Ni$_2$MnSn, theo.	0.21	3.75	−0.06	4.10
Cu$_2$MnAl, exp.	–	–	–	3.8;[118] 3.60[120]
Cu$_2$MnAl, theo.	0.02	3.62	−0.11	3.56

Table 5.3.3: Magnetic moments of Pd$_2$MnSn, Ni$_2$MnSn and Cu$_2$MnAl from experiment and theory.[T6]

In this work,[T6] these properties are compared for the three Heusler alloys Pd$_2$MnSn, Ni$_2$MnSn and Cu$_2$MnAl. All three of them belong to the group of full Heusler alloys with the general formula X$_2$YZ and crystallize in the cubic L2$_1$ structure, i.e., a NaCl lattice of Y and Z interleaved with a simple cubic lattice of species X. It is shown that the description of magnetic properties can be improved by introducing certain kinds of disorder like the intermixing of atoms between selected sites of the system.

The systems were calculated using the KKR method with the GGA in the PBE parametrization and the full-charge-density approximation. Test calculations with the LDA confirm the results. The magnetic exchange parameters J_{ij} are again determined using the magnetic force theorem and subsequently used to obtain approximates for the critical temperature T_C within the mean field approximation (MFA) as the largest eigenvalue of the matrix $\boldsymbol{\Theta} = \{\Theta_{AB}\}$,

$$\Theta_{AB} = \frac{2}{3k_B} J_{AB}(\mathbf{0}), \qquad (5.3.11)$$

and within Monte Carlo (MC) simulations. The latter were simulated towards a thermal equilibrium state and afterwards properties like the magnetic susceptibility were measured.

The electronic properties were initially investigated for the perfect ordered structures. Strong hybridization can be found between the Mn$_d$ and X$_d$ bands and also with the Sn$_s$ bands in the X$_2$MnSn Heusler alloys (cf. fig. 5.3.10). This supports the picture of d-d and d-s interactions as exchange mechanism in Heusler alloys. These findings are in agreement with experimental results.[116,117] The magnetic moments, shown in table 5.3.3, are also close to the experimental findings. The magnetic properties are calculated with the magnetic exchange
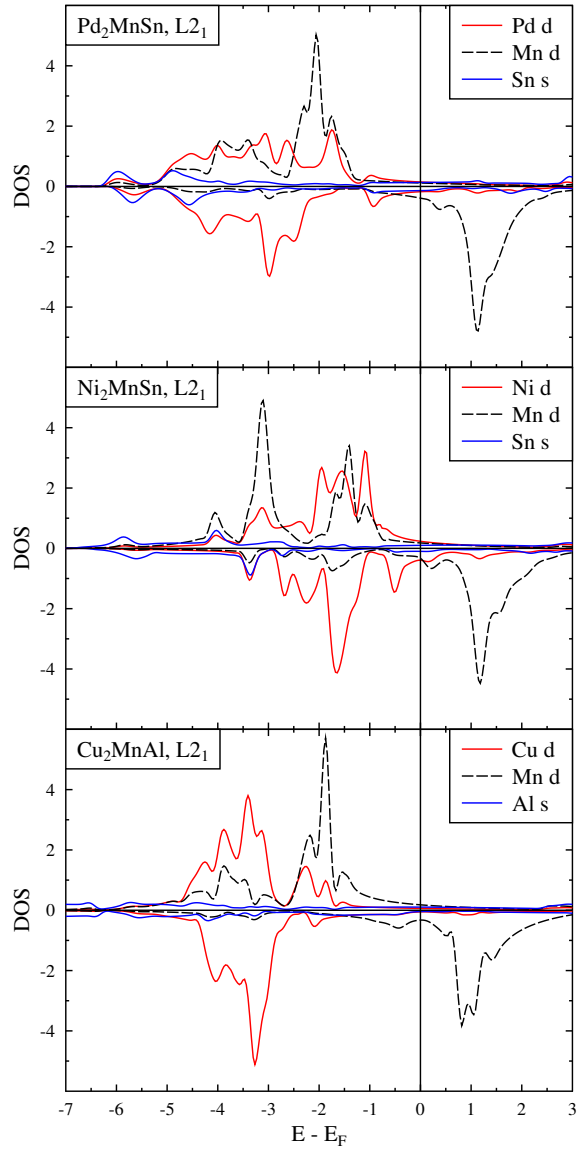
Figure 5.3.10: Partial density of states (DOS) for selected orbitals of the three Heusler alloys Pd_2MnSn, Ni_2MnSn and Cu_2MnAl.[T6]
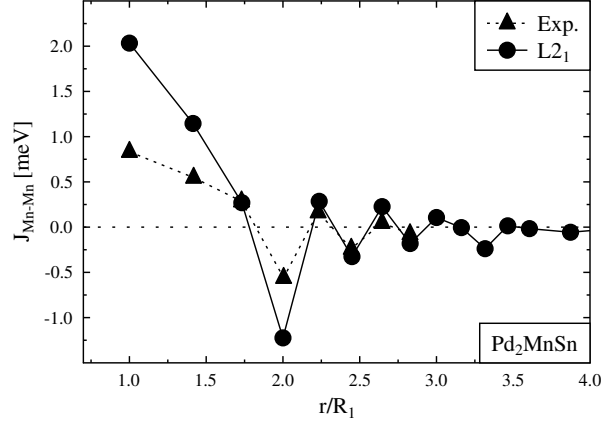
Figure 5.3.11: Magnetic exchange parameters of Pd_2MnSn from experiment[121] and theory.[T6]

parameters J_{ij}, obtained from the successful calculations of the electronic subsystem. Due to the good agreement in the electronic properties, one would also expect a reasonable description of the magnetic subsystem. However, this is not the case and further influences to the magnetic properties have to be considered.

Pd_2MnSn

The obtained magnetic exchange parameters J_{ij} are in good agreement with the experimental ones.[121] Only the parameters of the 1st, 2nd and 4th shell are deviating quantitatively, as can be seen in fig. 5.3.11. One might expect that these contributions cancel out in the resulting dispersion relation (fig. 5.3.12) but the magnon energies are heavily overestimated.

The first approach to improving the spectrum was the correction of the Mn_{3d} bands by application of the GGA+U method ($U = 1.5\,\mathrm{eV}$) as suggested by XPS measurements.[116] This improves the agreement of the calculated dispersion relation with the experimental results. Only along the high-symmetry line Γ–L, an additional dip was introduced. However, the moderate value of $U = 1.5\,\mathrm{eV}$ suggests a minor role for the correlation-related errors. This is strengthened by the good agreement of the magnetic moment of Mn from the GGA calculation ($4.13\,\mu_B$) with the experimentally determined moment ($4.08\,\mu_B$),[122] whereas the GGA+U calculation provides an overestimated result of $4.37\,\mu_B$.
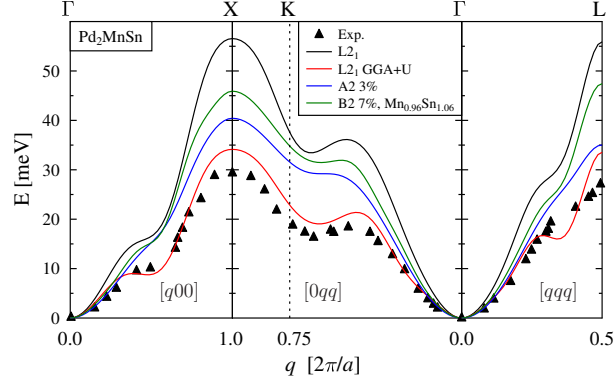
Figure 5.3.12: Dispersion relation of Pd_2MnSn including experimental data from Noda and Ishikawa[121] and theoretical results for the perfect $L2_1$ structure and structures with A2- and B2-like disorder.[T6]

The second approach is the consideration of disorder in the calculation of the dispersion relation. Experimentally, there are two main types of disorder, which can usually appear in full Heusler alloys: Assuming the X_2YZ composition, a B2-like disorder is achieved by exchanging some atoms of species Y and Z, and an A2-like disorder is introduced by exchanging atoms of all three species. In the case of Pd_2MnSn, the B2-like disorder is the most probable and was calculated with an exchange rate of 7 %. The resulting dispersion relation is quantitatively improved but the minimum along the high-symmetry line K–Γ has almost vanished. Introducing the A2-like disorder by exchanging 3 % of Pd with both Mn and Sn, the results improve further. However, the dispersion relation lacks the qualitative description of the turning points along the high-symmetry lines Γ–X and Γ–L and the minimum along K–Γ.

Concerning the critical temperature of the system, table 5.3.4 summarizes the experimental and theoretical results. The original calculation with the $L2_1$ structure overestimates the critical temperature, even beyond the expected overestimation of the MFA calculation. The application of the GGA+U correction yields a massive underestimation, although this method provided the best description of the dispersion relation. A better agreement was achieved by introduction of disorder, which results in a slight overestimation of the critical temperature by the MFA calculations and a moderate underestimation by the MC calculations. The results of the A2-like disorder could be further improved by increasing the amount of exchange to 5 %.

Method	MFA	MC
Exp.	190;[123] 189;[118]	184[122]
L2$_1$	267	224
GGA+U, Mn$_{0.96}$Sn$_{1.04}$	156	110
A2 3 %	219	156
A2 5 %	204	136
B2 7 %, Mn$_{0.96}$Sn$_{1.04}$	197	140

Table 5.3.4: Critical temperatures of Pd$_2$MnSn.

In summary, the GGA+U calculation provided the best dispersion relation but overestimated the magnetic moment and underestimated the critical temperature. However, the overall results are better from pure GGA calculations in combination with A2- and B2-like disorder.

Ni$_2$MnSn

The theoretical treatment of Ni$_2$MnSn is similar to Pd$_2$MnSn. Again, the magnetic exchange parameters are in good qualitative agreement, while the 1st, 2nd and 4th shell provide a quantitative deviation (cf. fig. 5.3.13). In addition to the magnetic exchange between the Mn atoms, a strong nearest-neighbor interaction between Mn and the slightly magnetic Ni atoms (0.21 μ_B) can be observed.

As expected from the previous results, the dispersion relation of the pure L2$_1$ structure, as shown in fig. 5.3.14, is massively overestimating the experimentally determined magnon energies. The introduction of the GGA+U correction with $U = 3$ eV provides a modest quantitative improvement with a qualitative degradation of the spectrum. Similarly, the introduction of A2- and B2-like disorder improves the spectrum slightly.

However, the comparison of the resulting critical temperatures provides a different situation: Table 5.3.5 shows a good agreement for the GGA calculation of the L2$_1$ structure with the experimental results but all other calculations underestimate the critical temperature. Therefore, the chosen methods do not provide a proper theoretical description of the system and the discrepancy between theoretical and experimental results cannot be explained by pure stoichiometric disorder.

Another possible approach is the introduction of n-doping to the system. In this calculation, this was achieved by the insertion of vacancies on the Sn sites.
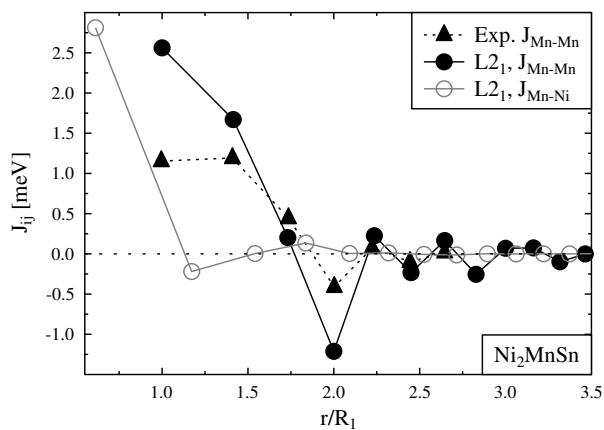
Figure 5.3.13: Magnetic exchange parameters of Ni_2MnSn from experiment[121] and theory.[T6]
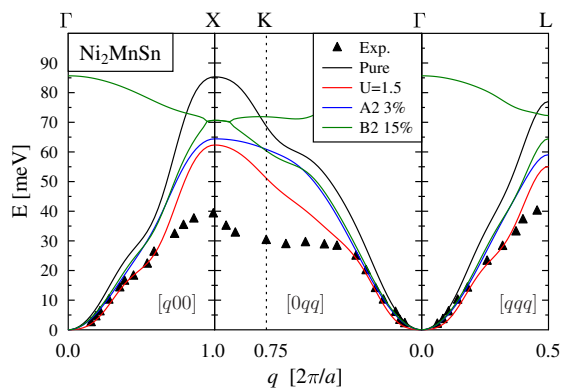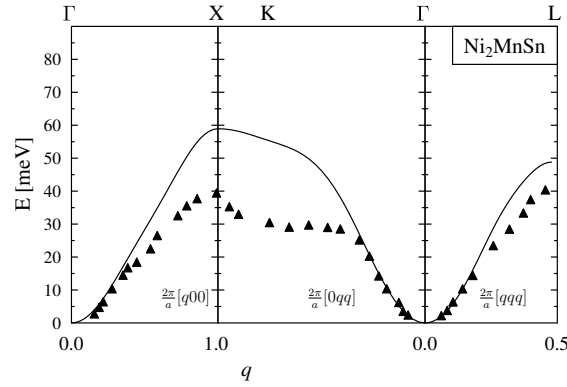

Figure 5.3.14: Dispersion relation of Ni_2MnSn including experimental data from Noda and Ishikawa[121] and theoretical results for the perfect $L2_1$ structure and structures with A2- and B2-like disorder.[T6]

Method	MFA	MC
Exp.	344;[118]	340[124]
L2$_1$	386	285
L2$_1$, GGA+U	319	210
A2 3 %	327	230
B2 10 %	266	220
B2 15 %	236	205

Table 5.3.5: Critical temperatures of Ni$_2$MnSn.

Figure 5.3.15: Dispersion relation of Ni$_2$MnSn including experimental data from Noda and Ishikawa[121] and theoretical results by n-doping.[T6]

The resulting dispersion relation (cf. fig. 5.3.15) shows similar magnon energies as the GGA+U calculation, but improves the qualitative description of the saddle point along the high-symmetry line Γ–K. Additionally, a very good agreement with the long-wavelength behavior is provided by this method.

Cu$_2$MnAl

Finally, Cu$_2$MnAl is the system most difficult to describe of the three Heusler alloys under consideration: While the magnetic exchange parameters (cf. fig. 5.3.16) of the first two shells are only differing by their magnitude and overestimate the experimental parameters by a factor of 3, the exchange parameters of the 3rd and the 4th shell are also of opposite sign. This behaviour, differing from the previous results for Pd$_2$MnSn and Ni$_2$MnSn, can be explained by the high
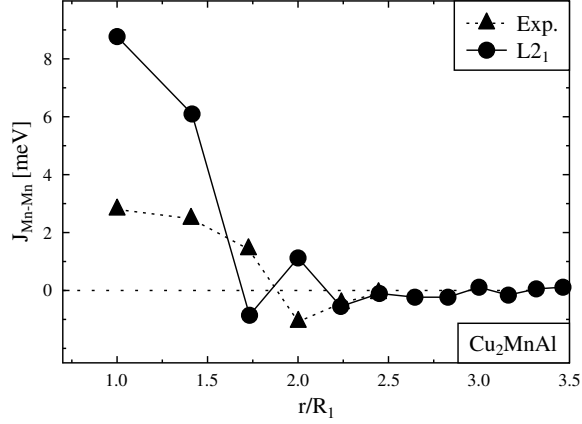
Figure 5.3.16: Magnetic exchange parameters of Cu_2MnAl from experiment[125] and theory.[T6]

dependence of the magnetic exchange on the Z atom.[126] The additional valence electron of Al changes the electron configuration at the Fermi level, which has a large impact on the magnetic exchange parameters.[127]

As expected from the different J_3 and J_4, which are mainly responsible for the dispersion relation along the high-symmetry line Γ–X, the dispersion relation in fig. 5.3.17 shows a clear misrepresentation for the respective wave vector range. The application of the GGA+U method did not result in any qualitative improvement but increased the magnetic moment of Mn to values disagreeing with experimental findings. The corresponding spectrum is therefore not shown. Likewise, the introduction of 5 % of A2-like disorder did not result in a significant change of the spectrum. Introducing a rather large amount of 25 % of B2-like disorder, however, reduces the deviation of the peak along the high-symmetry line Γ–X to half of the original deviation from the perfect $L2_1$ structure. The additional branch, visible in fig. 5.3.17, can also qualitatively describe the extra data points from the experiment.[125] This branch is the result of a second magnetic sublattice of Mn due to the high amount of introduced disorder.

Comparing the critical temperatures of the aforementioned calculations (cf. table 5.3.6), a similar situation appears: While the temperatures calculated from the perfect structure are too high, the GGA+U calculation, which was previously neglected, shows a better agreement by bracketing the experimental values with

Figure 5.3.17: Dispersion relation of Cu_2MnAl including experimental data from Tajima et al.[125] and theoretical results for the perfect $L2_1$ structure, structures with A2- and B2-like disorder and structures with vacancies.[T6]

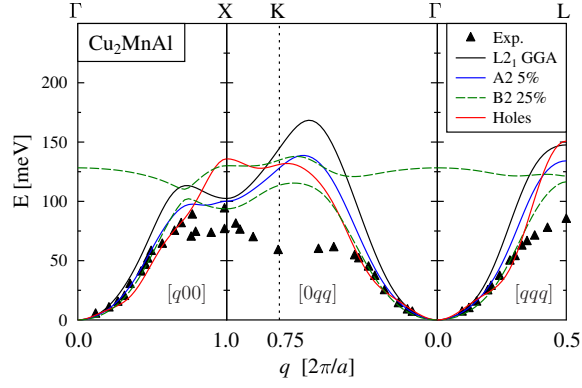| Method	MFA	MC
Exp.	600[118]	
$L2_1$	877	670
$L2_1$, GGA+U	734	470
A2 3 %	750	500
A2 5 %	674	410
B2 10 %	732	510
B2 15 %	645	430

Table 5.3.6: Critical temperatures of Cu_2MnAl.
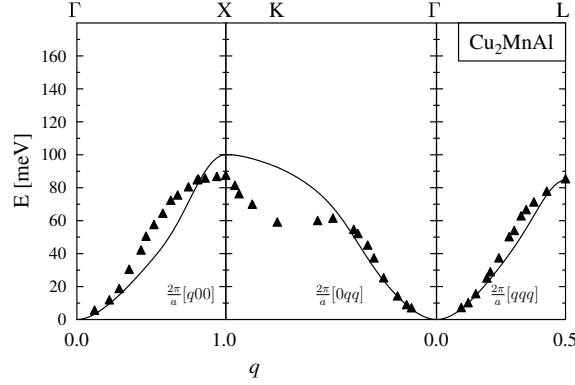
Figure 5.3.18: Dispersion relation of Cu_3Mn_2Al including experimental data from Tajima et al.[125] and theoretical results for the C15 structure.[T6]

theoretical results. The temperatures obtained from the disordered structures are systematically lower and are therefore in better agreement than the perfect system.

A third alternative for disorder is the introduction of vacancies in the system to lower the Fermi level E_f to achieve an electron configuration similar to Pd_2MnSn. By lowering the Fermi level E_f by $0.34\,eV$, a significant qualitative improvement over the perfect structure could be achieved, but the absolute magnon energies are still too high, as can be seen in fig. 5.3.17.

Besides the limited possibilities of stoichiometric disorder, previous experiments[128,129] suggested a multiphase system with significant contributions from Cu_3Mn_2Al crystallizing in a C15 structure. The resulting spectrum in fig. 5.3.18 provides a significant improvement: The long-wavelength dispersion relation is properly described and magnon energies are much more consistent with the experimental data, especially along the high-symmetry line Γ–L. However, the qualitative description of the turning point along the line Γ–X and the minimum at the high-symmetry point K is missing.

The calculated electronic properties of the three presented Heusler alloys are in excellent agreement with previously reported findings. In contrast to this, there are significant problems in the description of their magnetic properties. While the investigations of the Heusler alloy Pd_2MnSn could lead to satisfying results, especially for the dispersion relation, both Ni_2MnSn and Cu_2MnAl lack a proper theoretical description.

This leads to several conclusions: Quantitative predictions for Heusler alloys

remain a problematic topic which might require further qualitative understanding of the underlying magnetism, including the magnetic moment formation and exchange mechanism. A general description of Heusler alloys is unlikely and each compound has to be treated separately. The improvement of theoretically calculated properties with respect to experimental data by introduction of disorder suggests the existence of disorder in most experimental samples. Following from the last point, the probably missing stability and reproducibility of certain compounds with their respective properties could be a serious problem for any application.

6 Summary

In this thesis, the successful application of the multiple scattering approach was demonstrated. This approach was used to calculate diverse physical properties of electronic, magnetic and plasmonic systems.

At first, magnons in disordered systems were calculated in terms of the disordered Heisenberg Hamiltonian. This formulation allows to describe the magnetic properties of many systems with inherent disorder, like the diluted magnets, which appear in nature as alloys of magnetic and non-magnetic materials. The description in terms of large supercells avoids finite-size artifacts, while the averaging procedure keeps the computational requirements moderate. The method was successfully applied to the system $Fe_{1-x}Al_x$ ($x < 0.3$) and can now be used to calculate more complex systems, like the later investigated Heusler alloys.

The second topic was concerned with the investigation of ensembles of plasmonic particles with respect to the scattering of the electromagnetic field of a passing electron. The used approach represents a high-performing extension of the classical Mie theory towards the multi-scattering at multiple particles. Both, the numerical and computational performance were successfully verified by comparing the electron energy loss spectrum of a dimer of two gold spheres with previous results. Due to algorithmic advantages, it was additionally possible to create further spectra, which were not obtainable with a similar method. The good performance allowed to execute structural optimizations to design systems for near-field enhancements at different wavelengths and a plasmonic filter which amplifies the field for one wavelength, while it suppresses the field for another. This method could now be improved to further shapes of scatterers to provide more flexibility in the calculation of plasmonic scattering at ensembles of particles.

The multiple scattering approach was then used to calculate the electronic properties of several semiconductors under mechanical strain. On the one hand, microwires of ZnO were strained to observe the change in its band gap and to calculate the corresponding deformation potential parameter. The influence of several functionals, which determine the calculation of the internal energy and therefore the the equilibrium state at different strains, was investigated to gain a better understanding of the underlying physical phenomena. On the other hand, the semiconducting and topologically insulating alloy $Pb_xSn_{1-x}Te$ was

also examined with respect to its band gap behavior, which shows an inversion under pressure. It was shown that the band gap of this material depends on both the composition and lattice constant of the system. The experimentally determined point of band gap closure was successfully reproduced.

The remaining two sections were concerned with the investigation of Heusler alloys. At first, the Heusler alloy $Ca(Co_xRu_{1-x})O_3$ was studied for small concentrations of Co ($x < 0.2$). Due to the anti-ferromagnetic interaction of the low-concentrated Co atoms, the behavior as a quantum spin liquid was observed. The theoretically determined results support the experimental findings.

The investigation of the Heusler alloys Pd_2MnSn, Ni_2MnSn and Cu_2MnAl was aimed at the description of their magnetic properties, including the magnetic moments, critical temperatures and dispersion relation. This description was satisfactorily achieved for the first of the three Heusler alloys, but was shown to be problematic for the two remaining samples. The improvement of the results by introduction of heavy disorder hints at problems in the stability and reproducibility of experimental results. Especially, the multiphase structure of Cu_2MnAl provides tough conditions for future research. A unified description for the Heusler alloys could not be found and further research of the magnetic properties is required to potentially find suitable applications for these materials.

Summarizing, the multiple scattering approach was successfully used to determine various physical properties of a wide range of materials. While the corresponding methods are already well understood and deeply developed, more complex systems still provide a challenge for most existing approaches and there is still room for improvement.

Appendix

Spherical vector wave functions

The expansion of the electric fields in eqs. (3.2.16) to (3.2.18) in section 3.2.2 is done in terms of the spherical vector wave functions (SVWF). These are constructed from the scalar spherical wave functions, which are solutions to the scalar Helmholtz equation:

$$u_{mn}^{(1,3)}(k\,\boldsymbol{r}) = z_n^{(1,3)}(k\,r)P_n^{|m|}(\cos\theta)\mathrm{e}^{\mathrm{i}m\varphi}, \tag{A.1}$$

with $n = 1, 2, \dots$ and $m = -n, \dots, n$. The position vector $\boldsymbol{r}$ is given by its components in spherical coordinates (r, θ, φ). The spherical Bessel functions $z_n^{(1)} = j_n$ and the spherical Hankel functions of first kind $z_n^{(3)} = h_n^{(1)}$ are used for incoming and outgoing waves, respectively. The remaining two spherical functions, i.e., the spherical Neumann functions $z_n^{(2)} = y_n$ and the spherical Hankel functions of second kind $z_n^{(4)} = h_n^{(2)}$, are not used because the former functions diverge in the origin and the latter signify an incoming spherical wave. Following the definition of Doicu et al.,[28] the polar part is given by the associated Legendre polynomials $P_n^{|m|}$, which depends on the magnitude of m.

The SVWFs are the independent solutions of the vector wave equation, and are given with respect to the pilot vector $\boldsymbol{r}$ as

$$\boldsymbol{M}_{mn}^{(1,3)}(k\,\boldsymbol{r}) = \frac{1}{\sqrt{2n(n+1)}}\boldsymbol{\nabla}u_{mn}^{1,3}(k\,\boldsymbol{r}) \times \boldsymbol{r}, \tag{A.2}$$

$$\boldsymbol{N}_{mn}^{(1,3)}(k\,\boldsymbol{r}) = \frac{1}{k}\boldsymbol{\nabla} \times \boldsymbol{M}_{mn}^{(1,3)}(k\,\boldsymbol{r}). \tag{A.3}$$

By defining the angular function τ_n^m and π_n^m in terms of the associated Legendre polynomials P_n^m,

$$\tau_n^m(\theta) = \frac{\mathrm{d}}{\mathrm{d}\theta}P_n^m(\cos\theta), \qquad\qquad \pi_n^m(\theta) = \frac{P_n^m(\cos\theta)}{\sin\theta}, \tag{A.4}$$

the final expressions for the SVWFs are given by

$$\boldsymbol{M}_{mn}^{(1,3)}(k\,\boldsymbol{r}) = \frac{z_n^{(1,3)}(k\,r)}{\sqrt{2n(n+1)}}\Big(\mathrm{i}m\pi_n^{|m|}(\theta)\boldsymbol{e}_\theta - \tau_n^{|m|}(\theta)\boldsymbol{e}_\varphi\Big)\mathrm{e}^{\mathrm{i}m\varphi}, \qquad (A.5)$$

$$\boldsymbol{N}_{mn}^{(1,3)}(k\,\boldsymbol{r}) = \frac{1}{\sqrt{2n(n+1)}}\bigg(n(n+1)\frac{z_n^{(1,3)}(k\,r)}{k\,r}P_n^{|m|}(\cos\theta)\boldsymbol{e}_\mathrm{r}$$

$$+ \frac{\big[k\,r\,z_n^{(1,3)}(k\,r)\big]'}{k\,r}\Big(\tau_n^{|m|}(\theta)\boldsymbol{e}_\theta + \mathrm{i}m\pi_n^{|m|}(\theta)\boldsymbol{e}_\varphi\Big)\bigg)\mathrm{e}^{\mathrm{i}m\varphi}. \qquad (A.6)$$

Bibliography

Publications

[T1]   P. Buczek, L. M. Sandratskii, N. Buczek, S. Thomas, G. Vignale, and A. Ernst, "Magnons in disordered nonstoichiometric low-dimensional magnets", Physical Review B **94**, 054407 (2016).

[T2]   S. Thomas, C. Matyssek, W. Hergert, M. Arnold, L. Kiewidt, M. Karamehmedović, and T. Wriedt, "Application of Generalized Mie Theory to EELS Calculations as a Tool for Optimization of Plasmonic Structures", Plasmonics **11**, 865 (2016).

[T3]   W. A. Adeagbo, S. Thomas, S. K. Nayak, A. Ernst, and W. Hergert, "First-principles study of uniaxial strained and bent ZnO wires", Physical Review B **89**, 195135 (2014).

[T4]   M. Geilhufe, S. K. Nayak, S. Thomas, M. Däne, G. S. Tripathi, P. Entel, W. Hergert, and A. Ernst, "Effect of hydrostatic pressure and uniaxial strain on the electronic structure of $Pb_{1-x}Sn_xTe$", Physical Review B **92**, 235203 (2015).

[T5]   J. Gunasekera, A. Dahal, J. A. Rodriguez-Rivera, L. Harriger, S. Thomas, A. Ernst, T. Heitmann, and D. K. Singh, "Quantum magnetic properties in perovskite with artificial spin-½", Submitted to Nature Physics, May 2016.

[T6]   G. Fischer, X. Zubizarreta, A. Marmodoro, M. Däne, S. Thomas, P. Entel, W. Hergert, E. K. U. Gross, and A. Ernst, "First principles description of the magnetic properties of Pd_2MnSn, Ni_2MnSn, and Cu_2MnAl Heusler Alloys", in preparation, 2016.

References

[1] K. Zakeri and J. Kirschner, "Magnonics: From Fundamentals to Applications", in *Topics in Applied Physics*, Vol. 125, edited by O. S. Demokritov and N. A. Slavin (Springer Berlin Heidelberg, Berlin, Heidelberg, 2013) Chap. Probing Magnons by Spin-Polarized Electrons, pages 83–99.

[2] V. V. Kruglyak, S. O. Demokritov, and D. Grundler, "Magnonics", Journal of Physics D: Applied Physics **43**, 264001 (2010).

[3] S. Neusser and D. Grundler, "Magnonics: Spin Waves on the Nanoscale", Advanced Materials **21**, 2927 (2009).

[4] K. Sato, L. Bergqvist, J. Kudrnovský, P. H. Dederichs, O. Eriksson, I. Turek, B. Sanyal, G. Bouzerar, H. Katayama-Yoshida, V. A. Dinh, T. Fukushima, H. Kizaki, and R. Zeller, "First-principles theory of dilute magnetic semiconductors", Reviews of Modern Physics **82**, 1633 (2010).

[5] H. Ibach, D. Bruchmann, R. Vollmer, M. Etzkorn, P. S. Anil Kumar, and J. Kirschner, "A novel spectrometer for spin-polarized electron energy-loss spectroscopy", Review of Scientific Instruments **74**, 4089 (2003).

[6] B. N. Brockhouse, "Scattering of Neutrons by Spin Waves in Magnetite", Physical Review **106**, 859 (1957).

[7] R. N. Sinclair and B. N. Brockhouse, "Dispersion Relation for Spin Waves in a fcc Cobalt Alloy", Physical Review **120**, 1638 (1960).

[8] A. Furrer, J. Mesot, and T. Strässle, *Neutron Scattering in Condensed Matter Physics* (World Scientific, Singapore, 2009).

[9] E. Samuelson, T. Riste, and O. Steinsvoll, "Spin wave scattering of polarised neutrons", Physics Letters **6**, 47 (1963).

[10] H. Pan, V. L. Zhang, K. Di, M. H. Kuok, H. S. Lim, S. C. Ng, N. Singh, and A. O. Adeyeye, "Phononic and magnonic dispersions of surface waves on a permalloy/BARC nanostructured array", Nanoscale Research Letters **8**, 115 (2013).

[11] M. Pomerantz, "Excitation of Spin-Wave Resonance by Microwave Phonons", Physical Review Letters **7**, 312 (1961).

[12] M. H. Seavey and P. E. Tannenwald, "Direct Observation of Spin-Wave Resonance", Physical Review Letters **1**, 168 (1958).

[13] T. Balashov, "Inelastic scanning tunneling spectroscopy: magnetic excitations on the nanoscale", PhD thesis (Universität Karlsruhe (TH), Jan. 2009).

[14] T. Coenen, E. J. R. Vesseur, A. Polman, and A. F. Koenderink, "Directional emission from plasmonic Yagi-Uda antennas probed by angle-resolved cathodoluminescence spectroscopy.", Nano Letters **11**, 3779 (2011).

[15] F. von Cube, S. Irsen, J. Niegemann, C. Matyssek, W. Hergert, K. Busch, and S. Linden, "Spatio-spectral characterization of photonic meta-atoms with electron energy-loss spectroscopy [Invited]", EN, Optical Materials Express **1**, 1009 (2011).

[16] T. Coenen, E. J. R. Vesseur, and A. Polman, "Deep subwavelength spatial characterization of angular emission from single-crystal Au plasmonic ridge nanoantennas.", ACS Nano **6**, 1742 (2012).

[17] E. J. R. Vesseur, J. Aizpurua, T. Coenen, A. Reyes-Coronado, P. E. Batson, and A. Polman, "Plasmonic excitation and manipulation with an electron beam", MRS Bulletin **37**, 752 (2012).

[18] A. Y. Elezzabi, "The dawn of spinplasmonics", Nano Today **2**, 48 (2007).

[19] C. J. E. Straatsma, M. Johnson, and A. Y. Elezzabi, "Terahertz spinplasmonics in random ensembles of ni and co microparticles", Journal of Applied Physics **112**, 103904 (2012).

[20] S. T. Chui and Z.-F. Lin, "Spin plasmonics in magnetism", Chinese Physics B **23**, 117802 (2014).

[21] J. Homola, "Surface Plasmon Resonance Based Sensors", in *Springer Series on Chemical Sensors and Biosensors*, Vol. 4, edited by J. Homola (Springer Berlin Heidelberg, Berlin, Heidelberg, 2006) Chap. Electromagnetic Theory of Surface Plasmons, pages 3–44.

[22] P. A. Buczek, "Spin dynamics of complex itinerant magnets", PhD thesis (Martin-Luther-Universität Halle-Wittenberg, 2009).

[23] B. T. Draine and P. J. Flatau, "Discrete-dipole approximation for scattering calculations", Journal of the Optical Society of America A **11**, 1491 (1994).

[24] C. Hafner, *The Generalized Multipole Technique for Computational Electromagnetics* (Artech House Books, Boston, 1990).

[25] F. J. García de Abajo and A. Howie, "Retarded field calculation of electron energy loss in inhomogeneous dielectrics", Physical Review B **65**, 115418 (2002).

[26] K. Busch, M. König, and J. Niegemann, "Discontinuous Galerkin methods in nanophotonics", Laser & Photonics Reviews **5**, 773 (2011).

[27] C. Matyssek, J. Niegemann, W. Hergert, and K. Busch, "Computing electron energy loss spectra with the Discontinuous Galerkin Time-Domain method", Photonics and Nanostructures - Fundamentals and Applications **9**, 367 (2011).

[28] A. Doicu, T. Wriedt, and Y. A. Eremin, *Light Scattering by Systems of Particles*, Vol. 124, Springer Series in OPTICAL SCIENCES (Springer Berlin Heidelberg, Berlin, Heidelberg, 2006).

[29] Y.-l. Xu, "Electromagnetic scattering by an aggregate of spheres", Applied Optics **34**, 4573 (1995).

[30] Y.-l. Xu, "Electromagnetic Scattering by an Aggregate of Spheres: Errata", Applied Optics **37**, 6494 (1998).

[31]   K. Zakeri, T.-H. Chuang, A. Ernst, L. M. Sandratskii, P. Buczek, H. J. Qin, Y. Zhang, and J. Kirschner, "Direct probing of the exchange interaction at buried interfaces", Nature Nanotechnology **8**, 853 (2013).

[32]   R. Nathans, C. Shull, G. Shirane, and A. Andresen, "The use of polarized neutrons in determining the magnetic scattering by iron and nickel", Journal of Physics and Chemistry of Solids **10**, 138 (1959).

[33]   S. A. Maier, *Plasmonics: Fundamentals and Applications* (Springer Science US, 2007).

[34]   S. Thomas, "Berechnung von Eigenmoden plasmonischer Systeme", Bachelor's thesis (Martin-Luther-Universität Halle-Wittenberg, Halle, 2010).

[35]   S. Thomas, "Symmetrieeigenschaften und Optimierung photonischer und plasmonischer Nanostrukturen", Master's thesis (Martin-Luther-Universität Halle-Wittenberg, Halle, 2013).

[36]   P. B. Johnson and R. W. Christy, "Optical Constants of the Noble Metals", Physical Review B **6**, 4370 (1972).

[37]   M. A. Green, "Self-consistent optical parameters of intrinsic silicon at 300 K including temperature coefficients", Solar Energy Materials and Solar Cells **92**, 1305 (2008).

[38]   F. J. García de Abajo and M. Kociak, "Electron energy-gain spectroscopy", New Journal of Physics **10**, 073035 (2008).

[39]   P. Hohenberg and W. Kohn, "Inhomogeneous Electron Gas", Physical Review **136**, B864 (1964).

[40]   J. Korringa, "On the calculation of the energy of a Bloch wave in a metal", Physica **13**, 392 (1947).

[41]   W. Kohn and N. Rostoker, "Solution of the Schrödinger Equation in Periodic Lattices with an Application to Metallic Lithium", Physical Review **94**, 1111 (1954).

[42]   A. Liechtenstein, M. Katsnelson, V. Antropov, and V. Gubanov, "Local spin density functional approach to the theory of exchange interactions in ferromagnetic metals and alloys", Journal of Magnetism and Magnetic Materials **67**, 65 (1987).

[43]   A. Ernst, "Multiple-scattering theory: new developments and applications", Habilitation thesis (Martin-Luther-Universität Halle-Wittenberg, Halle, 2007).

[44]   R. M. Geilhufe, "Complex structures, disorder and low dimensionality – Treatment of oxides and semiconductors by a relativistic Korringa-Kohn-Rostoker Green function method", PhD thesis (Martin-Luther-Universität Halle-Wittenberg, 2015).

[45]   W. Kohn and L. J. Sham, "Self-Consistent Equations Including Exchange and Correlation Effects", Physical Review **140**, A1133 (1965).

[46] J. Zabloudil, R. Hammerling, P. Weinberger, and L. Szunyogh, editors, *Electron Scattering in Solid Matter*, Vol. 147, Springer Series in Solid-State Sciences (Springer Berlin Heidelberg, 2005).

[47] J. S. Faulkner, "Multiple-scattering approach to band theory", Physical Review B **19**, 6186 (1979).

[48] M. Hoffmann, "Multiple scattering theory for the description of defects in metallic alloys and oxide systems", PhD thesis (Martin-Luther-Universität Halle-Wittenberg, 2016).

[49] A. Marmodoro, A. Ernst, S. Ostanin, and J. B. Staunton, "Generalized inclusion of short-range ordering effects in the coherent potential approximation for complex-unit-cell materials", Physical Review B **87**, 125115 (2013).

[50] G. Fischer, M. Däne, A. Ernst, P. Bruno, M. Lüders, Z. Szotek, W. Temmerman, and W. Hergert, "Exchange coupling in transition metal monoxides: Electronic structure calculations", Physical Review B **80**, 014408 (2009).

[51] G. Fischer, "Defektinduzierter und intrinsischer Magnetismus in Zinkoxid und Übergangsmetallfluoriden - Einfluss von Korrelationskorrekturen", PhD thesis (Martin-Luther-Universität Halle-Wittenberg, 2011).

[52] D. W. Mackowski, "Analysis of Radiative Scattering for Multiple Sphere Configurations", Proceedings of the Royal Society A: Mathematical, Physical and Engineering Sciences **433**, 599 (1991).

[53] C. F. Matyssek, "Investigation of Plasmonic Structures by Light and Electron Microscopy: Contributions to an Efficient Numerical Treatment", PhD thesis (Martin-Luther-Universität Halle-Wittenberg, 2012).

[54] F. J. García de Abajo, "Relativistic energy loss and induced photon emission in the interaction of a dielectric sphere with an external electron beam", Physical Review B **59**, 3095 (1999).

[55] R. Durstenfeld, "Algorithm 235: Random Permutation", Communications of the ACM **7**, 420 (1964).

[56] K. Perlin, "An Image Synthesizer", SIGGRAPH Computer Graphics **19**, 287 (1985).

[57] K. Perlin, "Improving Noise", ACM Transactions on Graphics **21**, 681 (2002).

[58] K. Perlin, "Standard for perlin noise", 6,867,776 (2005), US Patent.

[59] W. H. Press, S. A. Teukolsky, W. T. Vetterling, and B. P. Flannery, *Numerical Recipes in Fortran 77: The Art of Scientific Computing*, 2nd edition (Cambridge University Press, 1997).

[60] K. C. Hass, B. Velický, and H. Ehrenreich, "Simplification of Green's-function calculations through analytic continuation", Physical Review B **29**, 3697 (1984).

[61] L. J. Gray and T. Kaplan, "Analytic continuation and Green function calculations", Journal of Physics A: Mathematical and General **19**, 1555 (1986).

[62] G. Engeln-Müllges, K. Niederdrenk, and R. Wodicka, *Numerik-Algorithmen*, 10th edition, Xpert.press (Springer Berlin Heidelberg, 2011).

[63] V. D. Natoli, M. H. Cohen, and B. Fornberg, "A New Numerical Algorithm for the Analytic Continuation of Green's Functions", Journal of Computational Physics **126**, 99 (1996).

[64] A. S. Mishchenko, "Correlated Electrons: From Models to Materials", in *Modeling and Simulation*, Vol. 2, edited by E. Pavarini, E. Koch, F. Anders, and M. Jarrell (Forschungszentrum Jülich GmbH, 2012) Chap. Stochastic Optimization Method for Analytic Continuation, pages 395–422.

[65] J. A. Nelder and R. Mead, "A Simplex Method for Function Minimization", The Computer Journal **7**, 308 (1965).

[66] C. Forestiere, A. J. Pasquale, A. Capretti, G. Miano, A. Tamburrino, S. Y. Lee, B. M. Reinhard, and L. Dal Negro, "Genetically engineered plasmonic nanoarrays.", Nano Letters **12**, 2037 (2012).

[67] K. Höflich, M. Becker, G. Leuchs, and S. Christiansen, "Plasmonic dimer antennas for surface enhanced Raman scattering", Nanotechnology **23**, 185303 (2012).

[68] W. Chu, X. Gao, and S. Sorooshian, "A new evolutionary search strategy for global optimization of high-dimensional problems", Information Sciences **181**, 4909 (2011).

[69] S.-H. Kim, H. Kim, and N. J. Kim, "Brittle intermetallic compound makes ultrastrong low-density steel with large ductility", Nature **518**, 77 (2015).

[70] L. M. Sandratskii and P. Bruno, "Exchange interactions and Curie temperature in (Ga,Mn)As", Physical Review B **66**, 134435 (2002).

[71] G. Bouzerar, J. Kudrnovský, L. Bergqvist, and P. Bruno, "Ferromagnetism in diluted magnetic semiconductors: A comparison between *ab initio* mean-field, RPA, and Monte Carlo treatments", Physical Review B **68**, 081203 (2003).

[72] L. Bergqvist, O. Eriksson, J. Kudrnovský, V. Drchal, A. Bergman, L. Nordström, and I. Turek, "Magnetic properties and disorder effects in diluted magnetic semiconductors", Physical Review B **72**, 195210 (2005).

[73] A. Chakraborty, R. Bouzerar, S. Kettemann, and G. Bouzerar, "Nanoscale inhomogeneities: a new path toward high curie temperature ferromagnetism in diluted materials", Physical Review B **85**, 014201 (2012).

[74] N. D. Mermin and H. Wagner, "Absence of Ferromagnetism or Antiferromagnetism in One- or Two-Dimensional Isotropic Heisenberg Models", Physical Review Letters **17**, 1133 (1966).

[75] N. D. Mermin and H. Wagner, "Absence of Ferromagnetism or Antiferromagnetism in One- or Two-Dimensional Isotropic Heisenberg Models", Physical Review Letters **17**, 1307 (1966).

[76] M. E. J. Newman and R. M. Ziff, "Efficient Monte Carlo Algorithm and High-Precision Results for Percolation", Physical Review Letters **85**, 4104 (2000).

[77] Ł. Kurzawski and K. Malarz, "Simple Cubic Random-Site Percolation Thresholds for Complex Neighbourhoods", Reports on Mathematical Physics **70**, 163 (2012).

[78] X. Xu, J. Wang, J.-P. Lv, and Y. Deng, "Simultaneous analysis of three-dimensional percolation models", Frontiers of Physics **9**, 113 (2014).

[79] P. Shukla and M. Wortis, "Spin-glass behavior in iron-aluminum alloys: A microscopic model", Physical Review B **21**, 159 (1980).

[80] Z. Jagličić, S. Vrtnik, M. Feuerbacher, and J. Dolinšek, "Magnetic properties of FeAl$_2$ and Fe$_2$Al$_5$", Physical Review B **83**, 224427 (2011).

[81] H. Kleykamp and H. Glasbrenner, "Thermodynamic properties of solid aluminum-iron alloys", Zeitschrift für Metallkunde **88**, 230 (1997).

[82] P. Bruno, J. Kudrnovský, V. Drchal, and I. Turek, "Interlayer Exchange Coupling: The Effect of Substitutional Disorder", Physical Review Letters **76**, 4254 (1996).

[83] J. Kudrnovský, V. Drchal, I. Turek, and P. Bruno, "Exchange interactions in random magnetic overlayers", Surface Science **507–510**, 567 (2002).

[84] C. Matyssek, V. Schmidt, W. Hergert, and T. Wriedt, "The T-Matrix method in electron energy loss and cathodoluminescence spectroscopy calculations for metallic nano-particles.", Ultramicroscopy **117**, 46 (2012).

[85] E. J. Zeman and G. C. Schatz, "An accurate electromagnetic theory study of surface enhancement factors for silver, gold, copper, lithium, sodium, aluminum, gallium, indium, zinc, and cadmium", The Journal of Physical Chemistry **91**, 634 (1987).

[86] S. Berciaud, L. Cognet, P. Tamarat, and B. Lounis, "Observation of Intrinsic Size Effects in the Optical Response of Individual Gold Nanoparticles", Nano Letters **5**, 515 (2005).

[87] N. Grady, N. Halas, and P. Nordlander, "Influence of dielectric function properties on the optical response of plasmon resonant metallic nanoparticles", Chemical Physics Letters **399**, 167 (2004).

[88] A. Vial, A.-S. Grimault, D. Macías, D. Barchiesi, and M. L. de la Chapelle, "Improved analytical fit of gold dispersion: Application to the modeling of extinction spectra with a finite-difference time-domain method", Physical Review B **71**, 085416 (2005).

[89] P. G. Etchegoin, E. C. Le Ru, and M. Meyer, "An analytic model for the optical properties of gold", The Journal of Chemical Physics **125**, 164705 (2006).

[90] P. G. Etchegoin, E. C. Le Ru, and M. Meyer, "Erratum: An analytic model for the optical properties of gold", The Journal of Chemical Physics **127**, 189901 (2007).

[91] C. David and F. J. García de Abajo, "Spatial Nonlocality in the Optical Response of Metal Nanoparticles", The Journal of Physical Chemistry C **115**, 19470 (2011).

[92] F. J. García de Abajo, "Nonlocal Effects in the Plasmons of Strongly Interacting Nanoparticles, Dimers, and Waveguides", The Journal of Physical Chemistry C **112**, 17983 (2008).

[93] H. Duan, A. I. Fernández-Domínguez, M. Bosman, S. A. Maier, and J. K. W. Yang, "Nanoplasmonics: Classical down to the Nanometer Scale", Nano Letters **12**, 1683 (2012).

[94] Y.-l. Xu and N. G. Khlebtsov, "Orientation-averaged radiative properties of an arbitrary configuration of scatterers", Journal of Quantitative Spectroscopy and Radiative Transfer **79**–**80**, 1121 (2003).

[95] B. Yan, S. V. Boriskina, and B. M. Reinhard, "Optimizing Gold Nanoparticle Cluster Configurations ($n \leq 7$) for Array Applications.", The Journal of Physical Chemistry C **115**, 4578 (2011).

[96] P. Zheng, S. K. Cushing, S. Suri, and N. Wu, "Tailoring plasmonic properties of gold nanohole arrays for surface-enhanced Raman scattering.", Physical Chemistry Chemical Physics **17**, 21211 (2015).

[97] COMSOL Multiphysics, *Comsol*, computer software, version 4.3, 2012.

[98] L. Fast, J. M. Wills, B. Johansson, and O. Eriksson, "Elastic constants of hexagonal transition metals: Theory", Physical Review B **51**, 17431 (1995).

[99] R. Ahuja, L. Fast, O. Eriksson, J. M. Wills, and B. Johansson, "Elastic and high pressure properties of ZnO", Journal of Applied Physics **83**, 8065 (1998).

[100] T. B. Bateman, "Elastic Moduli of Single-Crystal Zinc Oxide", Journal of Applied Physics **33**, 3309 (1962).

[101] I. Kobiakov, "Elastic, piezoelectric and dielectric properties of ZnO and CdS single crystals in a wide range of temperatures", Solid State Communications **35**, 305 (1980).

[102] C. P. Dietrich, M. Lange, F. J. Klüpfel, H. von Wenckstern, R. Schmidt-Grund, and M. Grundmann, "Strain distribution in bent ZnO microwires", Applied Physics Letters **98**, 031105 (2011).

[103] A. R. H. Preston, B. J. Ruck, L. F. J. Piper, A. DeMasi, K. E. Smith, A. Schleife, F. Fuchs, F. Bechstedt, J. Chai, and S. M. Durbin, "Band structure of ZnO from resonant x-ray emission spectroscopy", Physical Review B **78**, 155114 (2008).

[104] R. A. Powell, W. E. Spicer, and J. C. McMenamin, "Location of the Zn$3d$ States in ZnO", Physical Review Letters **27**, 97 (1971).

[105] C. J. Vesely, R. L. Hengehold, and D. W. Langer, "uv Photoemission Measurements of the Upper d Levels in the IIB-VIA Compounds", Physical Review B **5**, 2296 (1972).

[106] K. Hümmer, "Interband Magnetoreflection of ZnO", Physica Status Solidi B **56**, 249 (1973).

[107] Ü. Özgür, Y. I. Alivov, C. Liu, A. Teke, M. A. Reshchikov, S. Doğan, V. Avrutin, S.-J. Cho, and H. Morkoç, "A comprehensive review of ZnO materials and devices", Journal of Applied Physics **98**, 041301 (2005).

[108] E. Engel and R. M. Dreizler, *Density Functional Theory*, Theoretical and Mathematical Physics (Springer Berlin Heidelberg, 2011).

[109] J. O. Dimmock, I. Melngailis, and A. J. Strauss, "Band Structure and Laser Action in $Pb_xSn_{1-x}Te$", Physical Review Letters **16**, 1193 (1966).

[110] A. Ishida, T. Tsuchiya, T. Yamada, D. Cao, S. Takaoka, M. Rahim, F. Felder, and H. Zogg, "Electrical and optical properties of SnEuTe and SnSrTe films", Journal of Applied Physics **107**, 123708 (2010).

[111] J. R. Dixon and R. F. Bis, "Band Inversion and the Electrical Properties of $Pb_xSn_{1-x}Te$", Physical Review **176**, 942 (1968).

[112] P. Barone, T. Rauch, D. Di Sante, J. Henk, I. Mertig, and S. Picozzi, "Pressure-induced topological phase transitions in rocksalt chalcogenides", Physical Review B **88**, 045207 (2013).

[113] S. A. Wolf, D. D. Awschalom, R. A. Buhrman, J. M. Daughton, S. von Molnár, M. L. Roukes, A. Y. Chtchelkanova, and D. M. Treger, "Spintronics: A Spin-Based Electronics Vision for the Future", Science **294**, 1488 (2001).

[114] T. Sebastian, Y. Ohdaira, T. Kubota, P. Pirro, T. Brächer, K. Vogt, A. A. Serga, H. Naganuma, M. Oogane, Y. Ando, and B. Hillebrands, "Low-damping spin-wave propagation in a micro-structured $Co_2Mn_{0.6}Fe_{0.4}Si$ Heusler waveguide", Applied Physics Letters **100**, 112402 (2012).

[115] J. M. D. Coey, "Hard Magnetic Materials: A Perspective", IEEE Transactions on Magnetics **47**, 4671 (2011).

[116] S. Plogmann, T. Schlathölter, J. Braun, M. Neumann, Y. M. Yarmoshenko, M. V. Yablonskikh, E. I. Shreder, E. Z. Kurmaev, A. Wrona, and A. Ślebarski, "Local moments in Mn-based Heusler alloys and their electronic structures", Physical Review B **60**, 6428 (1999).

[117] D. Brown, M. D. Crapper, K. H. Bedwell, M. T. Butterfield, S. J. Guilfoyle, A. E. R. Malins, and M. Petty, "Photoelectron spectroscopy of manganese-based Heusler alloys", Physical Review B **57**, 1563 (1998).

[118] P. J. Webster, "Heusler alloys", Contemporary Physics **10**, 559 (1969).

[119] E. Uhl, "Magnetism of two new series of Heusler alloys: $(Rh_{1-x}Co_x)_2MnSn$ and $(Rh_{1-x}Ni_x)_2MnSn$", Journal of Magnetism and Magnetic Materials **49**, 101 (1985).

[120] K. Endō, T. Ohoyama, and R. Kimura, "On the Magnetic Moment of Mn in Aluminum Heusler Alloy", Journal of the Physical Society of Japan **19**, 1494 (1964).

[121] Y. Noda and Y. Ishikawa, "Spin Waves in Heusler Alloys Pd_2MnSn and Ni_2MnSn", Journal of the Physical Society of Japan **40**, 690 (1976).

[122] T. Kanomata, K. Endo, Y. Chieda, T. Sugawara, K. Obara, T. Shishido, K. Matsubayashi, Y. Uwatoko, H. Nishihara, R. Umetsu, M. Nagasako, and R. Kainuma, "Magnetic properties of Mn-rich Pd_2MnSn Heusler alloys", Journal of Alloys and Compounds **505**, 29 (2010).

[123] M. G. Natera, M. R. L. N. Murthy, R. J. Begum, and N. S. Satya Murthy, "Atomic and magnetic structure of the heusler alloys Pd_2MnGe, Pd_2MnSn, Cu_2MnIn, and CoMnSb", Physica Status Solidi A **3**, 959 (1970).

[124] S. Podgornykh, S. Streltsov, V. Kazantsev, and E. Shreder, "Heat capacity of Heusler alloys: Ferromagnetic Ni_2MnSb, Ni_2MnSn, NiMnSb and antiferromagnetic CuMnSb", Journal of Magnetism and Magnetic Materials **311**, 530 (2007).

[125] K. Tajima, Y. Ishikawa, P. J. Webster, M. W. Stringfellow, D. Tocchetti, and K. R. A. Zeabeck, "Spin Waves in a Heusler Alloy Cu_2MnAl", Journal of the Physical Society of Japan **43**, 483 (1977).

[126] E. Şaşıoğlu, L. M. Sandratskii, and P. Bruno, "First-principles calculation of the intersublattice exchange interactions and Curie temperatures of the full Heusler alloys Ni_2MnX (X=Ga, In, Sn, Sb)", Physical Review B **70**, 024427 (2004).

[127] E. Şaşıoğlu, L. M. Sandratskii, and P. Bruno, "Role of conduction electrons in mediating exchange interactions in Mn-based Heusler alloys", Physical Review B **77**, 064417 (2008).

[128] G. Johnston and E. Hall, "Studies on the Heusler alloys – II. The structure of Cu_3Mn_2Al", Journal of Physics and Chemistry of Solids **29**, 201 (1968).

[129] Y. V. Kudryavtsev, V. A. Oksenenko, N. N. Lee, Y. P. Lee, J. Y. Rhee, and J. Dubowik, "Effect of structural disorder on some physical properties of the Cu_2MnAl Heusler alloy films", Journal of Applied Physics **97**, 113903 (2005).

Acknowledgments

At this point I'd like to thank all those, who supported me on my way towards this thesis.

At first, I want to thank my supervisors Arthur Ernst and Wolfram Hergert for the opportunity to write this thesis and the ongoing support to finish this work. It was a pleasure to work under their guidance.

I thank all contributors of the publications, which led to this dissertation. It would not have been possible without their hard work.

Then, I'd like to thank my colleagues Waheed Adeagbo, Matthias Geilhufe, Martin Hoffmann and Sanjeev Nayak for the nice working atmosphere in our office. They were always open for serious and not-so-serious discussions.

A big thanks goes to Steven Achilles for the inspiring daily coffee breaks in the morning. I'd like to thank him and Michael Hengst for many exciting hours of working together on the computing cluster of our institute.

For the repeated proof-reading of this thesis, I have to thank Arthur Ernst, Wolfram Hergert, Martin Hoffmann and Paweł Buczek. Additionally, I'd like to thank the referees for reading my thesis.

Finally, I'd like to thank my family and my fiancée, Melanie Zorn, for the steady support during my studies.

<center>Thank you!</center>

Eidesstattliche Erklärung

Hiermit erkläre ich gemäß §5 der Promotionsordnung der Naturwissenschaftlichen Fakultäten I, II, III und des Zentrums für Ingenieurwissenschaften der Martin-Luther-Universität Halle-Wittenberg vom 13. Juni 2012, in der Fassung vom 26. Februar 2013, dass ich die vorliegende Dissertation selbständig und ohne fremde Hilfe verfasst habe, keine anderen als die von mir angegebenen Quellen und Hilfsmittel benutzt habe und die den benutzten Werken wörtlich oder inhaltlich entnommenen Stellen als solche kenntlich gemacht habe.

Weiter erkläre ich, dass ich bisher keine vergeblichen Promotionsversuche unternommen habe und dass diese Dissertation weder in der gegenwärtigen, noch in einer anderen Fassung, einer anderen Fakultät vorgelegen hat.

Halle (Saale), 05. 10. 2016

‾‾‾‾‾‾‾‾‾‾‾‾‾‾‾‾‾‾‾‾‾‾‾‾‾‾‾‾‾‾
Stefan Thomas

Curriculum Vitae

Persönliche Details

Name	Stefan Thomas
Geburtstag	12. Februar 1988
Geburtsort	Merseburg
Staatsangehörigkeit	Deutschland

Ausbildung

Studium

seit 2013	Doktorand, *Max-Planck-Institut für Mikrostrukturphysik*, Halle
2010 – 2013	Master of Science, *Martin-Luther-Universität*, Halle Masterarbeit: „Symmetrieeigenschaften und Optimierung photonischer und plasmonischer Nanostrukturen"
2007 – 2010	Bachelor of Science, *Martin-Luther-Universität*, Halle Bachelorarbeit: „Berechnung von Eigenmoden plasmonischer Systeme"

Schulbildung

2000 – 2007	Domgymnasium Merseburg, *Abitur*
1998 – 2000	Sekundarschule Merseburg-West
1994 – 1998	Grundschule Merseburg-West

Halle (Saale), 05. 10. 2016

_____

Stefan Thomas